UNIVERSITY OF OKLAHOMA

GRADUATE COLLEGE

USING MOLECULAR DYNAMICS SIMULATION TO STUDY BEHAVIOR OF HYDROCARBON FLUID

A THESIS

SUBMITTED TO THE GRADUATE FACULTY

In partial fulfillment of the requirements for the

Degree of

MASTER OF SCIENCE

By

QIUHAO CHANG

Norman, Oklahoma

2019

USING MOLECULAR DYNAMICS SIMULATION TO STUDY BEHAVIOR OF HYDROCARBON FLUID

A THESIS APPROVED FOR THE
MEWBOURNE SCHOOL OF PETROLEUM AND GEOLOGICAL ENGINEERING

BY

Dr. Xingru Wu, Chair

Dr. Liangliang Huang

Dr. Mashhad Fahes

Acknowledgments

First of all, I would like to express my sincere gratitude to my advisors, Dr. Xingru Wu, and Dr. Liangliang Huang, for their instructive advice and valuable guidance on my research studies. Without their consistent and illuminating instruction, I couldn't finish my research studies and my master's degree program.

Also, I would like to appreciate my committee member, Dr. Mashhad Fahes, for her suggestions and insightful comments on this research.

I want to thank my colleagues and friends, Qi Qiao, Guobing Zhou, and Yixin Ma, for all the help and support to the study and the learning of molecular dynamics simulation methods.

Last but not least, I express my deepest gratitude to my beloved parents who have always been encouraging me and supporting me without any complaint.

Table of Contents

List of Tables

List of Figures

Abstract

The purpose of this thesis is to study hydrocarbon fluid behavior with molecular dynamics (MD) simulations. In the past two decades, MD simulation has been proved to be a reliable tool in the study of oil and natural gas properties, and it plays an essential role to seek fundamental understandings from the molecular level.

For shale gas reservoirs, the storage of adsorbed gas is a large portion of original gas in place (OGIP). At first, the combination of MD simulation and cylindrical simplified local density (SLD) model was used to study the adsorption of hydrocarbon fluid in cylindrical nanopores through the analysis of local density distribution profiles. The second MD study in this thesis is about the phase behavior of petroleum fluids. To both convention and unconventional reservoirs, the ability to predict the state (gas or liquid) of a component is critical in many petroleum processes. In this thesis, with the trajectory from MD simulations, three different post-analysis methods have been evaluated to identify the phase of hydrocarbon fluid under a specified condition. Lastly, MD simulations have been performed to investigate the behavior of CO_2 from water/oil/CO_2 mixtures. Those systems are important to the tertiary recovery of conventional oil reservoirs. The industry has been developing technologies such as immiscible CO_2 flooding and in-situ CO_2 generation method. However, a systematic and molecular-level understanding of the phase behavior of the water/oil/CO_2 systems is still incomplete.

The completed studies in this thesis include: (1). The adsorption behavior of

hydrocarbon fluid in cylindrical nanopore was studied by using both the MD simulation and SLD model. In addition, the competitive adsorption between methane and n-butane molecule in nanopores was investigated by both methods. Lastly, a new method which combines SLD model and pore size distribution has been developed to estimate the OGIP of shale gas reservoirs. (2). Three post-analysis methods that utilize MD simulation trajectories have been evaluated to identify the phase state of methane and n-butane under a certain temperature and pressure condition. Although future efforts are needed to improve the accuracy, the completed work and the general ideas proposed in this study are important references to future studies in this field. (3). In the water/oil/CO_2 mixtures, the effect of pressure and temperature on CO_2 self-diffusion was studied via MD simulations. Additionally, a constructive idea by using MD simulations to determine CO_2 partition coefficient of water/oil/CO_2 systems was proposed.

Chapter 1: Introduction

1.1 Background of Shale Gas

According to the natural gas production report (**Figure 1**) from the U.S. Energy Information Administration (EIA, 2016), the shale gas production will be steadily growing in the next few decades. Due to the increase in demand and supply of shale gas, the comprehensive understanding of shale gas is essential for its development.

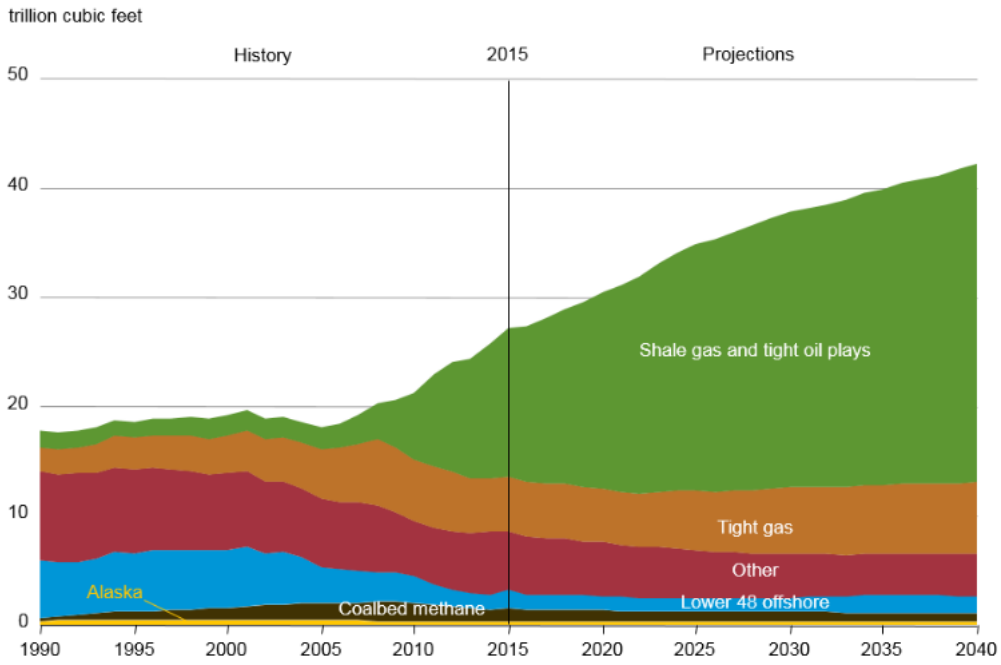

Figure 1: U.S. natural gas production from 1990 to 2040
[Source: Energy Information Administration, 2016].

Shale gas is known as unconventional resources and is the natural gas trapped in the shale formation, which has little difference with conventional natural gas resources in componentwise. Shale is a kind of fine-grained sedimentary rock formed from compaction process of small mineral particles such as mud, quartz, calcite, etc. Fissile

and laminated are two unique characteristics of the shale formation. The fissile feature refers to shale rocks that can easily split into thin pieces, while laminated feature refers to shale rocks made up of multiple thin layers.

Since the shale formation mechanism is different from conventional sedimentary rocks, the permeability and pore-throat size of shale rocks significantly differ from conventional sedimentary rocks. The permeability is directly related to the flow capacity of hydrocarbon fluid through a rock. **Figure 2** reveals several orders of magnitude difference between the permeability of conventional and unconventional rocks ─ In other words, shale gas is much more difficult to produce than conventional natural gas.

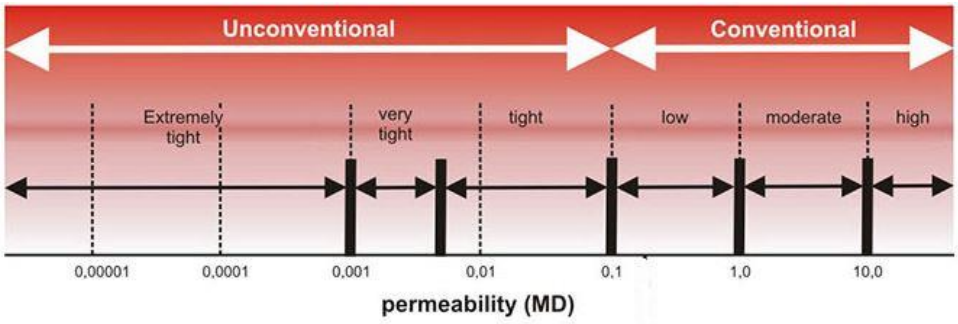

Figure 2: Permeability of Unconventional and Conventional rock [Source: Modified from Polish Geological Institute, 2014; https://infolupki.pgi.gov.pl/en/gas/petrophysical-properties-shale-rocks].

The pore-throat size of conventional reservoir rock is greater than 2μm (Nelson 2009). But in the shale formation, there is a wide range of pore-throat size, which can be from several nanometers to hundreds of nanometers (Zhang et al. 2016). The extremely small pore size makes the study of hydrocarbon fluid in shale formation become challenging. In addition, the pore size distribution (PSD) has a large influence on the composition of a rock, total organic carbon (TOC), the maturity of organic matter and the original gas in place (OGIP).

1.2 Objectives and Problems Statement

Since doing laboratory experiments on shale rocks are extremely challenging and experimental results are highly uncertain, numerical modeling including molecular dynamics simulations and density functions with Equation of state are applied in this thesis to study the complex phase behavior of shale gas/oil under the confined and unconfined condition. In specific, the following problems have been studied:

1. In shale gas reservoir, the volume of adsorbed gas is a large portion of total gas in place (OGIP). The adsorption behavior is directly related to the gas storage mechanism. Core sample study shows that many pores in organic matter have a cylindrical shape, but the curvature effect on gas storage has not been studied. Therefore, the adsorption behavior and storage mechanism of shale gas under the reservoir conditions for cylindrical pores have been studied by a thorough comparison between the Lennard Jones Potential with Peng-Robinson EoS (LJ-PREoS) and equilibrium molecular dynamics simulation.
2. The phase behavior of hydrocarbon fluid happens anywhere in reservoirs. The phase envelope and flash calculations are two common methods that can determine the phase-state or composition fraction of hydrocarbon fluid under specified conditions. But when it comes to confinements, it is not easier to use either method to gain those fundamental understandings. With MD simulations, the coordinates, velocities, and interactions of all molecules can be recorded

whether in bulk or under confinement. Thus, with the knowledge of thermodynamics and kinetics, MD simulation has been processed and interpreted to study the phase behavior of hydrocarbon fluid.

3. The mixture of water/oil/CO_2 is an important system to tertiary oil recovery, especially for the immiscible CO_2 flooding and the in-situ CO_2 generation methods. From the technical point of view, two properties are relevant, namely, the self-diffusion coefficient of CO_2 and the CO_2 partition coefficient, which are directly related to the recovery efficiency. The comprehensive studies about these two properties in the flooding process are insufficient since it is very hard to study them through laboratory experiments. The methods with MD simulation were proposed to study the self-diffusion coefficient and partition coefficient of CO_2 from the water/oil/CO_2 systems.

1.3 Layout of the Thesis

Chapter 1 introduces the background of shale gas and the challenges/problems the petroleum engineer faced in shale gas development.

Chapter 2 provides a literature review about common models of studying the hydrocarbon fluid in nanoscale pore space.

Chapter 3 studies the adsorption behavior of shale gas in cylindrical nanopore and develops a new framework to study the original gas in place (OGIP).

Chapter 4 focuses on the study of hydrocarbon phase behavior by using Molecular

dynamics simulation.

Chapter 5 investigates the self-diffusion coefficient and partition coefficient of CO_2 through the tertiary-CO_2 flooding processes.

Chapter 6 covers the conclusions of this thesis and future work recommendations.

Chapter 2: Literature Review on Shale Gas Behavior in Confined Spaces

2.1 Background

The original gas in place (OGIP) of a shale formation is an important parameter which directly determines whether the company will develop this shale formation or not. There are three ways to store natural gas in shale formations, as free gas in the inorganic pore space, as adsorbed gas in the organic matter, and as dissolved gas in water and oil (Curtis 2002). It should be noted that the volume of adsorbed gas can be 20% ~ 80% of the total gas in place (Curtis 2002; Zhao et al. 2015). Therefore, it is important to investigate the adsorption behavior of shale gas in the nanopores and estimate the OGIP of shale gas reservoirs. The mechanism of physical adsorption is molecular interaction between hydrocarbon fluid molecules and pore wall, which is related to the pore size, composition, pressure, and pore structure (Saito and Foley 1991; Schettler and Parmely 1989).

2.2 Classical Models of Studying Shale Gas Adsorption Behavior

There are several methods to study the adsorption mechanism of gas in shale nanopores. The most common method for studying adsorption behavior is the Langmuir isotherm model (Langmuir 1918). And there are two basic assumptions in the Langmuir

model: 1. constant temperature and pressure; 2. there is only one single layer of molecules adsorbed on the pore wall. These assumptions limit the model's application in a shale formation since multiple-adsorbed layers are formed under high pressure (Yu et al. 2014; Dhanapal et al. 2014). On the basis of classical Langmuir isotherm model, the BET isotherm model with assumptions such as homogeneous solid surface and no lateral interaction between molecules, is another adsorption model specially designed for the condition with multiple-adsorbed layers (Brunauer et al. 1938). But the BET model is not applicable for hydrocarbon fluid in supercritical condition.

SLD combined with Equation of State (EoS) has been proved to be a reliable method to study many phase behaviors of hydrocarbon fluid in Nano-scale condition. In the simplified local density (SLD) model, the molecular interaction between hydrocarbon molecules and solid surface is considered, and SLD model can be applied in wide-range pressure condition (Rangarajan et al. 1995). Because SLD model overcomes the limitations of the Langmuir model and BET model, it was selected as a theoretical method to study local density distribution (or adsorption behavior) of shale gas in most research studies. Charoensuppanimit et al. (2016) investigated the adsorption of gases in slit pores under high pressure by combining experimental data and SLD-PR model (Peng-Robinson Equation of state). Ma and Jamili (2014) studied the different effects of slit-pore structure such as pore sizes, pressure, and temperature on the phase behavior of shale gas via SLD-PR model. Pang et al. (2016) used SLD-PR model and Experimental methods to study the adsorption behavior of shale gas in slit-pore. In reality, pore

structure types in shale gas reservoir are very complex and different, such as slit pores, cylindrical pores, conical pores, and ink bottle-shaped pores (Li et al. 2016; Chalmers et al. 2012; Sing 1985; Yang et al. 2014). Curtis et al. (2010) observed some rock samples from Barnett, Eagle Ford, Horn River through SEM images and found that many nanoscale pores in kerogen have a round cross-section. A pore with different structure normally has its unique characters. For example, compared with the slit-pore structure, the cylindrical pore has a curvature effect, which will enhance the interaction between adsorbate molecule and pore-wall (adsorption effect increase). Most of the existing SLD models focus on studying shale gas in slit nanopores, but the study of shale gas in cylindrical nanopores is insufficient.

2.3 Molecular Simulation on Studying Shale Gas Adsorption Behavior

2.3.1 Background of Molecular Simulation

Molecular simulation is a computer simulation method developed in the early 20th century, which generally focuses on simulating the behavior of molecules. Molecular simulation is constructed using mathematical fundamentals and principles of physics and chemistry. To petroleum engineering, molecular simulation provides a new way to generate data and the main advantages are to reduce the research cost, for example, by reducing or avoiding experimental equipment cost, to provide improved safety, and to gain insight from conditions and cases otherwise inaccessible to experiments, such as ultrahigh temperature and pressure, nanoscale confinement, etc. Based on different

frameworks, molecular simulation methods are classified as molecular dynamics (MD) simulation, Monte Carlo (MC) method, and quantum mechanics calculations. Quantum mechanics calculations are to describe systems with bond breaking and formation. With electrons as the basic descriptor of quantum mechanics calculations, properties such as charge density, bond sequence, molecule energy, and chemical reactions can be obtained. MC method relies on probability and the theory of statistics. By using random numbers and advanced sampling techniques, phase behaviors can be studied via MC calculations. MC methods are also widely adopted to study adsorption processes.

2.3.2 Applying Molecular Simulation in Hydrocarbon Development

In petroleum engineering, molecular simulations are widely adopted to study hydrocarbon fluid properties under different conditions. For example, the molecular simulation was used to investigate adsorption/desorption phenomena of hydrocarbon molecules in nanoscale confinements (Ambrose et al. 2010; Wang et al. 2016; Collell et al. 2015; Liu et al. 2016; Pitakbunkate et al. 2016; Zhang et al. 2017). It was also used to study the phase behavior of fluid under a confinement condition, which is totally different with behavior in the conventional reservoir (Jin and Nasrabadi 2018; Li et al. 2014; Jin and Firoozabadi 2015; Ma and Jamili 2014). Furthermore, molecular simulations have been also performed to study transport mechanism of shale fluids, such as the transport diffusivity of methane in nanopores(Wu and Firoozabadi 2018), the displacement mechanism between $CH4/CO_2$ in shale formation(Zhang and Cao 2016) and the slip-flow of methane at the surface of shale nanopores (Umeda et al. 2014).

Even though molecular simulation can be used to overcome some limitations of laboratory experiments, direct using the tool on OGIP will be time-consuming. For example, the pore size distribution (PSD) is a critical factor to estimate OGIP, since the range of nanopore size in organic-rich shale can be from 2 nm to more than 50 nm (Ross and Bustin 2007), it is computationally expensive to study adsorption behavior/or local density distribution of hydrocarbon fluid in different pore-size by constructing a simulation model for each size every time.

Chapter 3: Studying the Shale Gas Behavior in Cylindrical Nanopore Through the Combination of SLD Model and MD Simulation

Tolbert and Wu (2015) developed a new SLD-PR model for cylindrical pore structure and used this new model to estimate the OGIP of shale gas reservoir, but their new cylindrical-SLD model has not been validated yet. The combination of Molecular simulation and SLD model was applied in this chapter, that is molecular simulation was used to validate new cylindrical SLD model, and then applied proven SLD model with PSD concept to study OGIP.

3.1 Methodology of Cylindrical PR-SLD Model

The Simplified Local Density model with Equation of State is based on the theory of chemical equilibrium, which states that the chemical potential of every molecule at any position within a nanopore is same if the system is in an equilibrium-state, no matter the molecule is adsorbed on pore surface or stays free in center. The main application of SLD model is to find the local density distribution profile of hydrocarbon fluid within nanopore. The density distribution profile of hydrocarbon fluid can reveal the adsorption phenomenon directly, and all kinds of fluid density in nanopore can be derived from its local density distribution profile, such as bulk-phase density, adsorption-phase density, and average fluid density.

The local density distribution for hydrocarbon molecule in a cylindrical nanopore is a function of their position r (**Figure 3**). At different position r, the density of hydrocarbon fluid is different. For example, in some large size nanopore under specified condition, for r getting closer to pore wall, the density of hydrocarbon fluid increase because adsorption effect of pore-wall on fluid molecule gets stronger. In contrast, for r getting closer to the center of pore, the density of fluid will decrease and become closer to its bulk-phase density, because the interaction between pore-wall and the fluid molecule will decrease with their distance increase.

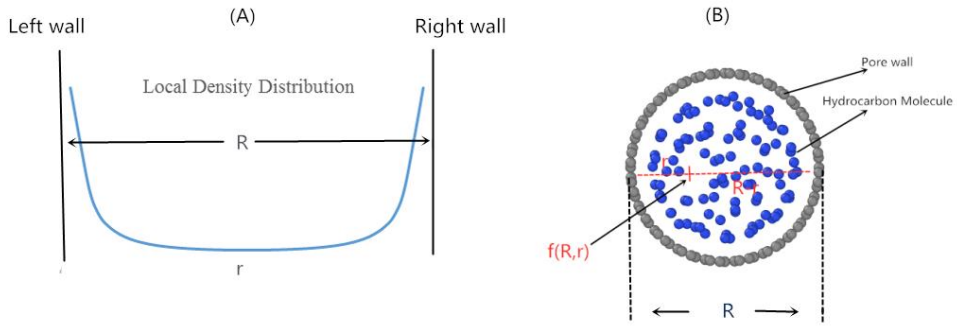

Figure 3: Cylindrical-SLD model. (A): Local density distribution profile; (B): MD model of the cylindrical Nanopore.

The methodology in detail of the new SLD model was attached in **Appendix A**.

3.2 Molecular Dynamics Simulation

As the introduction about Molecular simulation mentioned before, there are two most common models in molecular simulation: 1. The Molecular dynamics simulation (MD); 2. Monte Carlo simulation (MC). The main idea of MD is dependent on time-dependent analysis, for example, the coordination of atoms was determined via solving Newton's law of motion at every timestep. For MC simulation, generating the

configuration of the system to analyze a particular property via statistical Sampling method is the main theory, and MC simulation is not time-dependent modeling. There are two main reasons for us to choose the MD simulation in this study. At first, the cylindrical-SLD model was applied in nanoscale pore space, which means it is very hard to validate the model without special lab-equipment. At second, the main theory of SLD model is dependent on the equilibrium-state of system. So, in order to cooperate with the theory of SLD model, by using molecular dynamics simulation to study the behavior of hydrocarbon fluid molecule (density distribution, coordination variation, etc.) in an Equilibrium-state, which is a more time-saving method than MC simulation.

3.2.1 Structure of Graphite Nanotube

Methane is a typical component of hydrocarbon fluid in most shale gas formation (Freeman et al. 2012; Aljamaan 2015), so methane was chosen for studying the single-component system. The second case was for a binary system with about 80% methane and 20% n-butane in mole fractions to represent a multiple components system. In addition, both of the two systems were simulated in a perfect and simply graphite-nanotube (also called carbon-Nanotube) to represent a confined condition, because organic matter is one of the major storage media for shale gas (Mavor 2003) and the graphite material was used to represent the organic matter in this study. In order to validate the cylindrical SLD model, a nanopore with 10 nm diameter and 12 nm length was fixed for both the MD simulation and SLD model.

LAMMPS (Large-scale Atomic/Molecular Massively Parallel Simulator) was

used to run all simulation cases, and PACKMOL was used to construct CNT. The carbon nanotube was made of pure carbon atoms, and every carbon atom has 1.42 A diameter (**Figure 4** shown).

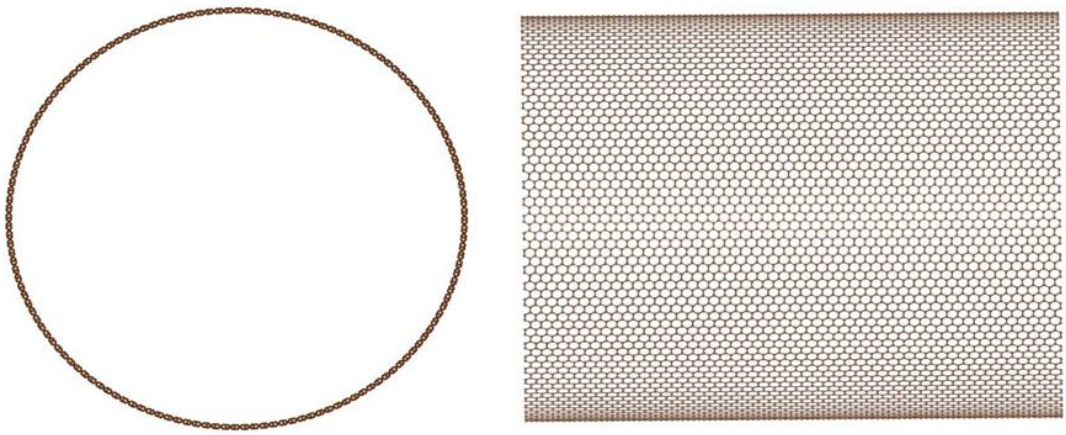

Figure 4: 2 sides view of graphite nanotube; the radius of nanotube = 5nm, length of nanotube = 12 nm, there is a total of 14800 carbon atoms in this CNT.

Normally, there are 2 typical types of carbon nanotube, one is the Zigzag pattern, the second one is the Armchair pattern. The difference between these two types of CNT is structure-sequence of carbon atoms and **Figure 5** displays their difference directly:

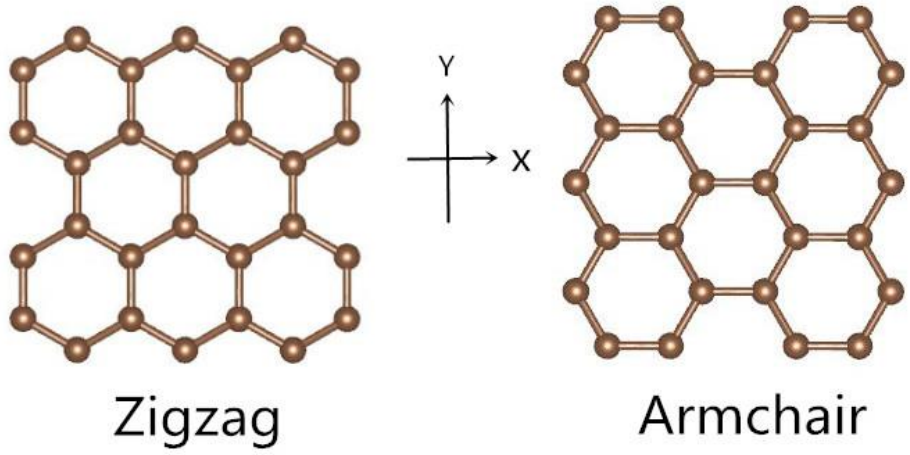

Figure 5: Two common structures of Carbon Nanotube: Zigzag (left) and Armchair (right).

The Armchair pattern was selected in this work. Both of these 2 types can be used in this study because the interaction between hydrocarbon molecules and wall of CNT is, in fact,

the interaction between the carbon atom and hydrocarbon molecule. And the sequence of carbon atom has no crucial influence on natural property of carbon atom itself, so the factor of structure-sequence in CNT can be negligible in this work.

3.2.2 Simulation Details

In LAMMPS, the formulas of total potential energy for the system are shown below:

$$E_{total} = E_{bonded} + E_{non-bonded} \quad (3.2.1)$$

$$E_{bonded} = E_{bond} + E_{angle} + E_{torsion} \quad (3.2.2)$$

$$E_{bond} = \frac{1}{2} * k * (r - r_0)\text{^}2 \quad (3.2.3)$$

$$E_{angle} = \frac{1}{2} * k * (\theta - \theta_0)\text{^}2 \quad (3.2.4)$$

$$E_{torsion} = \frac{1}{2} * v_1 * (1 + cos\phi) + \frac{1}{2} * v_2 * (1 - cos2\phi) + \frac{1}{2} * v_3 * (1 + cos3\phi) + \frac{1}{2} * v_4 * (1 - cos4\phi) \quad (3.2.5)$$

$$E_{non-bonded} = 4 * \varepsilon_{ij} * [\left(\frac{\sigma_{ij}}{r}\right)^{12} - \left(\frac{\sigma_{ij}}{r}\right)^{6}], \ r < r_c \quad (3.2.6)$$

$$\varepsilon_{ij} = \sqrt{\varepsilon_{ii} * \varepsilon_{jj}} \quad (3.2.7)$$

$$\sigma_{ij} = (\sigma_{ii} - \sigma_{jj})/2 \quad (3.2.8)$$

The E_{bonded}(3.2.2) means energy involve 2-,3-,4-body interactions of bonded atoms. For example, E_{bond} (3.2.3) means 2-body interaction energy which describes the harmonic vibrational motion between 2 bonded atoms. The E_{angle}(3.2.4) means 3-body interaction which describes the angular vibration motion between 3 boned atoms. The $E_{torsion}$(3.2.5) means 4-body interaction which describes the angular spring motion between the planes formed by the first 3 consecutive atoms and last 3 consecutive atoms,

like an example shown in **Figure 6**:

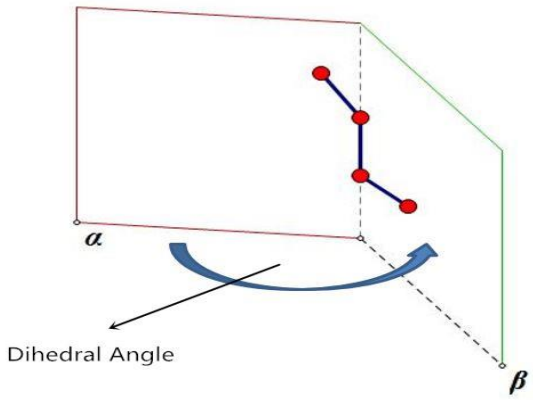

Figure 6: Example of Dihedral Angle.

The $E_{non-bonded}$ (3.2.6) means the potential energy from the interaction between all different pairs of atoms, which exclude pairs of atoms already in a bonded term. Also, Equation (3.2.6) is the formula of classical 12-6 Lennard-jones potential energy function, which describes the interaction force between molecules including attractive force and repulsive force. The r_c is the cut-off radius, and it was set to be 15 angstroms in the simulation. The L-J potential energy of two atoms will be ignored if the distance (r) between them is larger than r_c.

In order to support potential energy function, the TraPPE-UA force field was used for methane and butane system. TraPPE-UA style refers to Transferable Potentials for Phase Equilibria United-Atom force field, which is designed particularly for the n-alkanes group (Martin and J Siepmann 1998). To maximize simplicity and transferability, the TraPPE-UA force field parameters for a given pseudo-atom do not depend upon its neighboring pseudo-atoms (Martin and Siepmann 1999). For example, in a hydrocarbon molecule, a carbon atom and the hydrogen atoms around it are defined into a pseudo-

atom group (for example, in an N-butane molecule, CH3- is one type of pseudo-atom group, and -CH2- is another type of pseudo-atom group, as **Figure 7** shown). So, in the TraPPE-UA style, for a hydrocarbon molecule itself, the bonded interaction (E_{bonded}) is mainly caused by its pseudo-atom group, not a single C atom or H atom. Also, for the different molecules, the interaction energy ($E_{non-bonded}$) is still mainly caused by the different pseudo-atom groups. **Figure 7** also displays the difference between All-Atom style and United-Atom style clearly for an N-butane molecule.

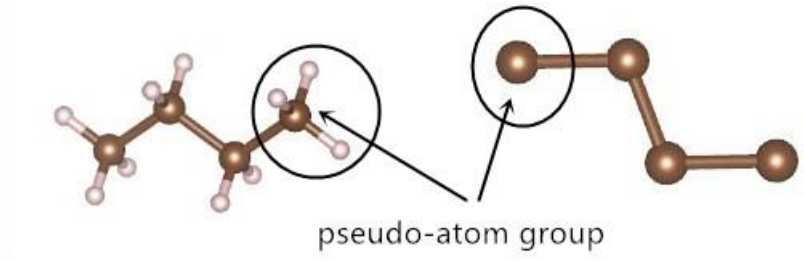

Figure 7: Comparison of United-Atom style and All-Atom style; Example of the pseudo-atom group.

Figure 8 displays the composition of shale gas in four U.S. shale reservoirs and it is no doubt that the methane is the major component in shale gas.

Barnett Shale Gas Composition					
Well	C1	C2	C3	CO2	N2
1	80.3	8.1	2.3	1.4	7.9
2	81.2	11.8	5.2	0.3	1.5
3	91.8	4.4	0.4	2.3	1.1
4	93.7	2.6	0	2.7	1

New Albany Shale Gas Composition					
Well	C1	C2	C3	CO2	N2
1	87.7	1.7	2.5	8.1	N/A
2	88	0.8	0.8	10.4	N/A
3	91	1	0.6	7.4	N/A
4	92.8	1	0.6	5.6	N/A

Marcellus Shale Gas Composition					
Well	C1	C2	C3	CO2	N2
1	79.4	16.1	4	0.1	0.4
2	82.1	14	3.5	0.1	0.3
3	83.8	12	3	0.9	0.3
4	95.5	3	1	0.3	0.2

Antrim Shale Gas Composition					
Well	C1	C2	C3	CO2	N2
1	27.5	3.5	1	3	65
2	57.3	4.9	1.9	0	35.9
3	77.5	4	0.9	3.3	14.3
4	85.6	4.3	0.4	9	0.7

Figure 8: Typical components of shale gas in four U.S shale reservoirs (Bullin and Krouskop 2009).

In the single-component system, the shale gas was represented by methane molecules

only. In the multi-component system, the shale gas was represented by mixing methane and N-butane molecules. The United-atom style of the methane molecule and N-butane molecule are shown in **Figure 9**.

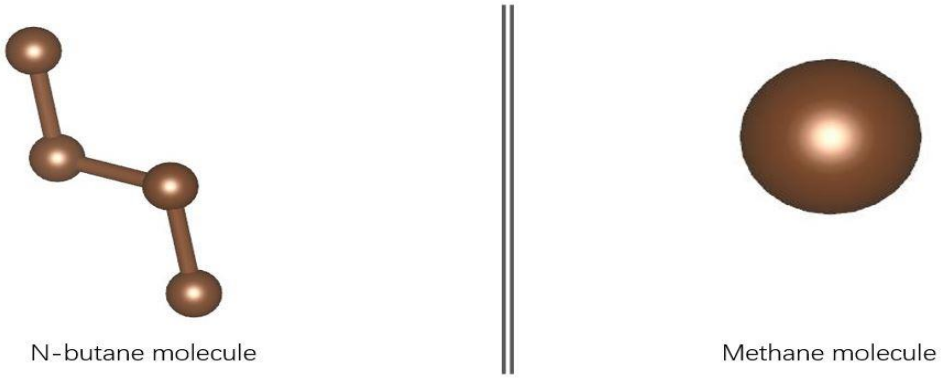

Figure 9: United-atom style for methane and N-butane molecule.

The parameters of TraPPE -UA force field for methane and N-butane molecule are shown in **Table 1**:

Atom Group	*σ*	*ε/kB*		
CH4	3.73	148		
CH3-	3.75	98		
-CH2-	3.95	46		
Carbon (C)	3.4	28		
Bond	***k***	***r0***		***Harmonic***
CH3-CH2	100	1.54		
CH2-CH2	100	1.54		
Angle	***k***	***θ***		***Harmonic***
CH3-CH2	62.1	114.0		
Torsion	***v1***	***v2***	***v3***	***v4***	***OPLS***
CH3-CH2-CH2-CH3	1.411	-0.2710	3.1450	0	

Table 1: TraPPE-UA force field parameters for methane and N-butane molecule.

In addition, periodic boundary conditions are applied to all three directions of the simulation box (P-P-P boundary condition). The gas reservoir temperature is set to be 200 °F. The volume of graphite nanotube should be fixed in the simulation, therefore the NVT ensemble was selected. The NVT ensemble means the system will be in a constant number of atoms, constant volume, and constant temperature condition. In order to investigate the behavior of local density distribution under different pressure, pressures of 500 psi, 1000 psi and 2000 psi, were simulated for both the single-component system and multi-component system. Different pressure requires the number of hydrocarbon

molecules to be different in simulation for each scenario. The PR-EoS (Peng-Robinson Equation of state) was used to calculate the number of molecules that need to be added for different pressure-case. For each case, molecules were placed randomly in CNT. Also, in equilibrium MD simulation, the useful information of the target system must be collected in its equilibrium-state condition, so the total run time for each pressure-case was set to be 20 ns to guarantee the final condition of the system would be in an equilibrium state.

3.3 Single-component System and Multi-component System

3.3.1 Single-component System

The initial set of single-component system is shown in **Figure 10A** which is the random placement of methane molecules in CNT, and **Figure 10B** shows methane molecules at equilibrium state after simulation. **Figure 10B** shows that the density of methane molecule close to the pore wall is higher than that at the center of CNT. The final local density distribution of C1 under different pressures from the MD simulation and cylindrical-SLD model were compared in **Figure 12** and **Figure 13**.

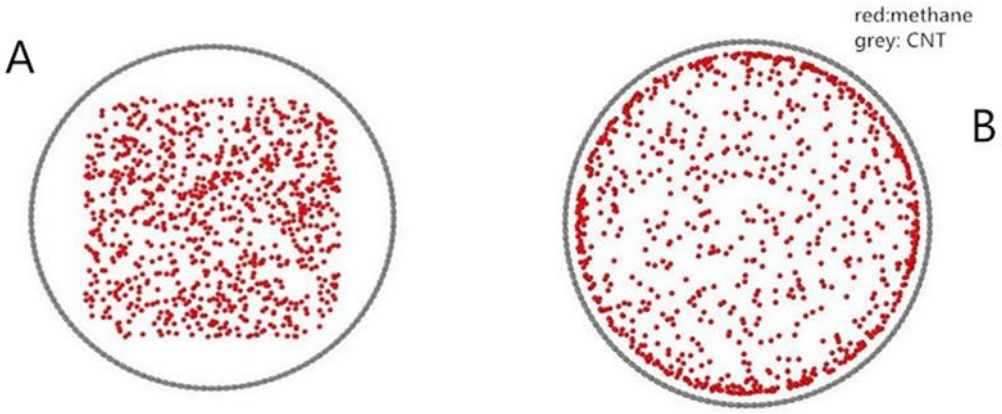

Figure 10: Snapshots of Pure-C1 system at 500psi and 200F, red = methane molecules, there is a total of 882 methane molecules in this case. (A): At time=0ns, Initial-state (B): At time =16ns, Final equilibrium-state.

3.3.2 Multi-component System

The multi-components system was represented by mixing methane molecules and N-butane molecules at the molar ratio of 4:1. In addition, the competitive adsorption between each component can be investigated in the multi-component system. Its initial set of MD simulation was random placement of methane and N-butane molecules in CNT (**Figure 11A** shown). **Figure 11B** shows molecular distribution at the equilibrium state of the system. There is a large portion of molecules adsorbed on pore wall, but most of the molecules are N-butane molecules (blue molecules).

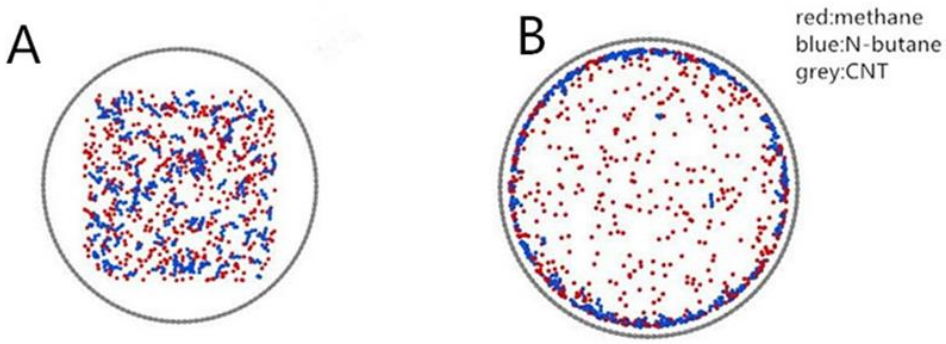

Figure 11: Snapshots of Mixture-C1/C4 system at 500psi and 200F, Blue = N-butane molecules, Red = methane molecules. There are 140 C4 molecules and 560 C1 molecules in this case. (A): At time=0ns, Initial-state (B): At time =19ns, Final equilibrium-state.

Other settings of the multi-component system such as NVT ensemble, periodical boundary, were the same as single-component system. The local density distribution profiles of mixture fluid under different pressure (500 psi, 1000 psi, and 2000 psi) from the MD simulation and cylindrical-SLD model were shown in **Figure 15** to **Figure 17**.

3.4 Results and Discussion

Part I: Single-component System

Figure 12 and **Figure 13** show the methane molecule distribution at the pressure of 500 psi and 1000 psi respectively. Because of the symmetrical property of local density distribution profile, the results shown are just about a half region of the pore (from pore-center to pore-wall, 0 to 5nm). The blue line represents local density distribution of C1 from MD simulation and the red line represents local density distribution from the cylindrical-SLD model. The grey dots represent the bulk phase density of methane under specified P/T. The bulk phase means the methane molecule is under non-confinement

effect, which means it is in the free gas phase.

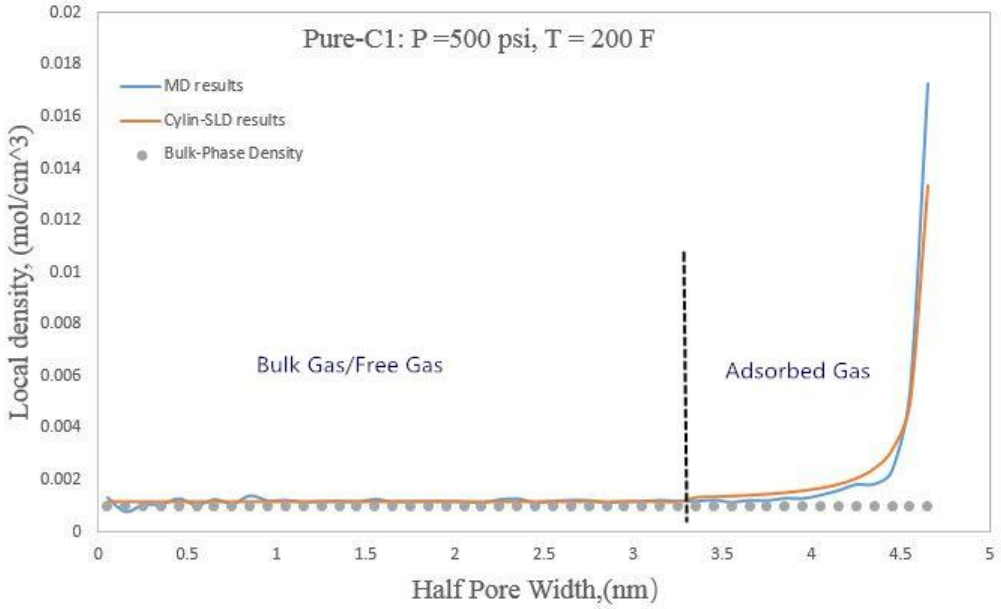

Figure 12: Local density distribution of Pure-C1 Gas at 500psi and 200F in the half-pore region.

From **Figure 12**, the free-methane gas and adsorbed-methane gas can be distinguished through their local density distribution. The density of free-methane gas is almost the same as its bulk phase density and the density of adsorbed-methane gas is higher than its bulk phase density, due to the interaction between the pore wall and methane molecules. As the distance gets closer to the pore wall, the adsorbed gas density increases

significantly.

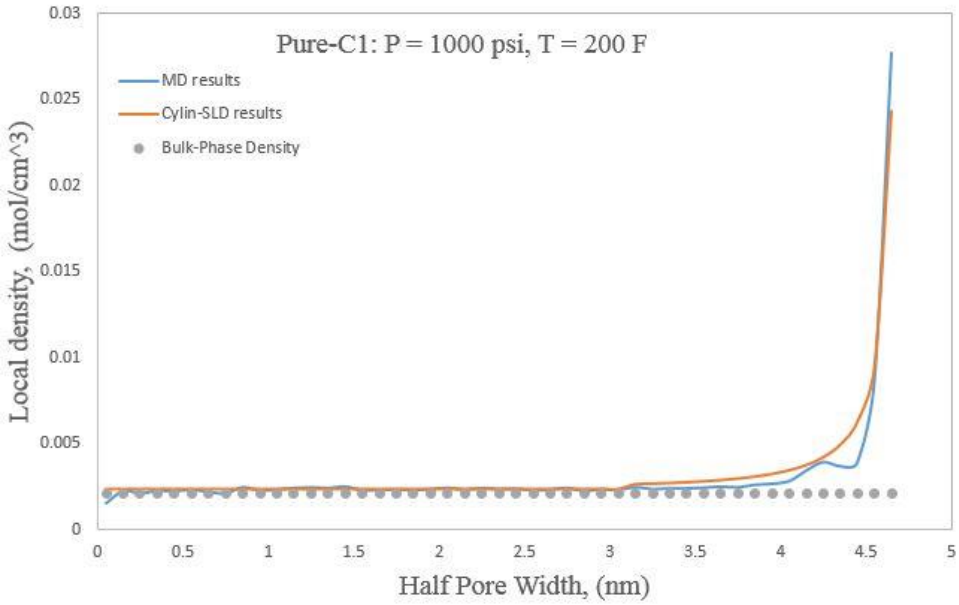

Figure 13: Local density distribution of Pure-C1 Gas at 1000psi and 200F in the half-pore region.

In **Figure 12** and **Figure 13**, it is no doubt that the MD simulation results and cylindrical-SLD model results match very well. It is very clear to see that as distance getting closer to pore-wall, especially from 4.3 nm ~ 4.8 nm, the density of methane molecules increases dramatically because of the stronger adsorption effect. There is no result in the region from 4.8 ~ 5 nm, and this is because the diameter of a methane molecule is about 4 nm (radius is 2 nm), which means the effective pore width for calculation is $R - 2 \times r_{methane}$ (4.8 for half-pore; 9.6 for entire-pore).

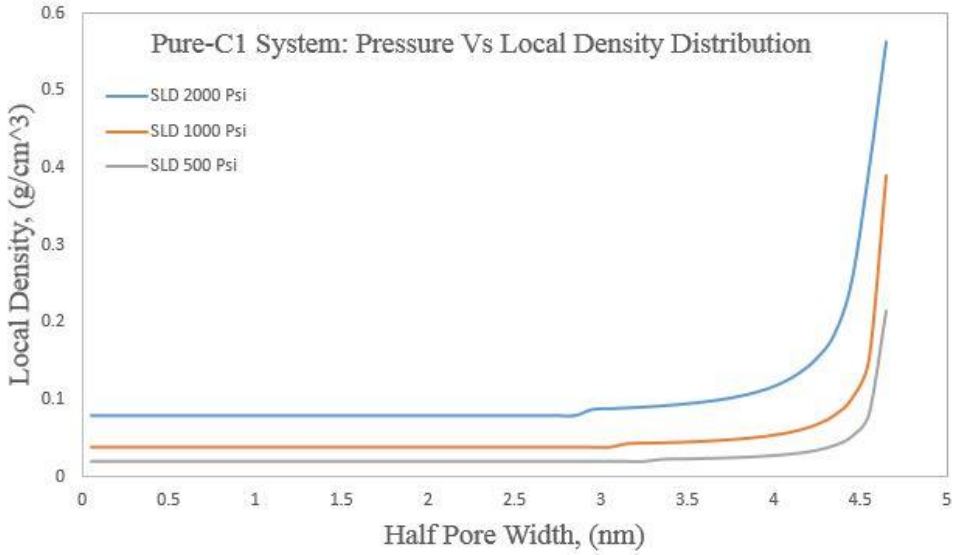

Figure 14: Local density distribution of Pure-C1 Gas at 500psi,1000psi,2000psi in half-pore region.

Figure 14 shows the local density distribution of C1 fluid under different pressure, it is clear to see that the density of free-C1 gas and adsorbed-C1 gas increase as pressure increase, especially for the density of adsorbed-C1 gas which increases dramatically. Therefore, it can be concluded that higher pressure can make more methane molecules become adsorbed gas.

Part II: Multi-components System

The simulation results for the multi-components under the pressures of 500 psi, 1000 psi, and 2000 psi from two methods were compared with each other and are shown in **Figure 15** to **Figure 17**. In **Figure 15**, the free-mixture gas and adsorbed-mixture gas were determined based on the same way via their local density distribution profile.

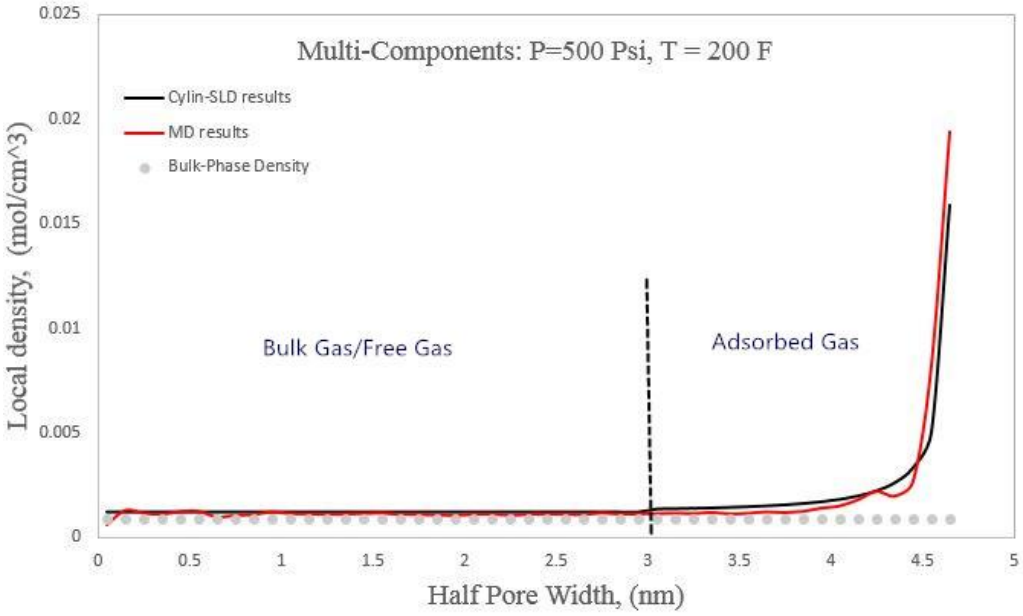

Figure 15: Local density distribution of Mixture-C1/C4 Gas at 500psi and 200F in the half-pore region.

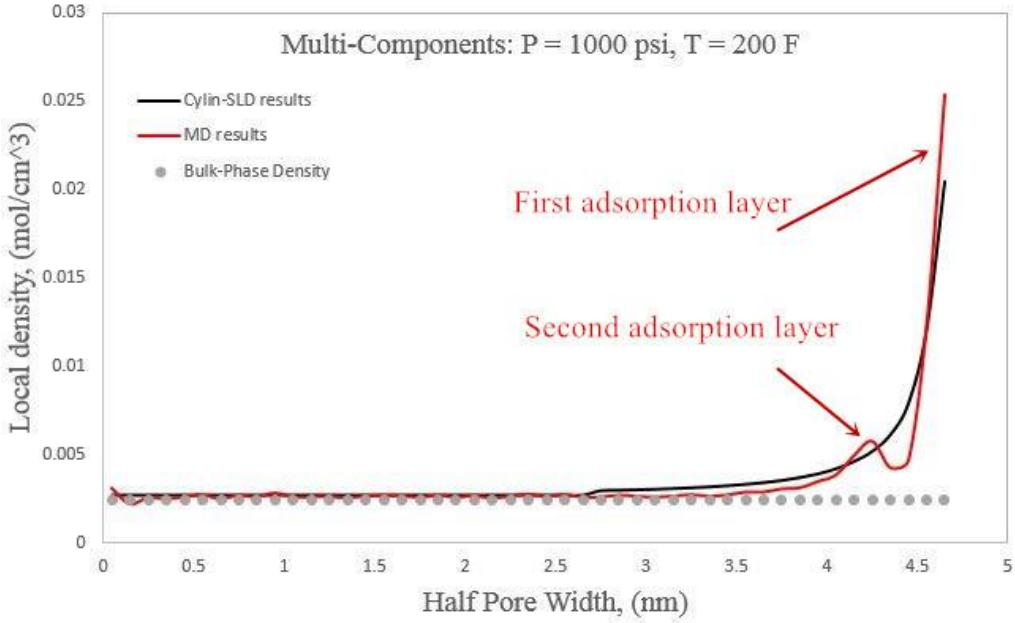

Figure 16: Local density distribution of Mixture-C1/C4 Gas at 1000psi and 200F in the half-pore region.

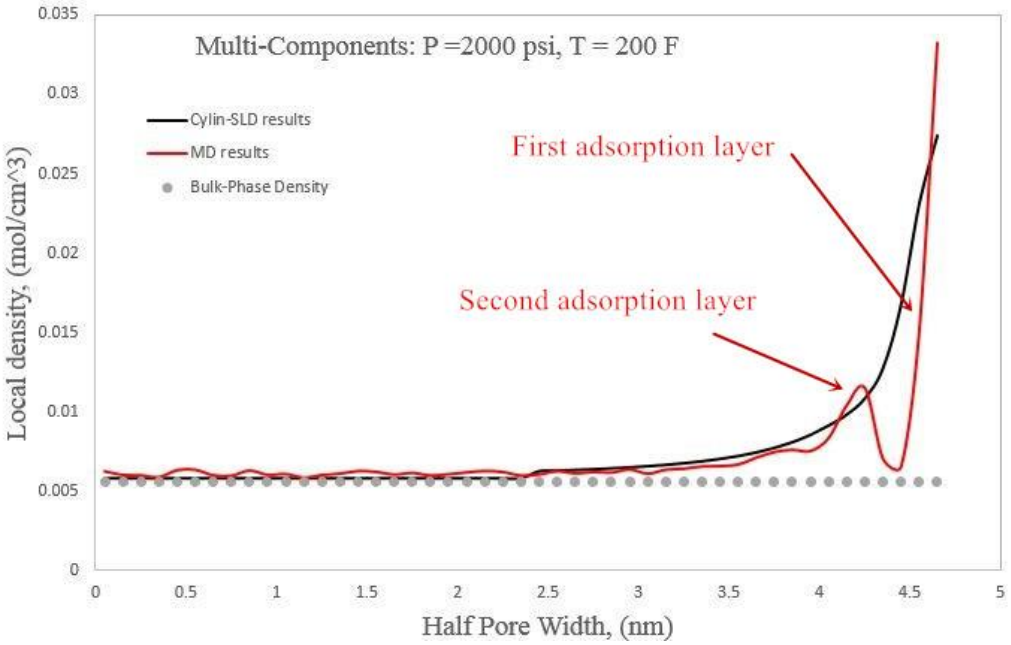

Figure 17: Local density distribution of Mixture-C1/C4 Gas at 2000psi and 200F in the half-pore region.

From the general results above, the local density distribution profile of two methods matched well with each other. Furthermore, from the MD results in **Figure 16** and **Figure 17**, the second adsorption layer appeared behind the first adsorption layer. Because higher pressure will enhance the molecular interaction between fluid-fluid and fluid-pore wall, which will force molecules to stay together and form a new adsorption layer.

In order to investigate the competition adsorption between methane and N-butane molecule, the Composition distribution graph of each component versus location r was plotted in **Figure 18** and **Figure 19** for 1000 psi and 2000 psi. In general, the number of butane molecules accumulated more and more with distance getting closer and closer to the wall. The number of methane molecules decreased with distance getting closer to the wall. Therefore, the effect of pore wall on the N-butane molecule is stronger than it on the methane molecule, which means the organic pore wall has stronger adsorption effect

on the heavier and more complex component.

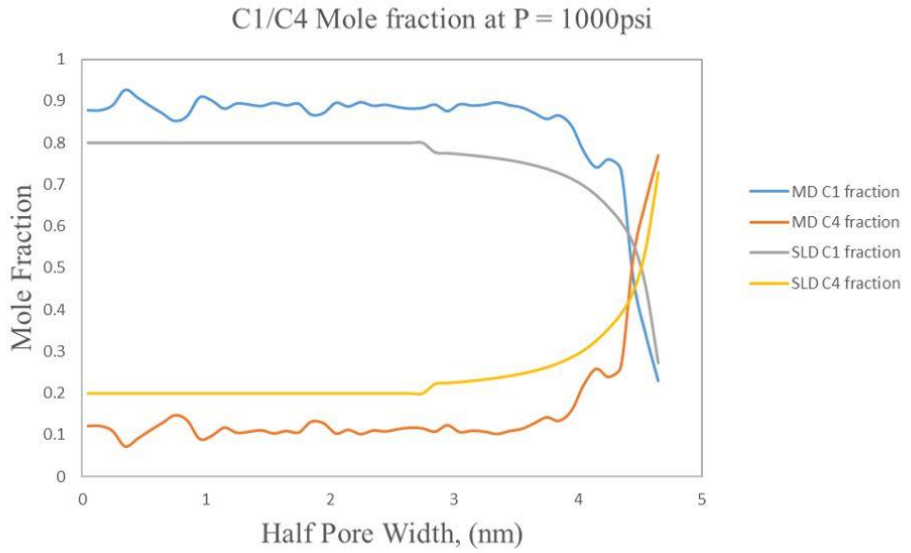

Figure 18: Comparison of Composition fraction of C1/C4 from two methods in the half-pore region.

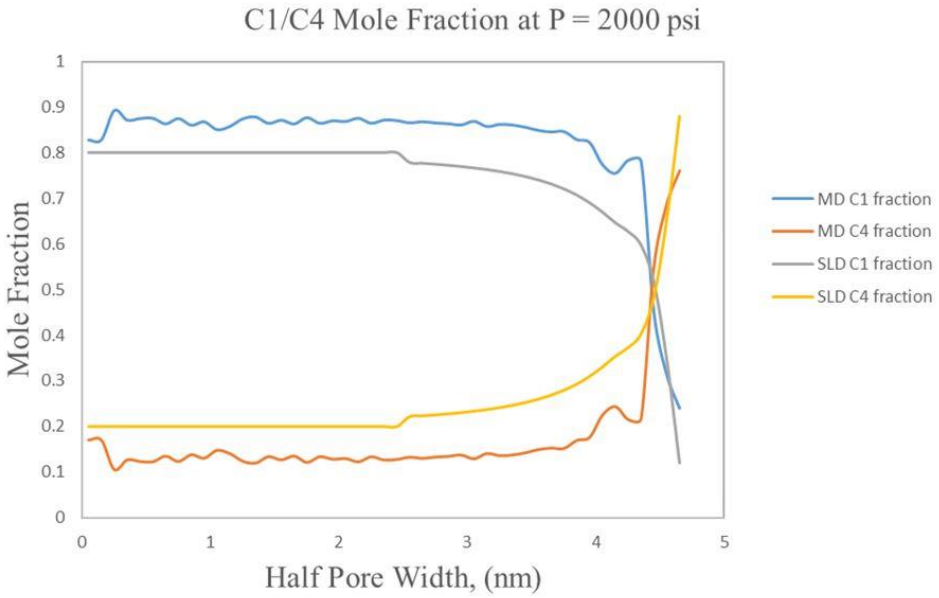

Figure 19: Comparison of Composition fraction of C1/C4 from two methods in the half-pore region.

In addition, another method by using the Number distribution graph from MD simulation was also applied to show competitive adsorption, as shown in **Figure 20**. The number percentage for each component i at location r is defined as:

$$\text{number of } i\ \% = \frac{number\ of\ Component\ i\ (at\ location\ \text{r})}{Total\ number\ of\ Component\ i} \qquad (3.4.1)$$

The case shown in **Figure 20** is C1/C4 mixture fluid under 500 psi and 200 F, and there are 140 butane molecules and 560 methane molecules (mole fraction 4:1) in the system. In the region from 4.5 nm to 4.8 nm, there are about 95.5% (67 out of 70) of C4 molecules and only 49.2% of C1 molecules (138 out of 280). From the Number distribution analysis, the adsorption effect from pore-wall is stronger on C4 molecules than C1 molecules, and this conclusion is the same as the conclusion from Composition distribution analysis by using both two models.

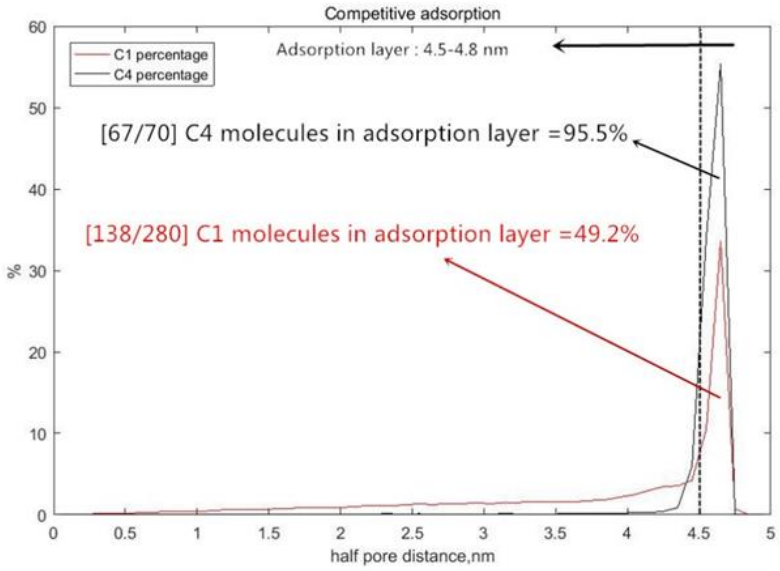

Figure 20: Number distribution of C1/C4 from MD simulation in the half-pore region.

The main theory of physical adsorption is molecular interaction (also known as van der Waals force) between hydrocarbon molecule and carbon nanotube. The magnitude of physical adsorption is proportional to molecular polarizability because larger molecular

polarizabilities add more contribution to molecular interaction (Schettler and Parmely 1989). In contrast to methane molecule, N-butane molecule has a more complex structure with larger and stronger molecular polarizability, and this is why the pore wall has a stronger effect on N-butane molecule than methane molecule.

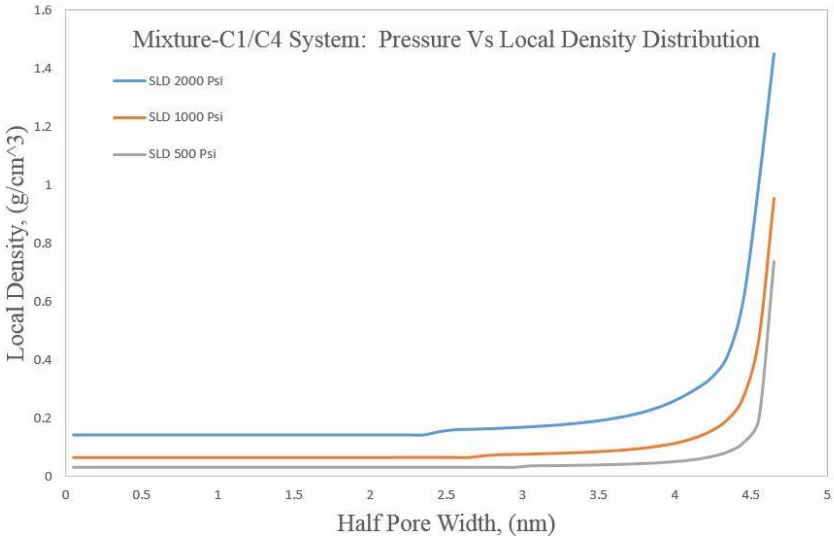

Figure 21: Local density distribution of Mixture-C1/C4 Gas at 500psi,1000psi,2000psi in the half-pore region.

From **Figure 21**, as pressure increase, no matter it is adsorbed gas or free gas, their density increases in general. By comparing with free gas, it is obvious that the density of adsorbed gas increases much more as pressure increase. And, from this point, because higher pressure will increase the density of both free gas and adsorbed gas, it means that there will be a larger volume of the natural gas stored in organic matter under a higher reservoir pressure. In addition, as pressure decrease because of reservoir depletion, some adsorbed gas will desorb as free gas.

3.5 A new Framework of OGIP Estimation

After the cylindrical-SLD model was successfully validated, this model can be applied to estimate original gas in place (OGIP) if other reservoir parameters are given. In shale gas reservoir (dissolved gas in water and oil were ignored), the total gas volume can be divided into two parts, gas reserved in organic matter and inorganic matter, and the general Equation is:

$$G_{gas-total} = G_{gas-organic} + G_{gas-inorganic} \tag{3.5.1}$$

Furthermore, natural gas mainly is in adsorbed phase stored in organic matter like kerogen, because molecular interaction exists between gas molecule and composition of organic matter such as carbon atoms, oxygen atoms, hydrogen atoms, etc. Unlike the organic matter, free gas is mainly stored in inorganic matter. In this framework, all of the gas stored in the inorganic matter was assumed as free gas, and the density of free gas was represented by its bulk-phase density under a specified reservoir condition:

$$G_{gas-inorganic} = \frac{V_{total} \times \emptyset_{inorganic} \times (1 - S_w - S_{oil}) \times \rho_{bulk}}{\rho_{std}} \tag{3.5.2}$$

For gas stored in organic matter, there are free gas and adsorption gas in coexistence:

$$G_{gas-organic} = G_{free-organic} + G_{ads-organic} \tag{3.5.3}$$

The density of free gas in organic matter was still represented by its bulk-phase density.

$G_{free-organic}$

$$= \frac{\sum_n (V_{total} \times \emptyset_{organic} \times PSD_n \times (1 - S_{w_n} - S_{oil_n} - S_{ads_n}) \times \rho_{bulk_n})}{\rho_{std}} \quad (3.5.4)$$

n was defined as the size of organic pores from range 1 to N nm:

$$\text{n} = 1,2,3 \ldots \text{N (PSD range, 1 nm to N nm)} \quad (3.5.5)$$

S_{ads_n} was defined as saturation of adsorbed gas in any kind of organic pore (size n), and S_{free_n} was defined as saturation of free gas in this pore. ρ_{bulk} means the bulk-phase density of hydrocarbon fluid under specified reservoir condition. $\overline{\rho_{\text{ads}_\text{n}}}$ in Equation (3.5.6) was defined as the average density of gas in the adsorption layer (the average density of adsorbed gas). In order to find S_{ads_n} and $\overline{\rho_{\text{ads}_\text{n}}}$ in Equation (3.5.4) and Equation (3.5.6), the adsorption layer and adsorbed gas in any-size(n) organic pore should be determined through its local density distribution profile from the cylindrical-SLD model at first.

$$G_{ads-organic} = \frac{\sum_n (V_{total} \times \emptyset_{organic} \times PSD_n \times (1 - S_{w_n} - S_{oil_n} - S_{free_n}) \times \overline{\rho_{ads_n}})}{\rho_{std}} \quad (3.5.6)$$

There is no standard rule to define the adsorption layer in shale nanopores because the definition of the adsorption region (adsorption layer) can be different from person to person. For example, Ma et al. (2016) defined the adsorption layer starting at where the local density is 1.15 times higher than bulk phase density. In my study, from the results (**Figure 12** and **Figure 15**), the adsorption region was defined starting at the location

where the local density is just higher than the bulk phase density. To avoid this ambiguous definition of adsorption layer, in the Equation (3.5.7), an average gas density of whole organic pore to include both free-gas density and adsorbed-gas density was developed:

$$\overline{\rho_{organic}}_n = \frac{[\,\rho_{bulk} \times A_{bulk} + \overline{\rho_{ads}} \times A_{ads}]_n}{A_{pore,n}} \tag{3.5.7}$$

$$A_{pore,n} = A_{bulk,n} + A_{ads,n} \tag{3.5.8}$$

$$G_{gas-organic} = \frac{\sum_n (V_{total} \times \emptyset_{organic} \times [PSD \times (1 - S_w - S_{oil}) \times \overline{\rho_{organic}}]_n)}{\rho_{std}} \tag{3.5.9}$$

After the average gas density in any-size organic pore was determined, the total gas in organic matter can be calculated through Equation (3.5.9). From Equation (3.5.1) to (3.5.9), all of the parameters to estimate OGIP were determined except pore size distribution (PSD).

3.5.1 Concept of Pore Size Distribution

Pore size distribution (PSD) is an important petrophysics property to study such as adsorption effect, diffusivity, permeability in the shale formation**.** In this work, the combination of cylindrical-SLD model and PSD was used to calculate the average gas density of different-size organic pore. There are several methods to measure pore size

distribution, such as Nuclear Magnetic Resonance (Prammer 1994; Sigal 2015), mercury injection capillary pressure method (Basan et al. 1997; Ghanbarian 2018), Brunaur-Emmett-Teller (Hinai et al. 2014), water adsorption isotherm method (Zolfaghari and Dehghanpour 2015). The main theory of Mercury injection capillary pressure method (MICP) is about measuring the injected volume of Mercury fluid that is forced into rock-sample. For small pores, the MICP method is unreliable because high injection pressure will compress the original pore space (Labani 2013). The Brunaur-Emmett-Teller (BET) method to calculate PSD is based on adsorption isotherm. But, the limitation of BET is that the different test fluids (such as N2, CO_2) used in adsorption isotherm test gave us different results of PSD for the same rock sample (Clarkson et al. 2013). Zolfaghari and Dehghanpour (2015) developed a new model with water adsorption isotherm to calculate PSD, and the advantages of their model are: 1). It can be applied in low vapor pressure; 2). the model can be used for small pores less than 1nm.

The reason Why the PSD is important in OGIP estimation is that different pore size will cause totally different adsorption/free phase of hydrocarbon fluid in pore space. For example, if the pore size is small enough, it is possible that all of the hydrocarbon fluid is in adsorption phase; but if the pore size is relatively large, both of adsorbed gas and free gas can exist in pore space. **Figure 22** to **Figure 24** show us the local density distribution of mixture fluid (C1/C4 mole fraction in 4:1) in different pore size at 2000 psi and 200 F.

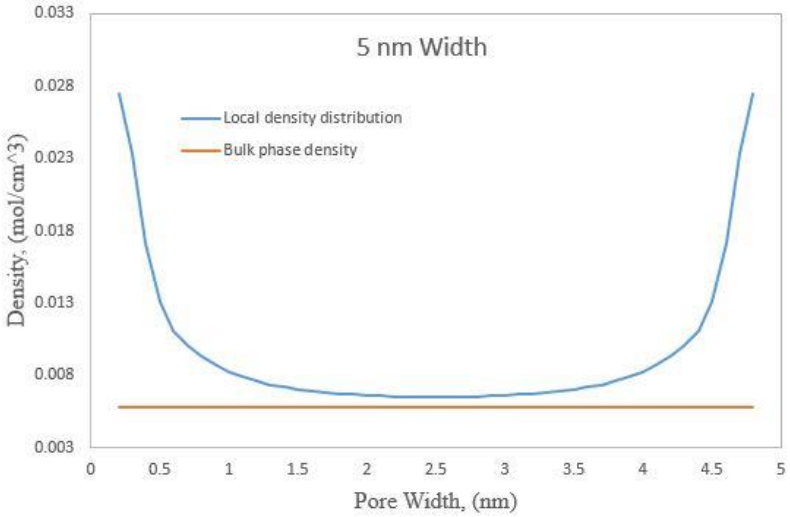

Figure 22: C1/C4 mixture fluid in 5nm cylindrical nanopore under 2000psi and 200F.The fluid in the center almost behaves like free gas.

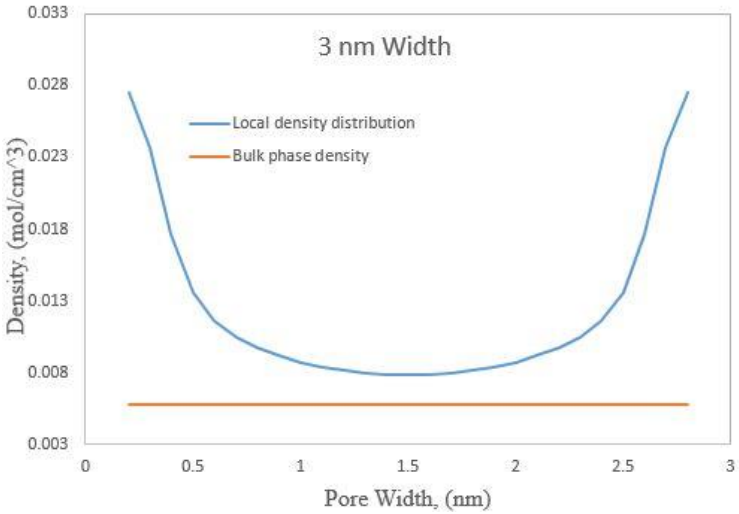

Figure 23: C1/C4 mixture fluid in 3nm cylindrical nanopore under 2000psi and 200F.

Figure 24: C1/C4 mixture fluid in 2nm cylindrical nanopore under 2000psi and 200F. There is only adsorbed gas in this pore size.

In **Figure 22**, because the pore size was large enough, some gas molecules in the center behaved like free gas (its density is very close to bulk phase density). In **Figure 24**, there is only adsorbed gas in whole pore space because of very small pore size.

The purpose in chapter 3.5.1 and 3.5.2 is just to show a case study for OGIP prediction by using the new framework, so the gamma distribution function was used to find a typical and representative PSD of a common shale-gas formation, which is enough for this part. The gamma probability density function was proved to be feasible in modeling real pore size distribution of shale gas reservoir (Joshi 2011). For gamma distribution used in this case, the shape factor was set to 3 and the scale factor was set to 2. Ko et al. (2017) concluded that nanopores (<50nm) are a large portion in shale formation rock, so the range of PSD was set from 0 to 25 nm in this case study. Finally, the PSD used in the case study was shown in **Figure 25**:

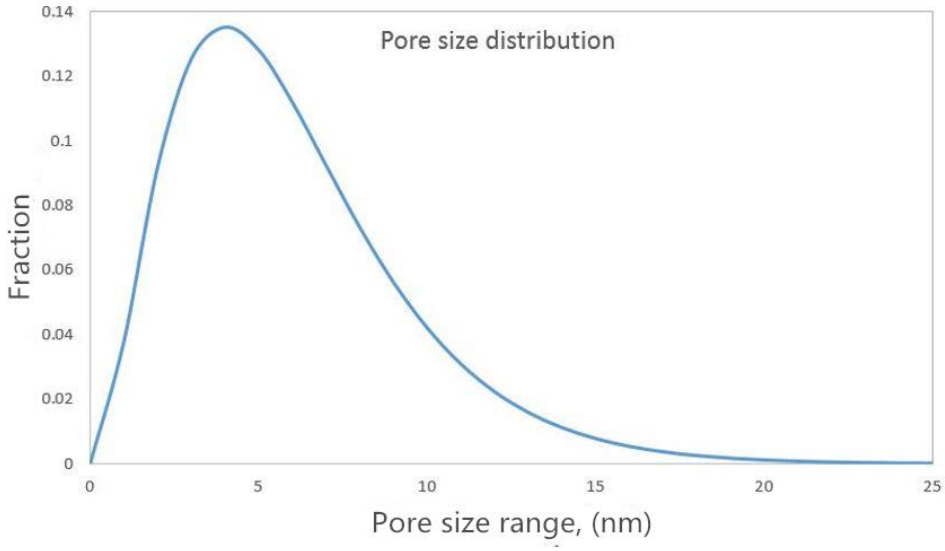

Figure 25: PSD of shale gas reservoir used in the case study. The range of pore size is from 0 to 25 nm.

After the PSD was determined, the final step was to collect basic information of a typical shale gas reservoir, such as porosity information, pressure, temperature, thickness, etc. Through some research studies about Barnett shale gas reservoir (Frantz et al. 2005; Jenkins and Boyer 2008; Kale et al. 2010; Aljamaan 2013), the necessary reservoir parameters for this case study were concluded in **Table 2**.

3.5.2 Case Study of OGIP Estimation

There are some assumptions in this case study. Firstly, the water saturation and oil saturation in all pore space were neglected, because it is a shale gas reservoir. Secondly, the adsorption effect just occurred in organic pore space, which means both free gas and adsorbed gas may store in organic matter. But, for inorganic matter, only free gas was considered because the adsorption effect was neglected. The basic information of the reservoir is listed in **Table 2**, and the results of OGIP calculated by the new framework were shown in **Table 3**.

Shale gas Reservoir information	
	Value
Reservoir Pressure (psi)	3000
Reservoir Temperature (°F)	200
Area of Well spacing (acre)	30
Thickness (ft)	100
Organic Porosity	5%
Inorganic Porosity	5.5%
Water saturation	0
Oil saturation	0
Pore size range (nm)	0 ~ 25

Table 2: Parameters of shale gas reservoir.

Results		
	Value	Units
OGIP in Inorganic	1446	MMscf
OGIP in organic	3717	MMscf

Table 3: Results of OGIP in organic matter and inorganic matter.

From the results in **Table 3**, the gas volume in organic matter is much larger than it in inorganic matter. I think this is a reasonable estimation, because: (1). The volume of adsorbed gas is a large portion of total gas in organic nanopores (especially for relatively small-size nanopore) and adsorbed-gas density is much larger than free-gas density (like the local density distribution profiles shown in chapter 3.4); (2). The PSD used in this case study mainly consists of small-size pores.

3.5.3 The Effects of PSD and Pressure on OGIP

From **Figure 22** to **Figure 24**, the results show us that the adsorbed/free gas in different pore size is significantly different. For example, if the pore size is small enough, there is no free gas in pore space (all of the gas is in adsorption phase); if the pore size is

large enough, there are free gas and adsorbed gas in coexistence. In addition, the range of pore size in shale gas formation can be from several nanometers to hundreds of nanometers. In order to study the effect of PSD on OGIP, three different pore size distributions were applied to calculate their OGIP by using the new framework. The adsorption effect was still assumed that it just exists in organic pore space.

Figure 26 distinctly shows the difference between these 3 PSD cases:

1. In case 1, the large portion of pore size is concentrated in the range from 0 ~ 5 nm.
2. In case 2, the large portion of pore size is concentrated in the range from 0 ~ 10 nm.
3. In case 3, the large portion of pore size is concentered in the range from 7 ~ 15 nm.

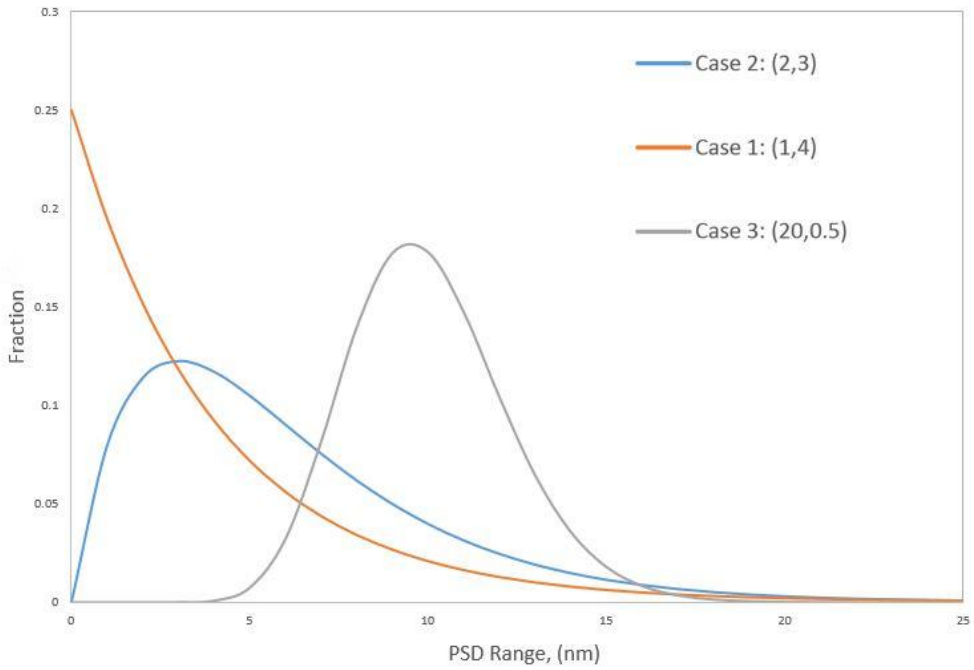

Figure 26: Three different pore size distributions.
Case 1 is the shape factor of 4 and scale factor of 1; Case 2 is the shape factor of 3 and the scale factor of 2; Case 3 is the shape factor of 0.5 and the scale factor of 20.

The OGIP values of these 3 cases were calculated in **Table 4** below:

OGIP Results					
Case 1		Case 2		Case 3	
k	Θ	k	Θ	k	Θ
1	4	2	3	20	0.5
Gas in Organic matter	Gas in Inorganic matter	Gas in Organic matter	Gas in Inorganic matter	Gas in Organic matter	Gas in Inorganic matter
4738 (MMscf)	1495 (MMscf)	4229 (MMscf)	1495 (MMscf)	2658 (MMscf)	1495 (MMscf)

Table 4: OGIP of 3 different PSD cases. The case 1 has the largest OGIP and Case 3 has the smallest OGIP. The OGIP of case 1 is almost twice more than case 3.

The results shown above are reasonable and acceptable, because the large portion of pore size in case 1 is very small (mainly 0 ~ 5nm) which cause strong adsorption effect on hydrocarbon fluid (like the case in **Figure 24**, there is even no free gas in such small pore); comparatively, most of the pore size in case 3 is relatively large, so there may be both free gas and adsorbed gas in pore spaces. Because the density of adsorbed gas is much greater than free gas, it is no doubt that case 1 has the largest OGIP value.

By using the same framework, the effect of pressure on OGIP was also investigated through a new case study. The basic reservoir-information of the new case study was taken from **Table 2** and the PSD was the same as **Figure 25**. The different pressures were tested in this case study: 500 psi, 1000 psi, 2000 psi, 3000 psi, 4000 psi, 5000 psi, and 6000 psi, and their results are shown in **Figure 27**.

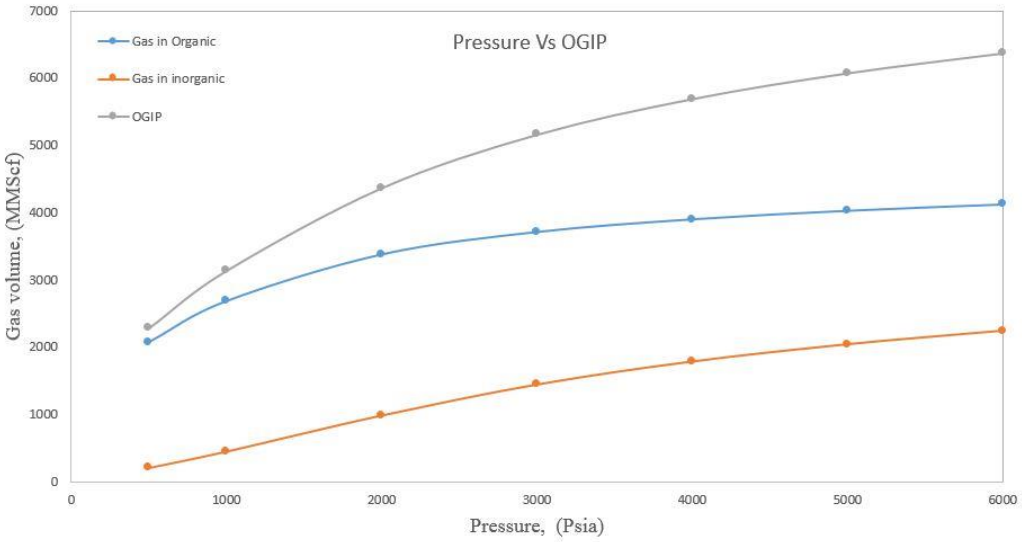

Figure 27: Total OGIP value under different pressures.

From results shown above, with the reservoir pressure increases, the total OGIP of the same reservoir increases because higher pressure will increase the density of both adsorbed gas and free gas.

Chapter 4: Study of Hydrocarbon Phase Behavior

4.1 Background

Phase behavior of hydrocarbon fluid is an interesting topic no matter in conventional resources development or unconventional resources development, as its related problems happen anywhere through reservoir development. The phase behavior of hydrocarbon fluid can not only affect the composition of production fluid at the surface but also affect the transport mechanism of fluid through the wellbore. There are several aspects of phase behavior about hydrocarbon fluid that are worth to study. The objects of chapter 4 are about studying the phase-state change of hydrocarbon fluid with MD simulation and determining the component fraction in each phase. The phase change of petroleum fluid (or hydrocarbon fluid) occurs in three places: 1. petroleum fluid in reservoir condition; 2. petroleum fluid through production wellbore; 3. production fluid through surface processing.

In the production period, the phase-state of petroleum fluid in the reservoir will change as pressure continuously declines. **Figure 28** displays the phase envelope of a typical volatile oil reservoir. It is clear that the single-phase petroleum fluid exists at the beginning period of production because the initial pressure is enough to maintain its initial phase. As the reservoir pressure declines, the single-phase turns into a two-phase

state and such fluid phase change in the reservoir can induce the composition change of production fluid at the surface, which is a common phenomenon that needs to be considered.

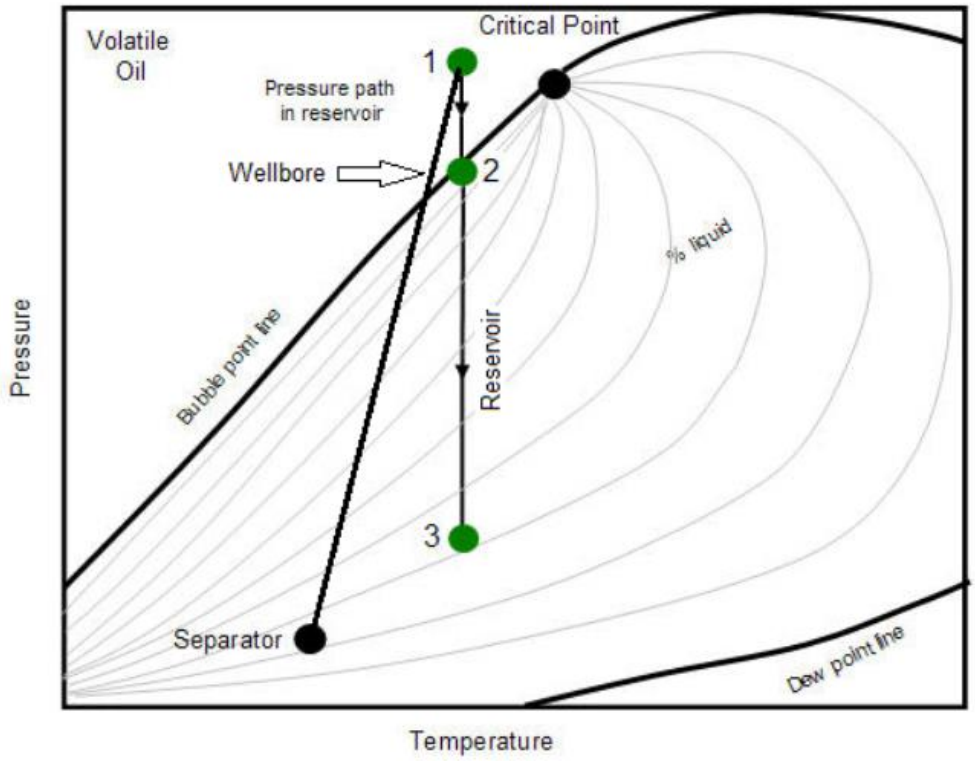

Figure 28: Phase envelope of a volatile oil reservoir. At point 1, the petroleum fluid is in the single-phase state; at point 3, the fluid is in the two-phase state [Source: IHS Inc, 2014].

The phase change of hydrocarbon fluid also happens in the production wellbore. The length of the wellbore from the bottom to the surface is too long to cause different pressure regions through the wellbore, which makes the fluid phase change as shown in **Figure 29B.** The phase change of fluid in production wellbore can cause problems such as liquid loading at the bottom of the wellbore, shut down the production immediately (**Figure 29A**).

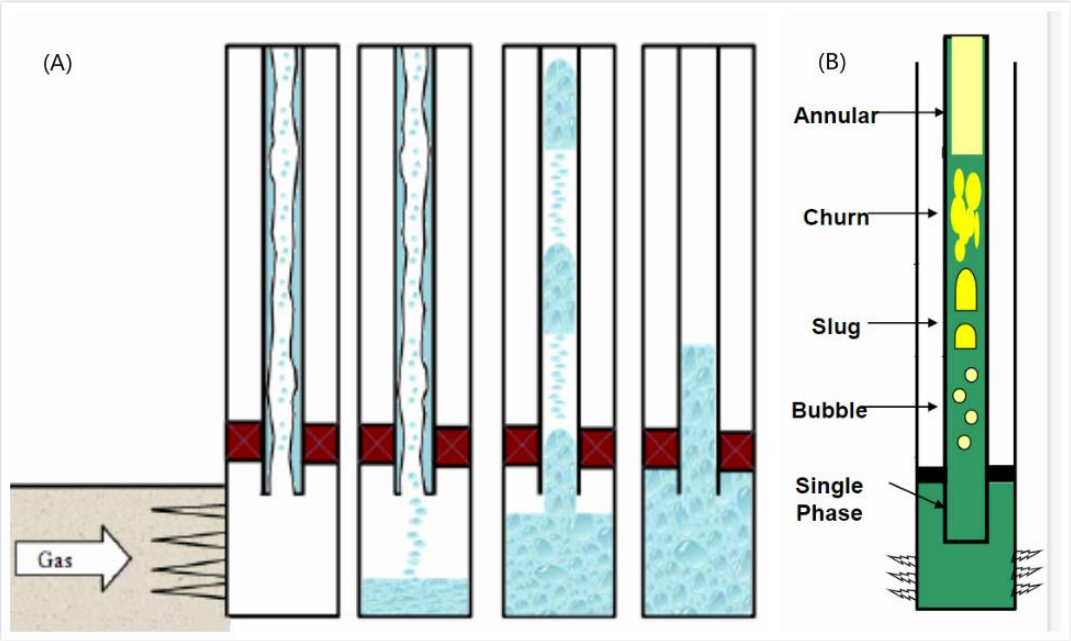

Figure 29: A): Liquid loading at bottom of the wellbore; B): Phase-state change and Flow-pattern change of production fluid through wellbore [Source: Modified from Class notes, Dr. Hamidreza Karami, The University of Oklahoma, 2018].

The third place of phase change is on the surface processing equipment such as in a separator. For a production fluid through the surface processing, the volatile components and heavy components are required to separate from each other. In the separation process, an original single-phase fluid will flash into a vapor phase and a corresponding liquid phase. It is necessary to determine component fractions in each phase.

4.1.1 Existing Methods for Studying Hydrocarbon Phase Behavior

The phase envelope (phase diagram) and flash calculation are two widely used methods that can help us to determine the phase-state/component fraction of hydrocarbon fluid under a specified condition. The phase envelope is usually expressed in the P-T or P-V diagrams. For example, **Figure 30** shows a P-T phase diagram of C1/C4 mixture fluid (4:1 in mole fraction). The phase-state of this fluid mixture under different P-T can

be clearly determined through this diagram.

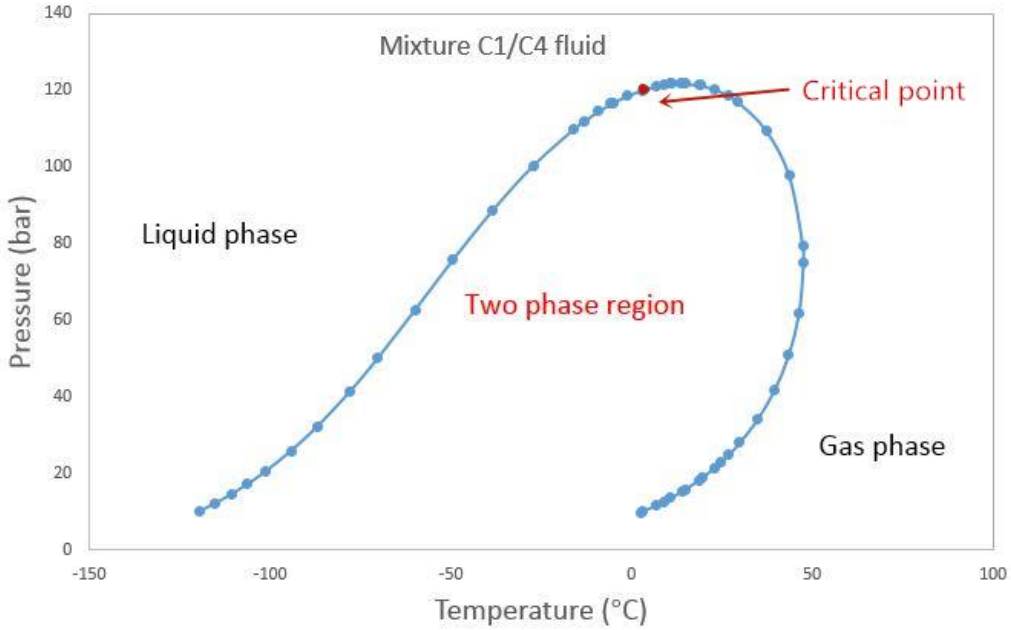

Figure 30: Phase diagram of C1/C4 fluid mixture(4:1 in mole fraction), produced by PVTsim software.

Flash calculation is a theoretical method that depends on the vapor-liquid phase in equilibrium, which is mainly used to decide the composition of each component in liquid/gas phases at a given temperature, pressure and initial mole-fraction of each component. There are two prerequisites for flash calculations. The first one is that we need to decide whether the initial single-phase fluid will flash into the two-phase state or remain its original phase-state under a given P/T condition. The second one is that the method is for systems with vapor/liquid equilibrium. Both the phase diagram and flash calculation have limitations to investigate hydrocarbon fluid phases under reservoir condition. Here we apply MD simulations to study phase properties of hydrocarbon fluids, using a C1/C4 mixture as a model system.

4.2 MD Simulation on Studying the Hydrocarbon Phase Behavior

4.2.1 Phase Property of a C1/C4 Mixture System

As shown in **Figure 31**, the system is composed of 2118 n-butane molecules and 12000 methane molecules, randomly placed in a 3-D cubic simulation box.

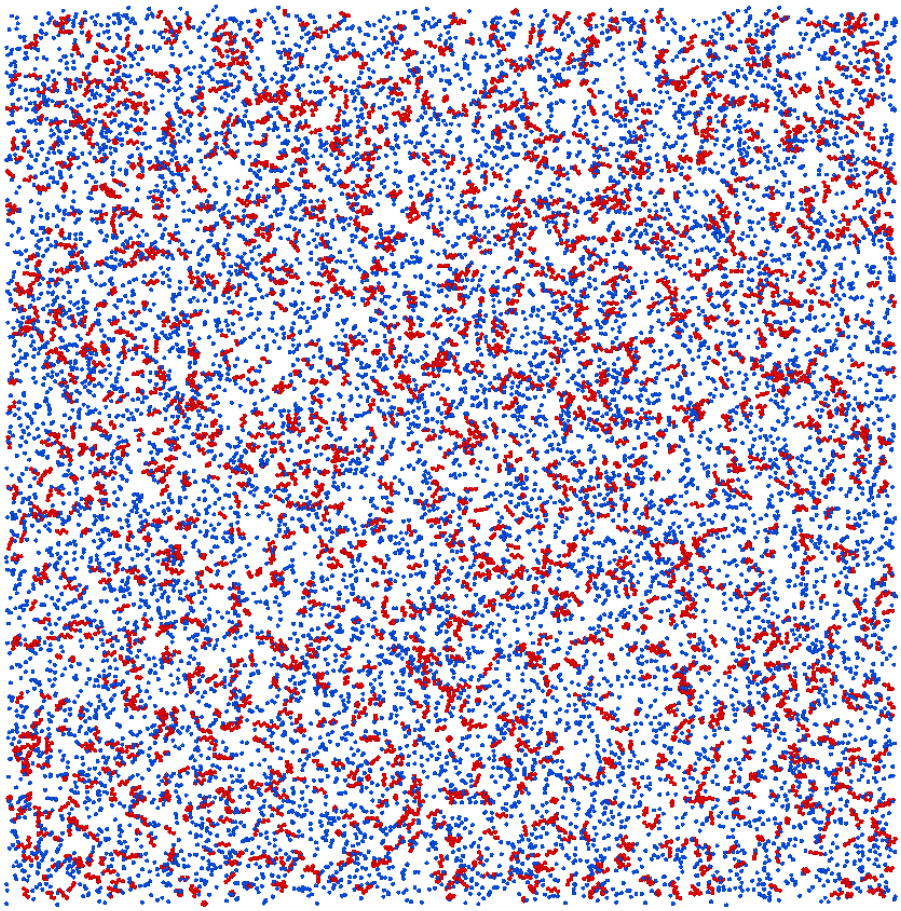

Figure 31: A MD model of C1/C4 fluid mixture in the bulk-phase state. The blue dots represent 12000 methane molecules and the red dots are 2118 n-butane molecules.

The NPT ensemble was applied in the calculation where the number of molecules, pressure (3.47 MPa) and temperature (195 K) hold constant. The total simulation time is 200 ns.

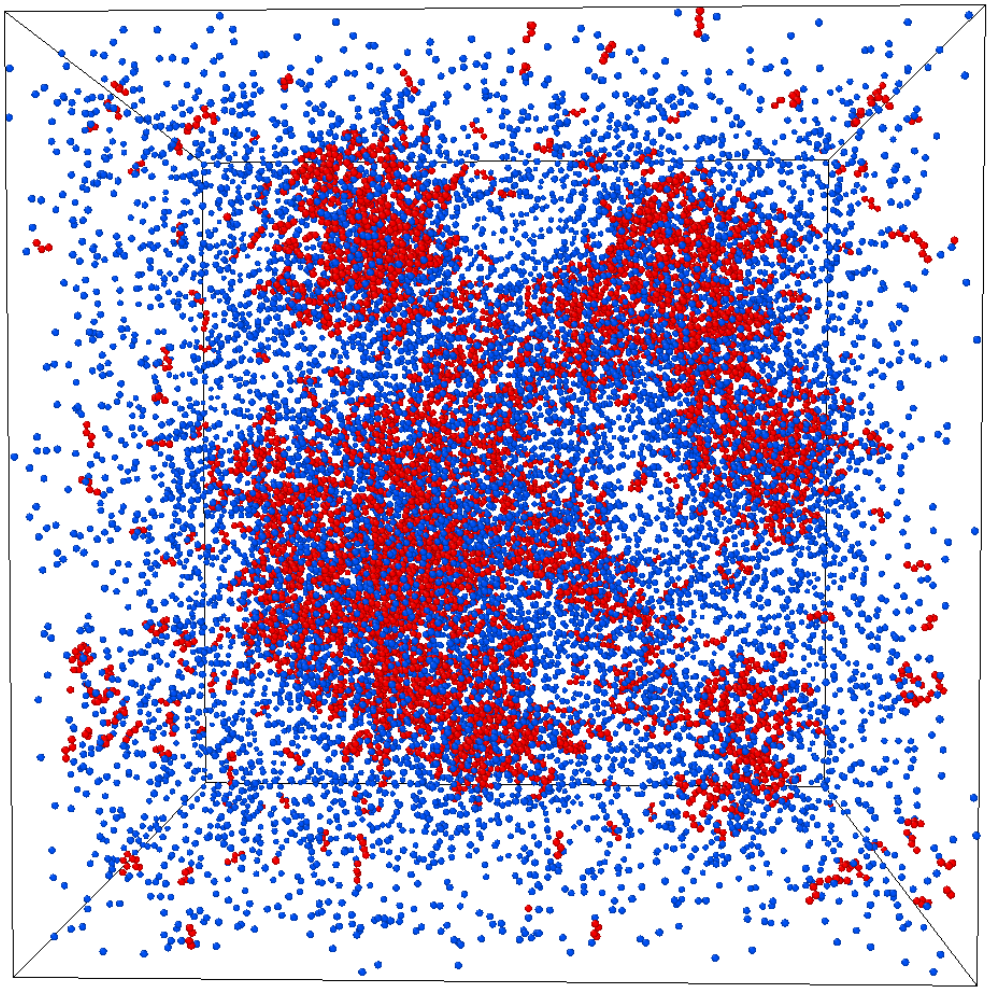

Figure 32: The MD simulation at time t = 0.5 ns, where molecules accumulate to form a liquid state.

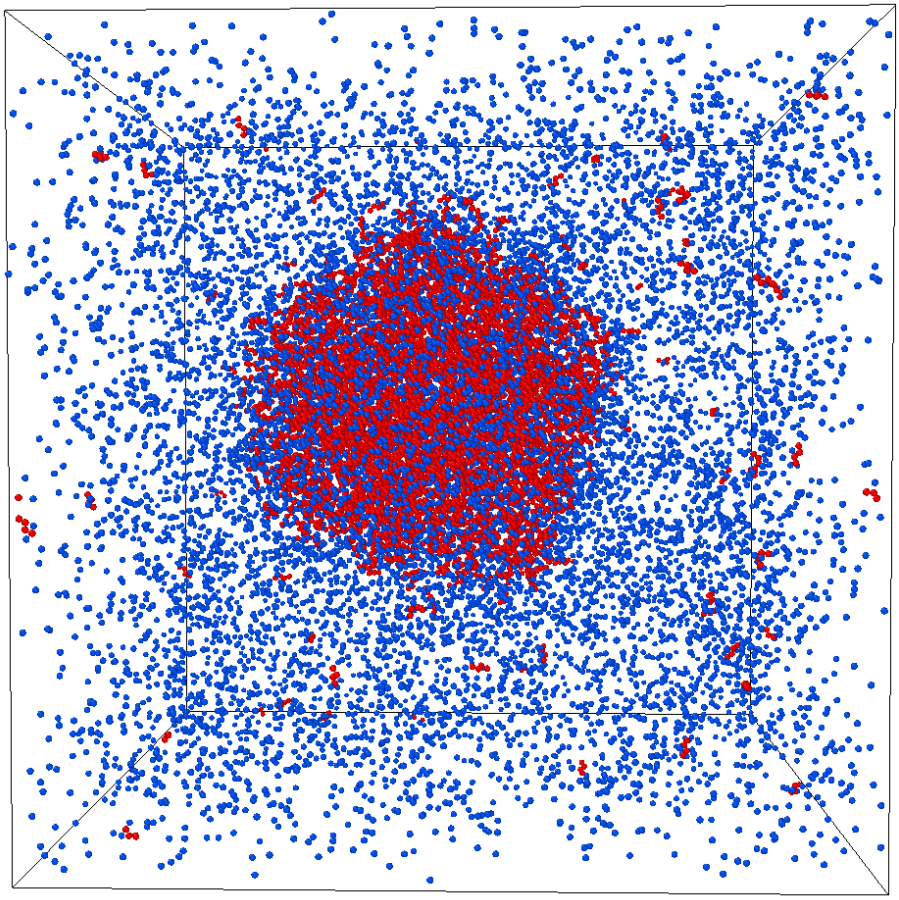

Figure 33: The MD simulation at time t = 72.1 ns, where a liquid state is clearly shown.

As shown in **Figure 32** and **Figure 33**, at the studied temperature and pressure, molecules accumulate and form a mixture of vapor/liquid phases. The reproducing of the vapor-liquid co-existent demonstrates that MD simulation is a proper tool to study phase properties of hydrocarbon fluids.

4.2.2 Determine Component Fraction of Co-Existing Phases

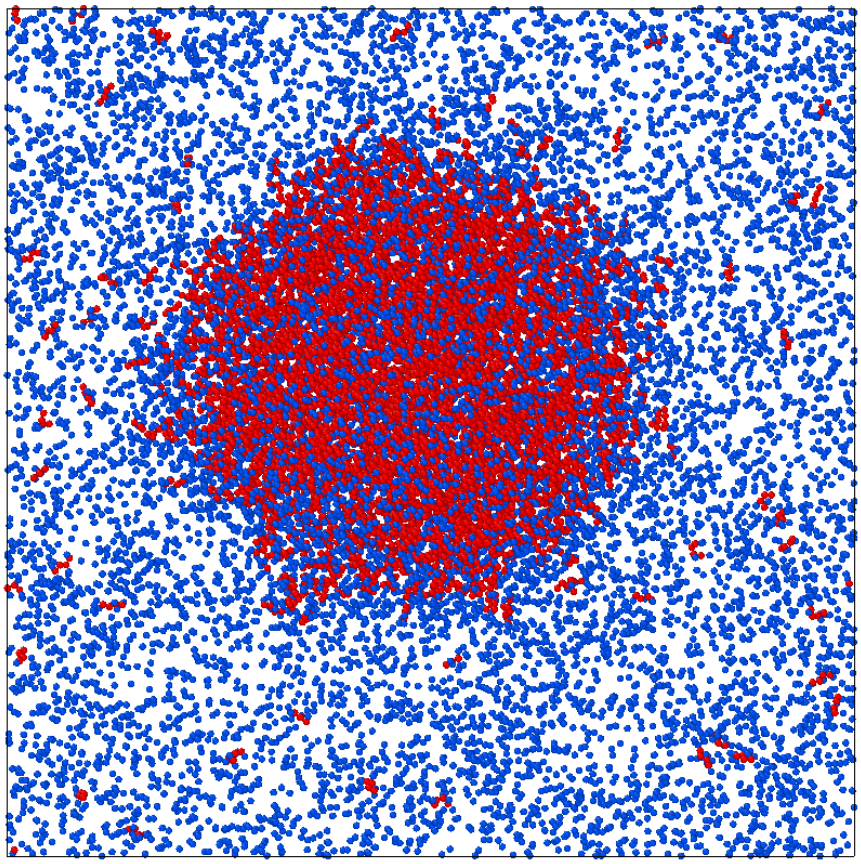

Figure 34: The equilibrium configuration of the C1/C4 vapor-liquid co-existence system.

Figure 34 shows the equilibrium configuration of the system at t = 72 ns. A liquid phase of the system has already been formed and stabilized. What remains unknown is the fraction of each component in the two phases. A quick estimation is to fit a cubic region to incorporate all liquid molecules, and then figure out how many C1 and C4 molecules respectively in the liquid region. As illustrated in **Figure 35**, the green cubic region has been placed to cover the size of the liquid droplet.

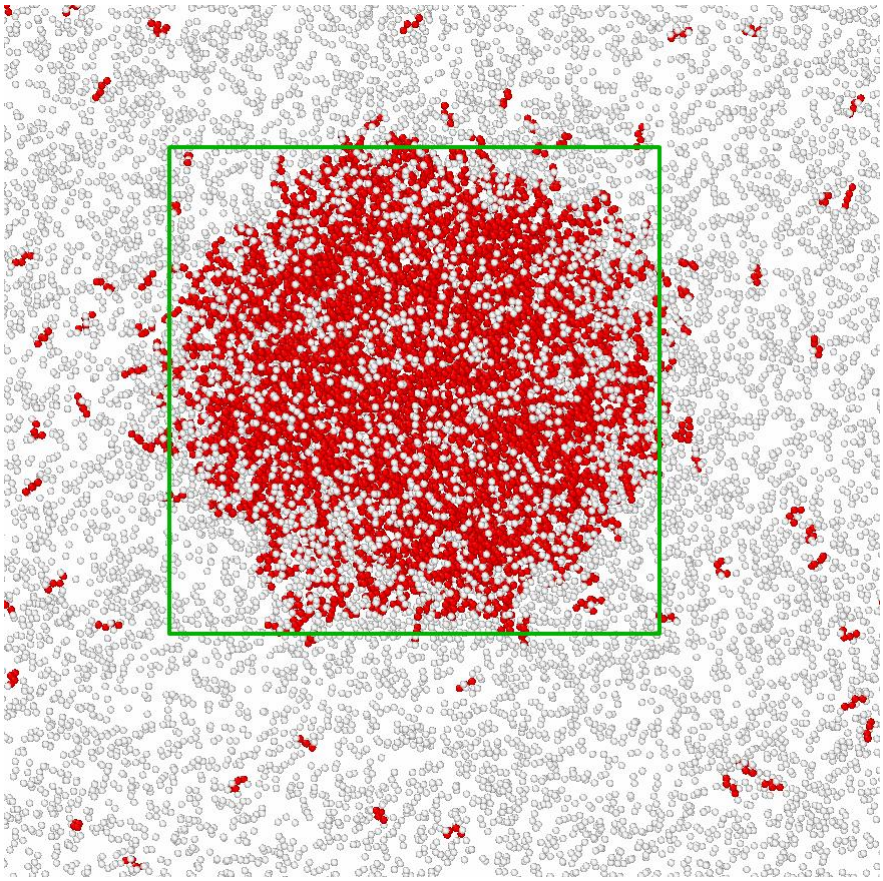

Figure 35: The identification of the liquid phase by fitting the droplet size via a cubic box.

All the molecules in the green box were assumed as a liquid molecule, and those located outside of the green box were assumed to be in the gas phase. After this, by comparing the coordinate regions, the number of C1 and C4 molecules could be identified. It is worth noting that using an approximate cubic shape to fit the liquid droplet will bring forth a large absolute error. One way to improve the accuracy is to use geometries that can closely mimic the shape of the liquid droplet.

Results of component fraction from the approximate method

The ranges of the cubic box along the X, Y and Z directions were identified and shown in **Figure 36**. The exact number of C1 and C4 molecules in each phase are listed in **Table 5**.

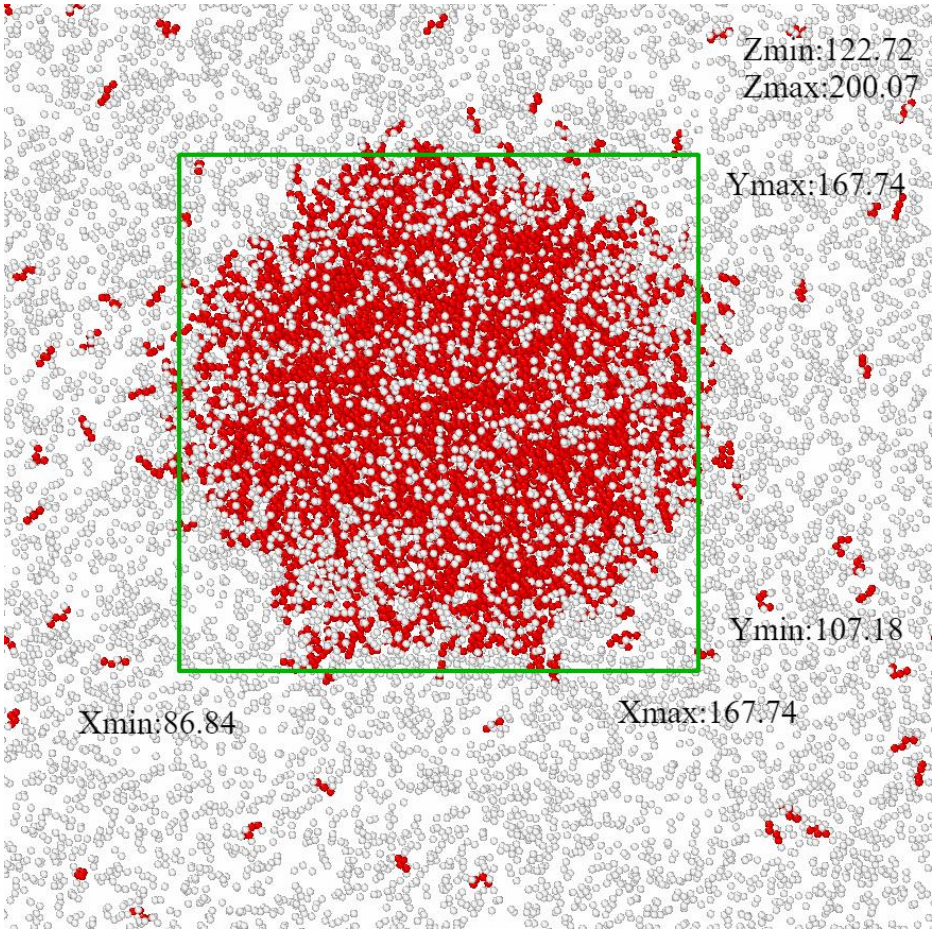

Figure 36: Coordinate values of the cubic region. All of the values were found from the XYZ file of the system (An output file from LAMMPS).

The results of this example are shown in **Table 5**:

Results	**C1 in Liquid**	**C4 in Liquid**	**C1 in Gas**	**C4 in Gas**
Number	**2512**	**1774**	**9488**	**344**
Fraction	**58.6%**	**41.4%**	**96.5%**	**3.5%**

Table 5: Number and fraction of C1 and C4 in the liquid and vapor phases.

In order to check the accuracy of results shown in **Table 5**, we adopted the vapor-liquid equilibrium flash calculation to determine the fraction of C1/C4 in each phase.

4.2.3 Vapor-Liquid Flash Calculation

Minimum Gibbs energy

Before the vapor-liquid equilibrium (VLE) flash calculation, it is necessary to determine whether or not the initial single-phase fluid will flash into a two-phase mixture under the known pressure and temperature. Whitson and Brulé (2000) concluded that the initial fluid prefers to minimize the Gibbs energy of the system. If the system could remain a lower Gibbs energy by a two-phase co-existence, the phase splitting from the initial vapor phase to a vapor-liquid phase mixture is a spontaneous process.

VLE method

The main theory of VLE is based on mass balance calculations. For the total mass balance:

$$F = V + L \tag{4.2.1}$$

At equilibrium, for the mass balance of each component in the liquid and vapor phases:

$$F \times Z_i = L \times X_i + V \times Y_i \tag{4.2.2}$$

The parameter C is defined as the vapor-phase fraction:

$$C = V / F \tag{4.2.3}$$

From the equations (4.2.1, 4.2.2, 4.2.3), the expression of component i in each phase-state is:

$$X_i = \frac{Zi}{1+C\times(K_i-1)} \; ; Y_i = \frac{K_i\times Zi}{1+C\times(K_i-1)} \tag{4.2.4}$$

Since the sum of all component fractions for each phase should be unity, we have:

$$\sum_{i=1} X_i = 1 \;\; ; \;\; \sum_{i=1} Y_i = 1 \tag{4.2.5}$$

$$\sum_{i=1} (X_i - Y_i) = 0 \tag{4.2.6}$$

Therefore, we can derive the Rachford-Rice function, which is the core equation for VLE flash calculation:

$$\mathrm{f}(C) = \sum_{i=1} \frac{(K_i - 1) \times Z_i}{1 + C \times (K_i - 1)} = 0 \tag{4.2.7}$$

K_i is defined as the equilibrium constant for each component. C is the only unknown parameter which can be calculated by numerical method - Newton-Raphson method. The VLE calculation is performed via the MATLAB code with the steps as shown in **Figure 37** by courtesy of Dr. Hamidreza Karami (University of Oklahoma):

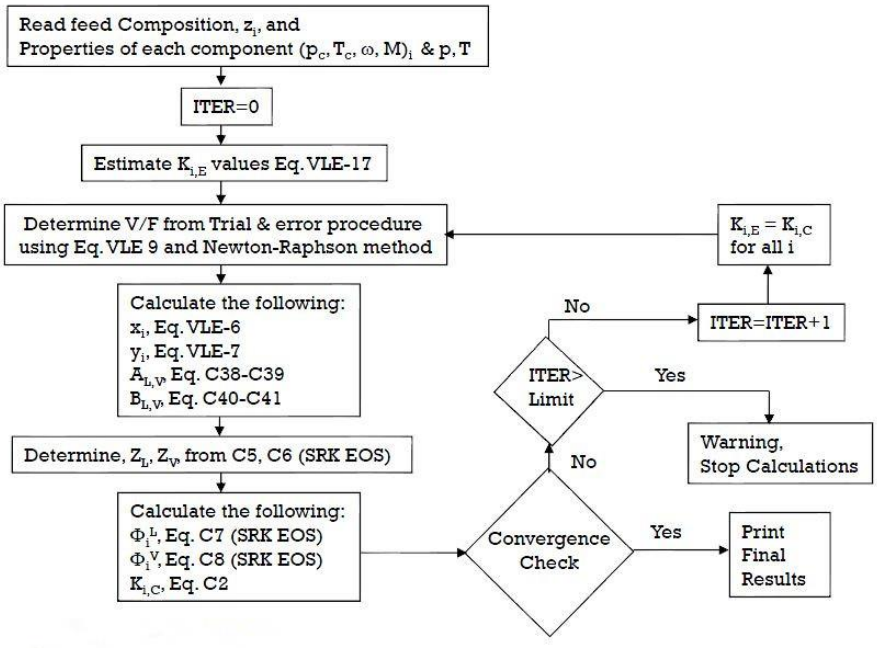

Figure 37: Loop of VLE process [Source: Class notes from Dr. Hamidreza Karami, The University of Oklahoma, 2017].

$K_{i,c}$ represents the equilibrium constant of component i:

$$K_{i,c} = \frac{yi\ (Gas\ mole\ fraction\ of\ component\ i)}{xi\ (Liquid\ mole\ fraction\ of\ component\ i)} \quad (4.2.8)$$

Last but not least, the choice of an equation of state (EoS) is critical for flash calculations. This is because EoS is used to calculate fugacity coefficients of each component in each phase, which directly affects the quality and accuracy of the equilibrium constant $K_{i,c}$. After having the value of $K_{i,c}$, the iteration as discussed in **Figure 37** will be carried out. In this part, Wilson's Correlation (4.2.9) was used to estimate the initial $K_{i,E}$ value.

$$K_{i,E} = \frac{Pci}{P} \times \exp\{5.37 \times (1 + wi) \times \left[1 - \frac{Tci}{T}\right]\} \quad (4.2.9)$$

There are several EoS models such as Redilich-Kwong EoS, Soave EoS, Peng-Robinson EoS, and SRK-EoS, etc. The SRK-EoS and PR-EoS were selected to apply in the VLE method. In the calculation process shown above, there are two important procedures: the first one is to find vapor phase fraction (C, V/F) by using Newton-Raphson method in the inside while-loop; the second one is about iteration process in outside while-loop. All the details and formulas of VLE flash calculation were attached in **Appendix B**.

The MATLAB code of VLE with SRK-EoS /PR-EoS was first developed and then was used to test its accuracy by comparing with an experimental case (Sage et al. 1950). The initial condition of the experiment is shown in **Table 6**.

Initial Condition	
Constant Temperature (°F)	160
Constant Pressure (psi)	1000
Initial Zi of C1	0.5301
Initial Zi of C4	0.1055
Initial Zi of C10	0.3644

Table 6: Initial condition of the experimental fluid.

Under the pressure and temperature condition, the initial liquid mixture of C1/C4/C10 will flash into a vapor-liquid co-existence system. The composition of each component in each phase from the VLE code and experimental data are shown below.

Results	SRK-EoS		Experimental data	
Components	Gas Fraction	Liquid Fraction	Gas Fraction	Liquid Fraction
CH4	0.9317	0.2807	0.963	0.242
N-C4H8	0.059	0.1344	0.036	0.152
C10H22	0.0093	0.5849	0.0021	0.606
Results	**PR-EoS**		**Experimental data**	
Components	Gas Fraction	Liquid Fraction	Gas Fraction	Liquid Fraction
CH4	0.9276	0.2764	0.963	0.242
N-C4H8	0.0614	0.1336	0.036	0.152
C10H22	0.011	0.5899	0.0021	0.606

Table 7: Components fraction in the liquid/gas phase from VLE code and experiment data (Sage et al. 1950).

By comparing with experimental data, the results of the VLE code are satisfactory, which validates the developed MATLAB code. And then the verified code was applied to calculate the component fractions of the C1/C4 system and compared the results with the MD simulation. **Table 8** shows the initial condition of the C1/C4 mixture and **Table 9** shows the results of C1/C4 fraction in each phase from both methods.

Initial Condition	
Temperature (K)	**200**
Pressure (Mpa)	**3.49**
Number of C1	**12000**
Number of C4	**2118**
Zi of C1	**85%**
Zi of C4	**15%**

Table 8: Initial condition of mixture C1/C4 fluid in MD example.

Results	**C1 in Liquid**	**C4 in Liquid**	**C1 in Gas**	**C4 in Gas**
VLE	**18.1%**	**81.9%**	**99.62%**	**0.38%**
MD	**38.6%**	**61.4%**	**96.5%**	**3.5%**

Table 9: C1/C4 fraction in the liquid/gas phase from the VLE method and MD simulation.

From the results in **Table 9**, it is clear that the difference between the two methods is significant. The reasons are: 1). The MD estimation was using one configuration of the simulation trajectory. There are hundreds of configurations along the MD trajectory, so the fraction shall be the average value. 2). The adopted cubic shape is a rough estimation.

A better approximation is needed to identify gas and liquid molecules. It is worth emphasizing that the method developed in chapter 4.2.2 is just a rough and simple method to gain some initial insight of the analysis.

4.3 Other Methods to Identify Gas and Liquid Molecules

To study a new subject, the first step is to start from its foundation. The final goal of chapter 4 is to determine the phase/component fraction of hydrocarbon fluid (multi-component system) under a confined condition by using MD simulation, therefore the first target is to study the phase-state of a single-component system in bulk-phase condition. If the study of a single-component system can be successfully achieved, then it will be extended to the multi-component system. In the following chapters, the pure methane/pure N-butane system was selected to represent the single-component system.

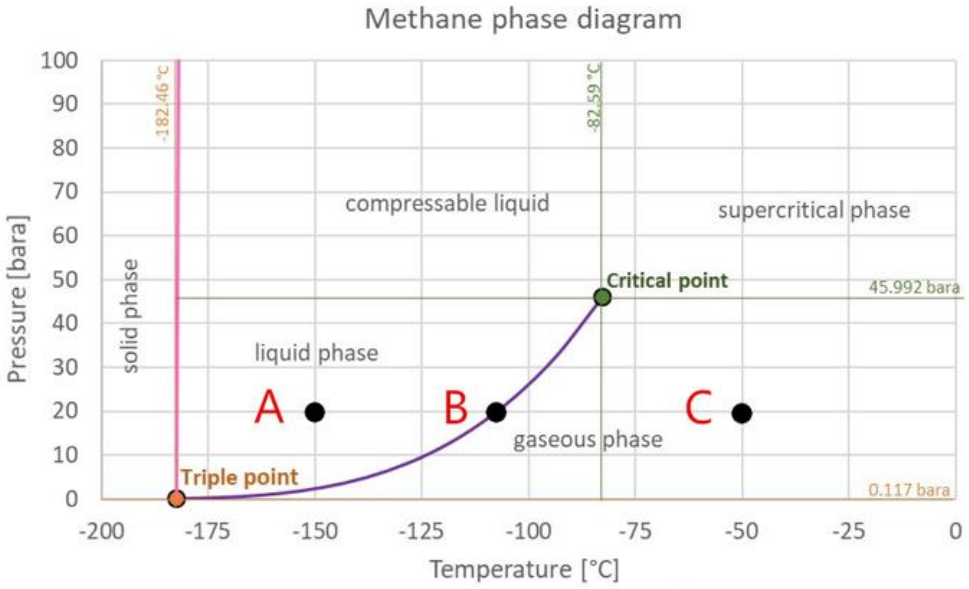

Figure 38: Phase diagram of pure methane
[Source: Modified from The Engineering ToolBox, 2008].

Figure 38 displays the phase diagram of pure methane. If the pressure and temperature of pure methane fluid were given in its single-phase region like point A or point C, it is easy to determine its phase-state by the phase diagram. But, how about the phase state in point B which is a coexistent state of liquid phase and gas phase (Two-phase state). In the two-phase state (point B), it is hard to determine the fraction of liquid methane and gas methane by using this phase diagram. In the following chapters, several methods with MD simulation to determine component fraction in two phase-state of a single-component system have been developed.

4.3.1 First Method – Molecule Distance

For a pure-C1 system or a pure-C4 system, the issue is what is the difference in essence between gas molecules and liquid molecules. Two liquid-C4 molecules and two gas-C4 molecules were picked from MD example and shown in **Figure 39**.

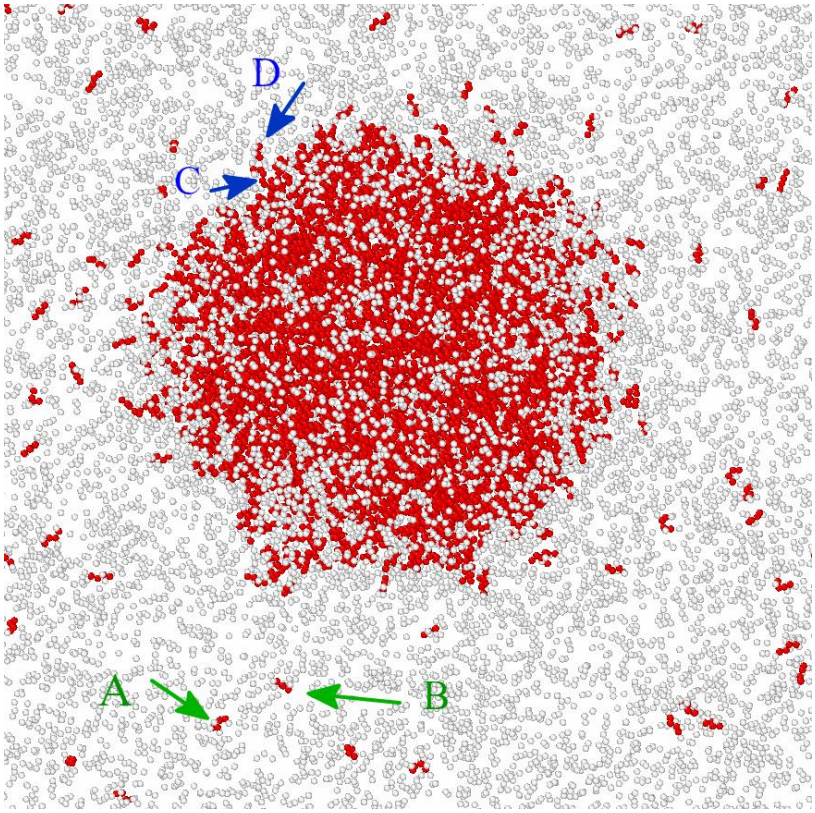

Figure 39: The distance between gas molecules A and B is much larger than the distance between liquid molecules C and D.

The distance between gas molecule A and B is several orders of magnitude larger than the distance between liquid molecule D and C, therefore the distance between molecules was used as judgment to identify phase-state in chapter 4.3.1. Next, for a pure methane system (or pure C4 system), the challenge is: under a specified pressure condition, what is a range of distance between two methane molecules that we can define these two methane molecules are in the gas phase, and what is a range of distance between two methane molecules that we can define they are in liquid phase.

If the maximum distance between liquid-methane molecules and the minimum distance between gas-methane molecules can be determined under a specified pressure condition, then it is possible to find the number of gas-methane molecules and liquid-

methane molecules in its two-phase state. The main idea is – under a specified pressure condition, If the distance between any two methane molecules is smaller than liquid maximum distance, then both of these two methane molecules can be defined as liquid-C1 molecules; similarly, if the distance between any two methane molecules is larger than minimum gas distance, then both of them can be defined as gas-C1 molecules. The minimum gas distance should be much larger than the maximum liquid distance like **Figure 39** shown.

To determine the max-distance between liquid-C1 molecules and min-distance between gas-C1 molecules under a specified pressure condition is essential for this method. Also, in this method, these two distances were assumed to be different with different pressure condition, that is why the pressure condition needs to be specified before using this method. The factor temperature can help us to determine these two distances after the pressure has been decided. The theory about how to define maximum liquid distance and minimum gas distance under a specified pressure is explained through an example shown below.

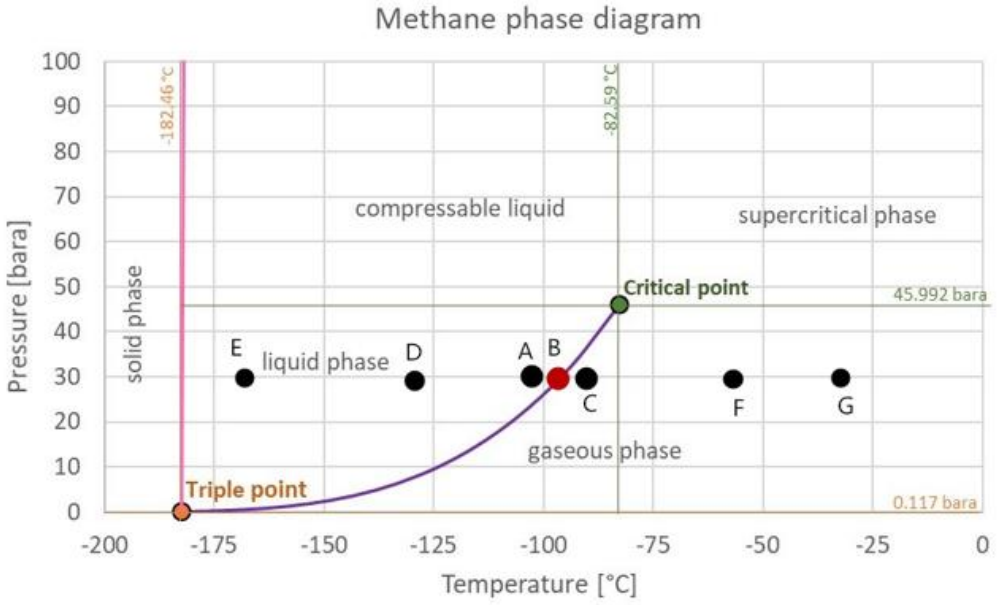

Figure 40: Critical liquid condition at point A; critical gas condition at point C; two-phase state at point B [Source: Modified from The Engineering ToolBox, 2008].

For instance, we want to determine the gas/liquid fraction of methane at its two-phase state under 30 bar which is point B shown in **Figure 40**. From this method, the maximum liquid distance can be calculated based on the coordinate file from MD simulation at point A and the minimum gas distance can be calculated based on the coordinate file from MD simulation at point C because the distance between molecules will decrease as temperature decrease, contrarily the distance between molecules will increase as temperature increase. Also, in chapter 4, such the point A and Point C are defined as the critical point of liquid-phase state and critical point of gas-phase state under a specified pressure condition.

How to determine the maximum liquid distance and minimum gas distance based on MD simulation at point A and C? Through some studies and investigation, the Radial distribution function (RDF) was thought as a helpful tool to solve this problem.

The definition of RDF from molecular dynamics simulation is (Oobatake et al. 1990):

$$g_{cc}(\mathrm{r}) = < \frac{1}{N} \sum_{i=1}^{N} [\frac{V \Delta n_{cc}(r)}{N 4 r^2 \Delta r}] > \quad (4.3.1)$$

The N means the number of molecules in the system with volume V. The $\Delta n_{cc}(r)$ means the number of molecules in the range from $r - \frac{\Delta r}{2}$ to $r + \frac{\Delta r}{2}$. The $g_{cc}(\mathrm{r})$ is the probability of finding molecules at a distance r from a reference molecule. The < > means an average calculation of all molecules in the system. From its definition, the RDF represents a general and typical property that every molecule has in the target system because it is an average result calculated from all molecules in the target system. In addition, RDF describes the density variation of atoms as a function of distance from a reference atom. For example, in **Figure 41**, RDF can be expressed by the density of atoms in the yellow region (at any distance r) over the average density of the whole system:

$$\mathrm{RDF} = \frac{Local\ density\ of\ atoms\ at\ any\ position\ r}{Overall\ density\ of\ atoms (bulk-phase\ density)} \quad (4.3.2)$$

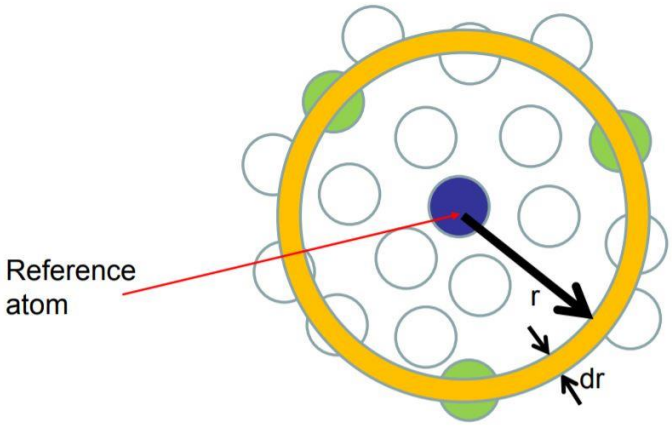

Figure 41: Radial distribution function
[Source: Wiketomica, 2008].

From its definition, the RDF can tell us at which location we can find the maximum number of atoms around the reference atom. In this method, the location of the largest local density in RDF was assumed to be different for gas-state and liquid-state of any hydrocarbon substance. The location r that has the largest RDF value was defined as a critical distance. In this method, the critical distance in RDF was also assumed to be different with different pressure and temperature. For example, in **Figure 40**, the critical distance of point A, B, C, D, E, F, G are different because their temperature is different.

Let me use an MD case to explain critical distance more clearly. **Figure 42**B displays the MD simulation of liquid C4 molecules under 30 bar/-57°C. **Figure 42**A displays its RDF graph. The red line was made by MATLAB code and black line was made by LAMMPS output (both of them matched well). The location of the first peak in RDF is equal to 5.1 Angstrom and therefore the critical distance (general distance) between two liquid-C4 molecules under 30 bar/-57°C is equal to 5.1 A.

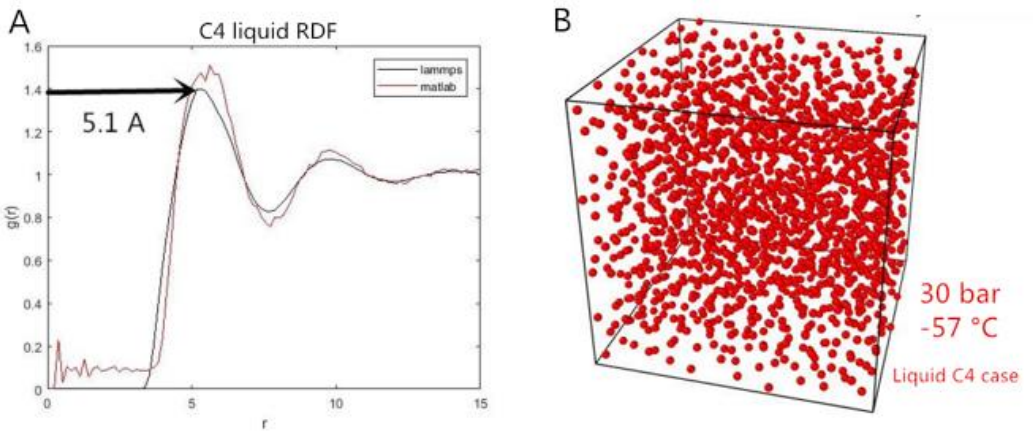

Figure 42: A) RDF of liquid C4 under 30 bar and -57 °C; B) MD model of liquid C4 under 30 bar and -57 °C.

Now go back to **Figure 40**, the maximum liquid distance is equal to the critical

distance of case at point A and the minimum gas distance is equal to the critical distance of case at point C. Furthermore, in this method, we thought the critical distance at point D is smaller than maximum liquid distance because lower temperature makes molecules getting closer to each other. Similarly, the critical distance of point G is larger than minimum gas distance because higher temperature makes molecules getting further to each other.

After the maximum liquid distance and minimum gas distance are determined under a specified pressure condition, then we can try to distinguish the fraction of gas-C1/liquid-C1 molecules in its two-phase state through this method.

4.3.2 A Case Study to Test the First Method

For the case in **Figure 40**, the MD simulation ran two cases. The first case was at point A which is the liquid phase of C1 under 30 bar and the second case was at point C which is the gas phase of C1 under 30 bar. The maximum liquid distance and minimum gas distance under 30 bar were determined through their RDF graph. At point A, the liquid C1 is approximately at 30 bar and -105 °C, which has a density of 0.0208 mol/cm^3. Also, at point C, the gas C1 is at 30 bar and -90 °C, which has a density of 0.0030 mol/cm^3. In MD simulation, these two cases simulated under NPT ensemble and all x-y-z periodic boundary (P-P-P). The two models are shown below (**Figure 43** and **Figure 44**)

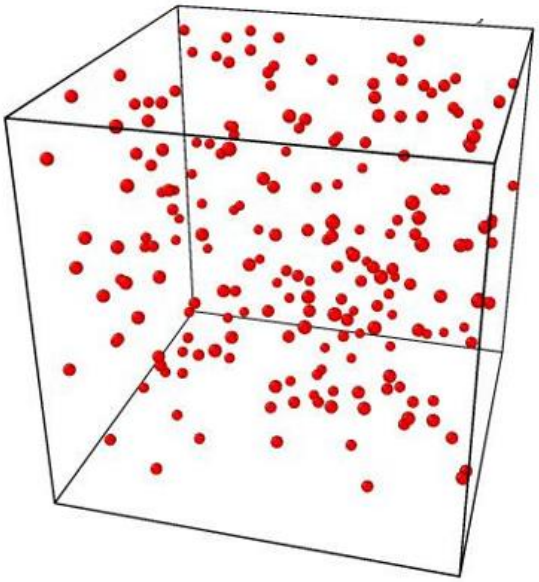

Figure 43: MD model of case C: gas-C1 system under 30 bar and -90 °C. The system density is 0.003 mol/cm^3.

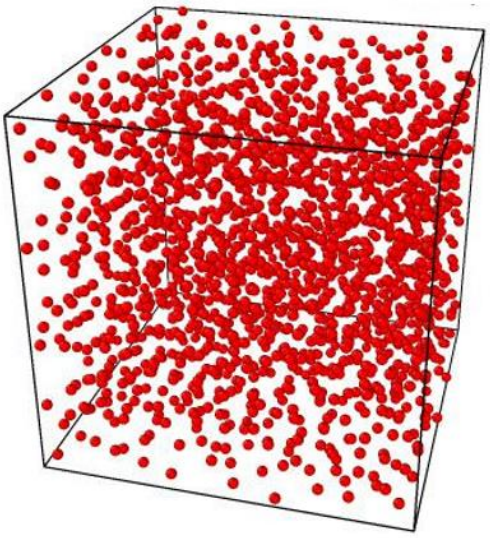

Figure 44: MD model of case A: liquid-C1 system under 30 bar and -105 °C. The system density is 0.0208 mol/cm^3.

After each system was in its equilibrium state, the radial distribution function of each case was calculated and compared in **Figure 45**.

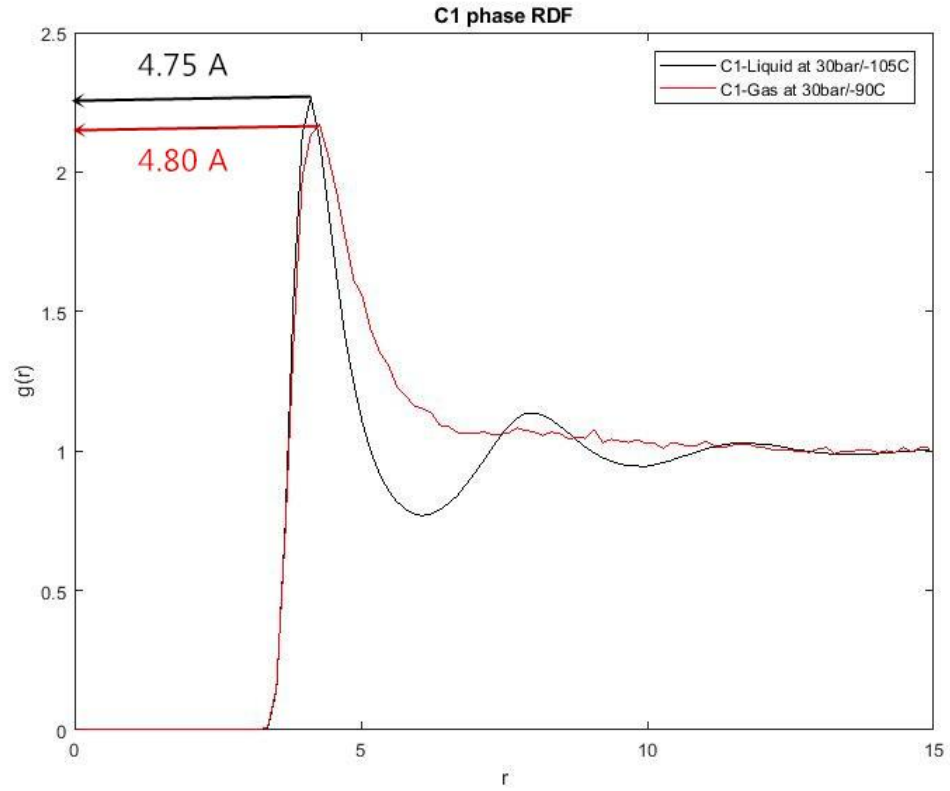

Figure 45: RDF of liquid-C1 and Gas-C1 at their critical condition (Point A, Point C).

From results, it is strange that there is no obvious difference between the max/min critical distance of liquid-C1 and gas-C1 under 30 bar, which is contrary to the initial assumption of this method. From their RDF, the maximum critical distance of liquid-C1 molecules is 4.75 angstrom and minimum critical distance of gas-C1 molecules is 4.80 angstrom. In the initial assumption, there should be several orders of magnitude difference between gas critical distance and liquid critical distance. And it is impossible to use these two values as a judgment in this method because they are almost same.

In order to understand why there is no obvious difference between the min-critical distance of gas-C1 and max-critical distance of liquid-C1, the gas-C1 molecules under different P/T conditions were simulated at first and their RDF graphs were shown in

Figure 46.

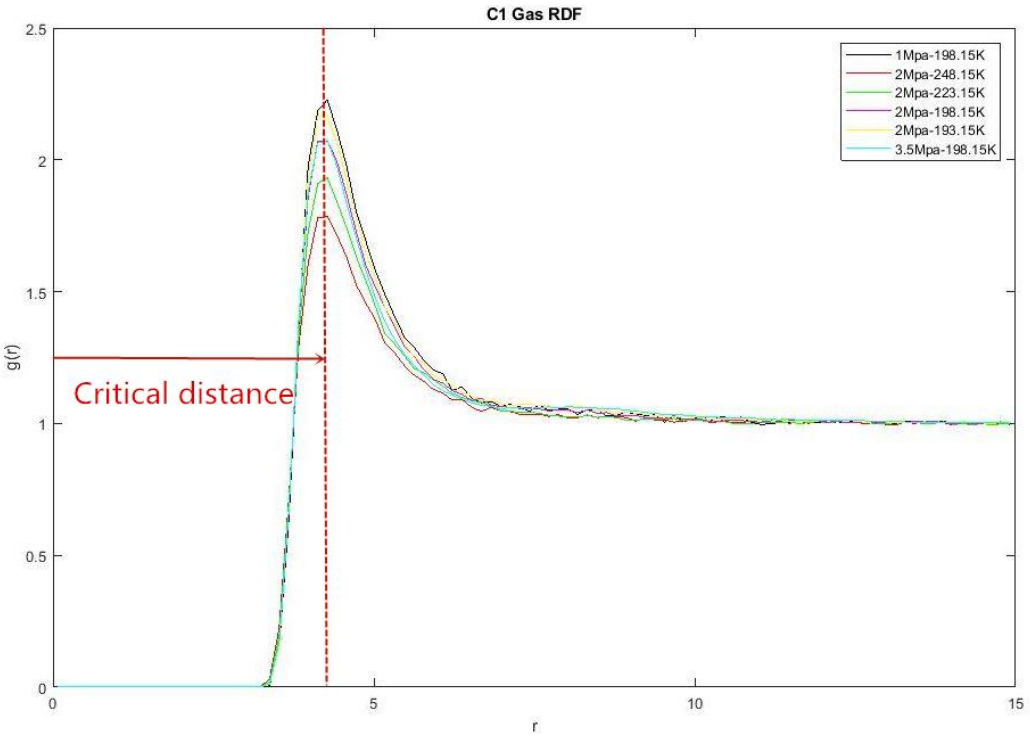

Figure 46: RDF of Gas-C1 under different conditions.

It is clear to see that the critical distance of each case is almost the same, no matter how the pressure or temperature change. Does this phenomenon just present in methane substance or still present in other substances? Also, how about the RDF graph of a substance in its liquid-phase state?

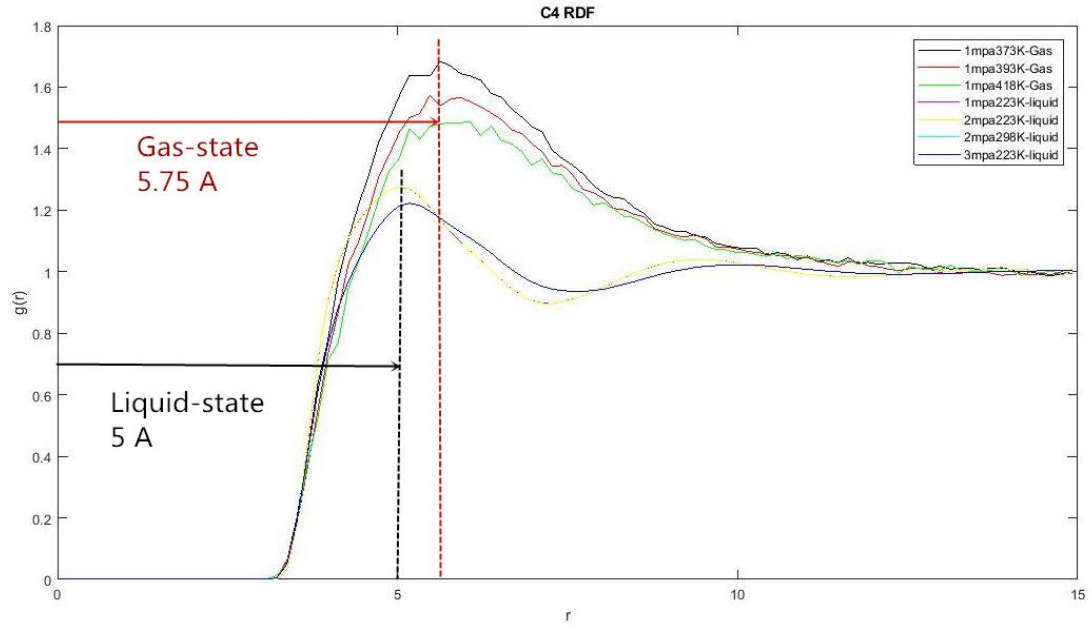

Figure 47: RDF of Liquid-C4 and Gas-C4 under different conditions.

The gas-state and liquid-state of C4 molecules under different P/T were simulated and their RDF graphs were shown in **Figure 47**. At first, the critical distance of all gas-state is about 5.75 angstroms and the critical distance of all liquid-state is about 5 angstroms. The difference between gas critical distance and liquid critical distance is still very small. At second, the location of the first peak is not affected by pressure and temperature no matter it is in a gas-phase state or liquid-phase state.

The result of pure C4 system is the same as pure C1 system. The phenomena about RDF discussed before are not just for a certain substance, but they are kinds of universal phenomena. In addition, **Figure 48** shows 3 phase-states RDF (gas/liquid/solid) of Argon and it is clear to see that critical distance is almost same no matter it is in gas-state, liquid-state or solid-state. In conclusion, the critical distance of a certain substance can be considered as a natural property of itself, and it is not affected by external factors, such as pressure, temperature.

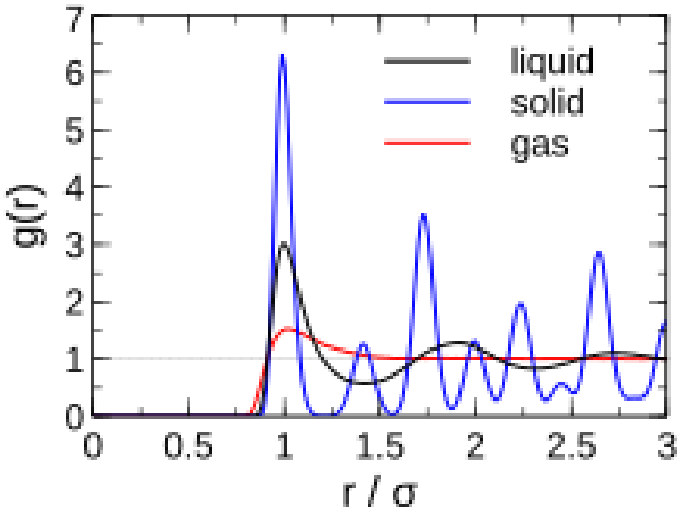

Figure 48: Argon RDF of its different phase-state
[Source: Wikimedia Commons, 2015].

The first MD method is not feasible to determine the C1 fraction in the two-phase state. In the next chapter, a new idea was introduced to continue the study.

4.3.3 Second Method – The Number of Peaks in RDF

Figure 49 displays the RDF of liquid-C1 molecules and RDF of gas-C1 molecules under 30 bar and it is obvious that there are two peaks in liquid-RDF and one peak in gas-RDF. Some research studies also indicated that for a certain substance, the RDF of its liquid-phase has two peaks and RDF of its gas-phase just has one peak (Zhou 2001). In this chapter, two methods based on the number of peaks were tried to determine whether a C1 molecule is liquid molecule or gas molecule in its two-phase state.

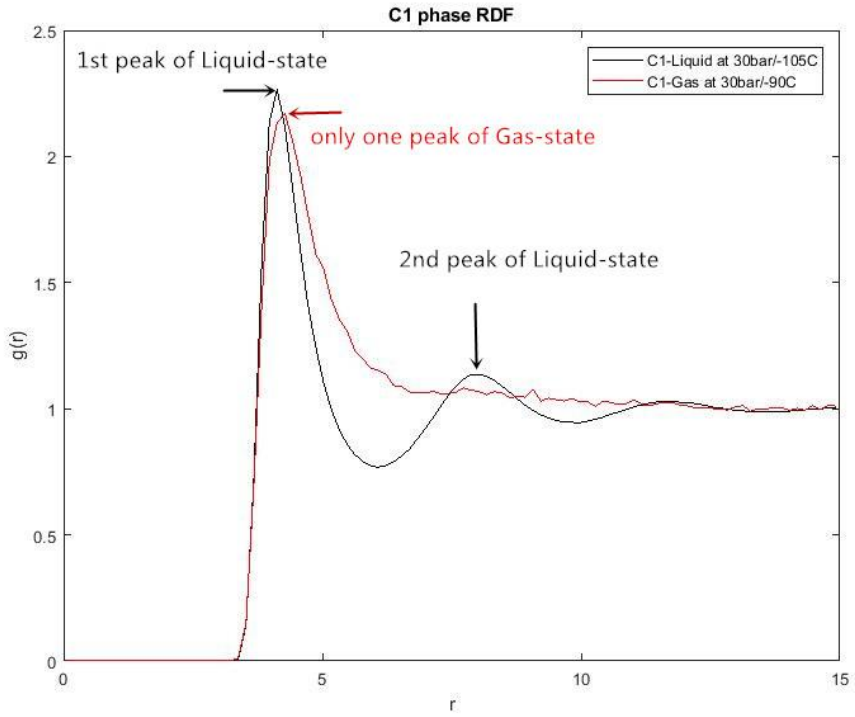

Figure 49: The number of Peaks in RDF of liquid-C1 and Gas-C1.

Two types of graphs were developed: 1. Number distribution graph of any single molecule; 2. RDF graph of any single molecule.

Number distribution graph

The Number distribution graph was simply defined as the number of molecules around any reference molecule versus its location r. Because the general RDF of a liquid-C1 system displays two peaks, from the definition of RDF, I thought that there are still two peaks in Number distribution graph of each liquid-C1 molecule. And the same rule for gas molecule, there is just one peak for every gas-C1 molecule in its Number distribution graph.

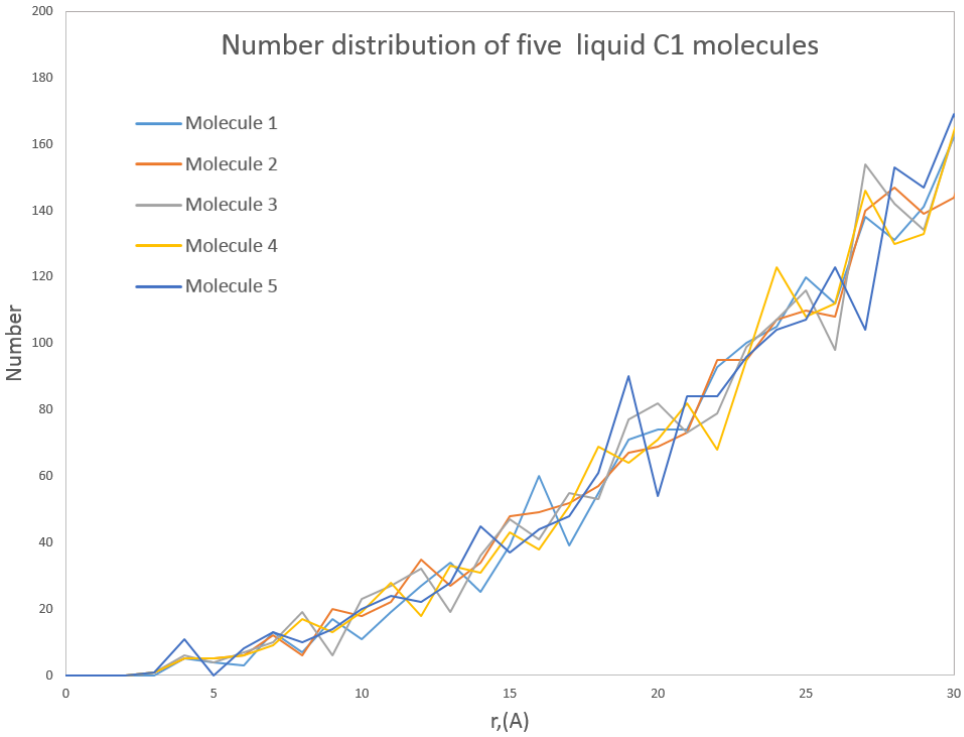

Figure 50: The number of molecules vs distance r of five liquid-C1 molecules under 30 bar and -105 °C.

Figure 50 displays the Number distribution versus location r of five liquid-C1 molecules. From this result, the number of molecules around the reference molecule increase with distance increase and there are no two peaks shown in this graph, which is totally different from the initial assumption. The confusing point is why the Number distribution increases continuously, but the RDF graph has a declining trend with distance r increase. As a further study of RDF, the problem of this idea was found. Let me use the example in **Figure 51** and **Figure 52** to explain my problem (this example is not related to the pure-C1 system discussed before, just for explanation).

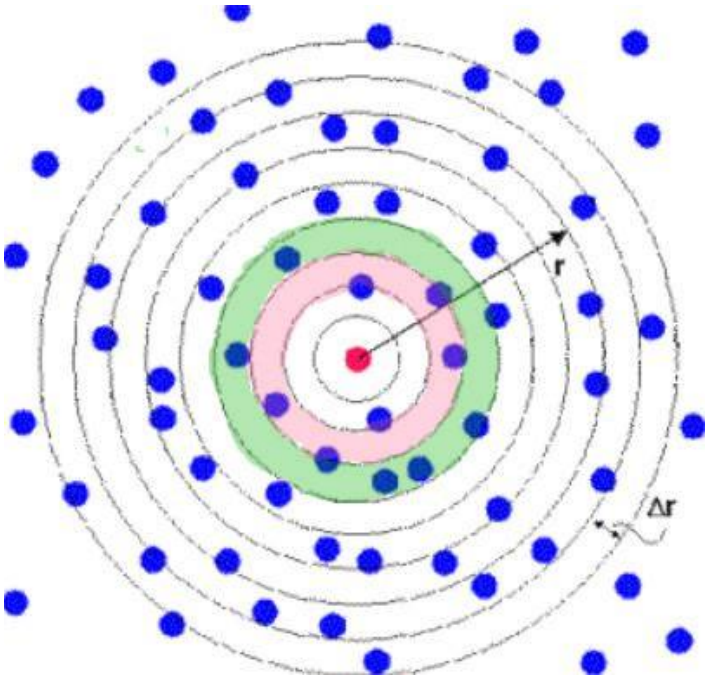

Figure 51: RDF plane of the example [Modified from Daresbury Laboratory, 2001].

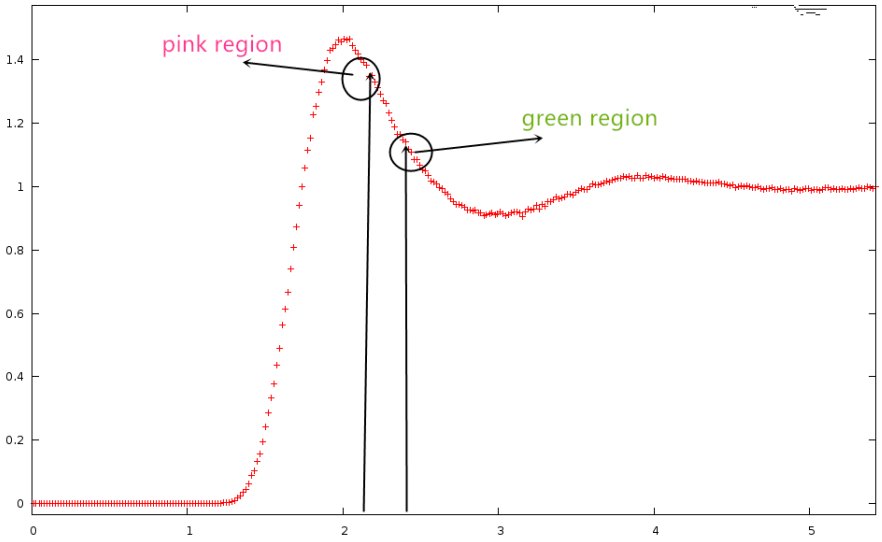

Figure 52: RDF of the example shown in Figure 51.

The RDF definition is:

$$rdf = \frac{Local\ density}{Bulk\ phase\ density} \tag{4.3.3}$$

$$Local\ density = \frac{number\ of\ molecules\ in\ local\ region\ (location\ r)}{volume\ of\ local\ region} \tag{4.3.4}$$

Figure 52 is the RDF of the example shown in **Figure 51**. The RDF value of the green

region is smaller than the RDF of the pink region, even though the number of molecules in the green region is larger than the number of molecules in the pink region. The reason for this confusion is that the volume of the green region is also larger than the volume of the pink region. Both numerator and denominator in Equation 4.3.4 increase together and therefore it causes the RDF of the green region smaller than RDF of the pink region. In fact, there is no relationship between the RDF graph and the Number distribution graph. From the work shown above, the Number distribution graph of a single molecule can't determine its phase state.

RDF of a single molecule

All the RDF graphs discussed before are a type of general graph of the whole system because they were plotted based on the average result of all molecules in the target system. The previous chapter concluded that the general RDF of liquid system and gas system are different (one peak for the pure gas system and two peaks for the pure liquid system), so the new idea is: how about the RDF of a single molecule in this system. For example, in a two-phase state, if the RDF graph of a single molecule has two peaks, then this molecule can be defined as a liquid molecule; if the RDF graph of a single molecule just has one peak, then this molecule can be defined as a gas molecule.

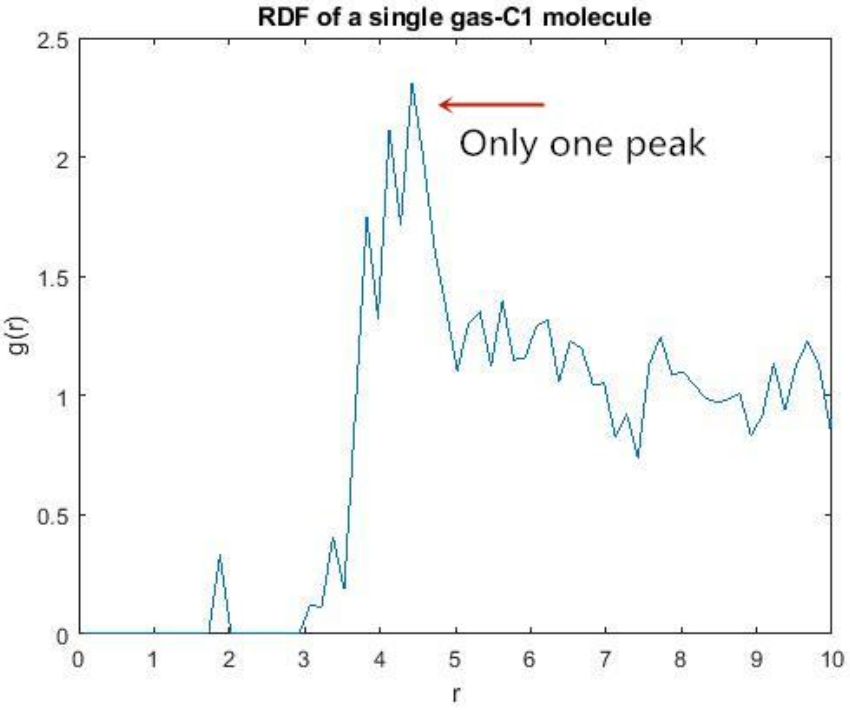

Figure 53: RDF of a single gas-C1 molecule under 30 bar and -75 °C.

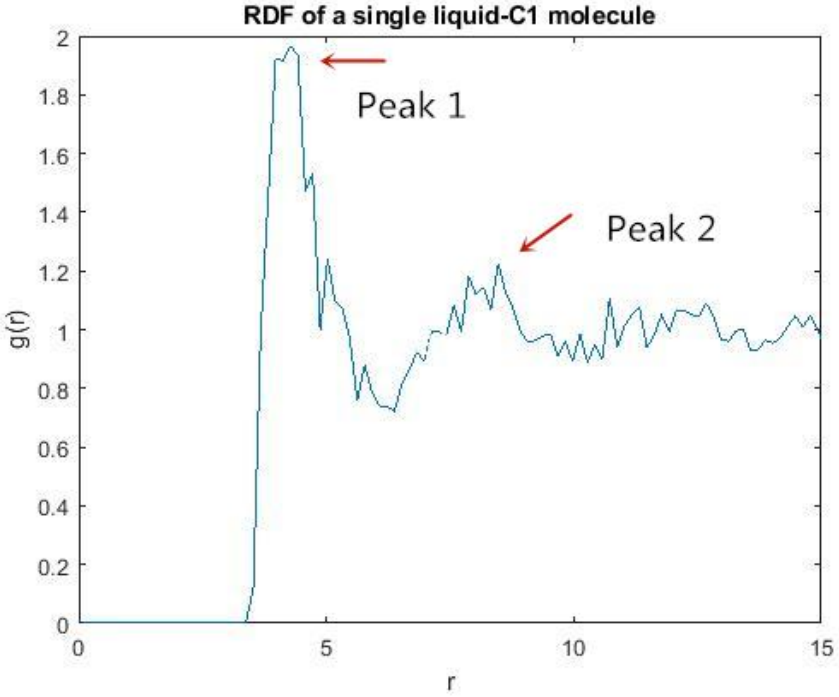

Figure 54: RDF of a single liquid-C1 molecule under 30 bar and -125 °C.

Figure 53 shows the RDF graph of a single gas-C1 molecule and **Figure 54** shows the RDF graph of a single liquid-C1 molecule. From their results, the features of the gas

molecule and liquid molecule can almost be distinguished, which are two peaks in RDF for the liquid molecule and one peak in RDF for the gas molecule. Now, the phase state of a single molecule can be successfully distinguished based on its RDF graph. But the new challenges are:1). It will take a lot of time to draw RDF graphs of all the molecules in a certain system. 2). How to determine the number of gas molecules/liquid molecules through a systematic way even if the RDF graphs of all those molecules are plotted (it is impossible to determine the phase of molecules one by one based on their RDF graphs).

In this chapter, the new methods about using the number of peaks are still unable to deal with the subject. And in the next chapter, a new method with the combination of critical distance and neighbor molecules has been developed.

4.3.4 Third Method – Neighbor Molecules

The chapter 4.3.2 concluded that there is no obvious difference between the critical distance of liquid-C1 molecules and gas-C1molecules under a specified pressure condition; also, the critical distance is a kind of natural property of a substance and it is not affected by external factors such as pressure, temperature. But there must be some differences between liquid molecules and gas molecules of a substance that haven't been found yet. After a further study of the radial distribution function, the differences were found.

For example, in a pure-C1 system, the difference between liquid-C1 RDF and gas-C1 RDF are: 1). the height of the first peak at the critical distance; 2). The number of neighbors around reference molecules before the first peak (the number of molecules

around the reference molecule in the circular region from radius = 0 to radius = critical distance).

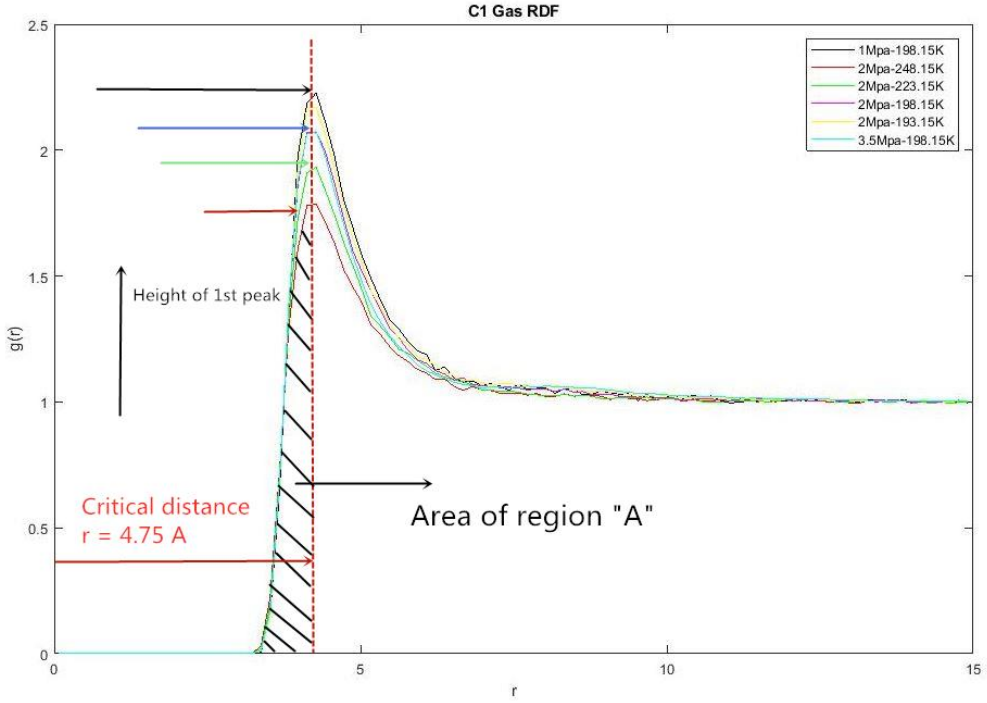

Figure 55: RDF of Gas-C1 under different conditions; Definition of region A.

In **Figure 55**, it shows the RDF graphs of gas-C1 molecules under different P/T conditions. The critical distance of all cases is almost the same and at same location r = 4.75 A, but height of the first peak (at location 4.75A) in each RDF is different. The area of the region from r = 0 to r = critical distance is different for each case because the height is different. From the definition of Radial distribution function, the larger area of region A means the larger number of molecules (or neighbors) in this region and vice versa. The definition of neighbors around the reference molecule can be explained by **Figure 56** shown below:

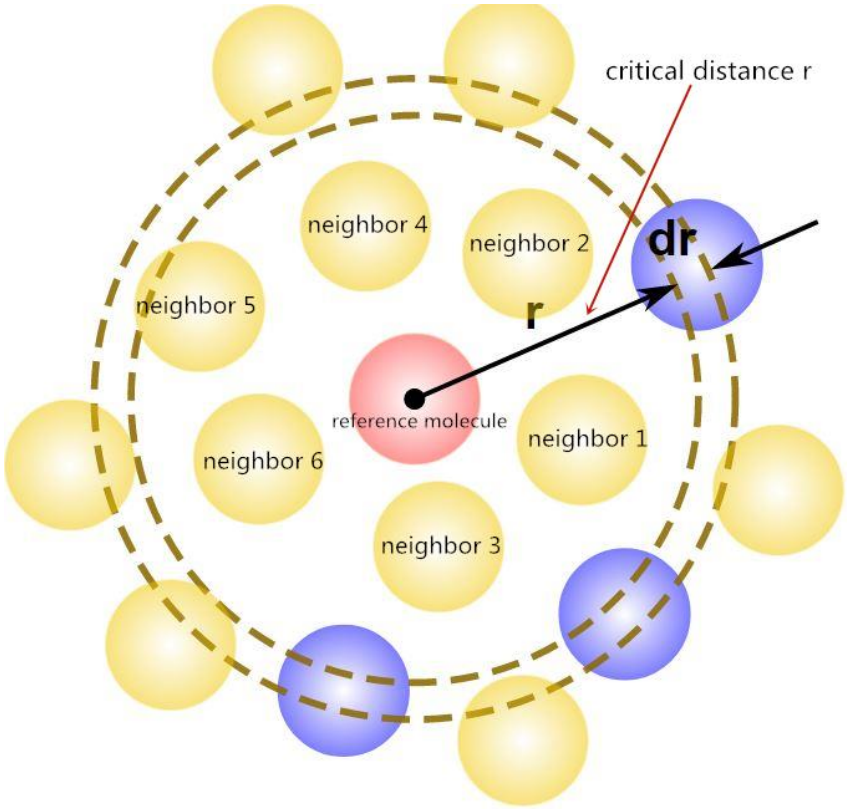

Figure 56: Definition of Neighbors around a reference molecule [Source: Modified from Wikimedia Commons, 2017].

For pure C1 system (pure C4 system is the same), the critical distance r has no big difference between its gas-state and liquid-state, but the number of neighbors around every molecule within region A are quite different. As discussed in chapter 4.3.2, there is a confusing question that is why there is no change in length of critical distance with the change of pressure or temperature. And now, the answer for that question is: for any molecule, the number of neighbors within its critical distance will change with P/T change but the length of critical distance will not change. Therefore, the number of neighbors around a liquid-C1 molecule within its critical distance is greater than the number of neighbors around a gas-C1 molecule within its critical distance.

In this method, firstly we need to define the critical number of any molecule in a

system:

Critical number = The number of neighbors around any reference molecule within region A

Region A is defined in **Figure 55**. The critical number of a molecule under different pressure and temperature is different.

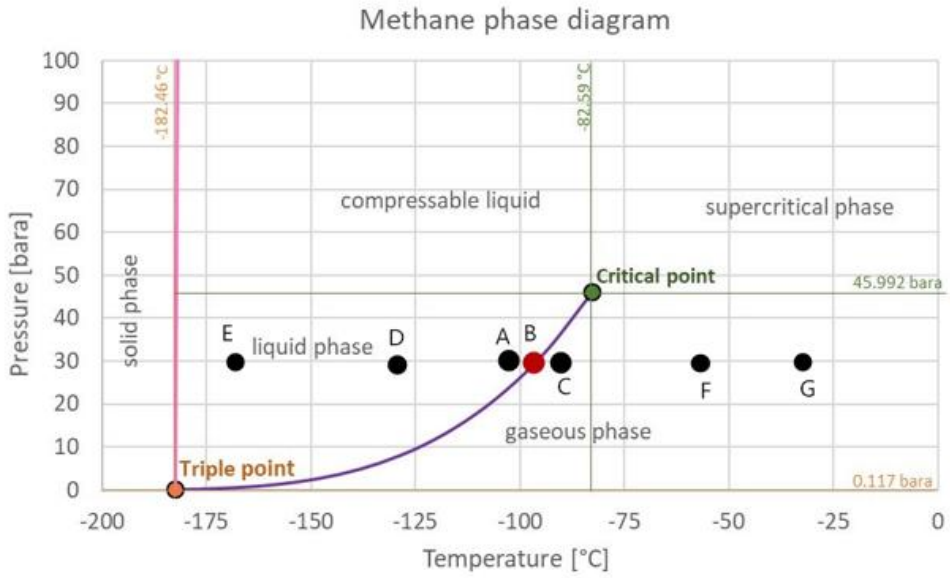

Figure 57: Critical liquid condition at point A; critical gas condition at point C; two-phase state at point B [Source: Modified from The Engineering ToolBox, 2008].

In **Figure 57**, the critical number of a C1 molecule at point E, D, A, B, C, F, G are different. Under a specified pressure condition, we thought that the critical number of a molecule will decrease as temperature increase and increase with temperature decrease. For example, the critical number of a liquid-C1 molecule at point E is larger than it at point D and the critical number of a gas-C1 molecule at point F is smaller than it at point C.

For a pure-C1 system (pure-C4 system is the same) under a specified pressure, the maximum critical number of gas-state and the minimum critical number of liquid-state (the maximum gas number and minimum liquid number) need to be found. After the

max/min-critical number of each phase-state was found, under a specified pressure condition, the molecule A will be defined as gas-molecule if its critical number is smaller than the maximum gas number; on the contrary, A will be defined as liquid-molecule if its critical number is larger than the minimum liquid number. The method of determining max/min critical number is the same as method of determining max/liquid critical distance, which is based on cases at two critical points (for example, in **Figure 57**, point A and point C were used for determining the max/min critical number of each phase-state under 30 bar). Please note, the maximum gas number and minimum liquid number are two average value and their definition are shown below:

Maximum gas number = < the number of neighbors around reference molecule i within region A> @ critical condition of gas-state

Minimum liquid number = < the number of neighbors around reference molecule i within region A> @ critical condition of Liquid-state

i=1,2,3,4,5…. N (Totally N molecules in the system)

The symbol < > means the average calculation of all molecules in the target system. In the assumption of this method, for a pure-substance system, its min-critical number of liquid-state (minimum liquid number) is far greater than its max-critical number of gas-state (maximum gas number).

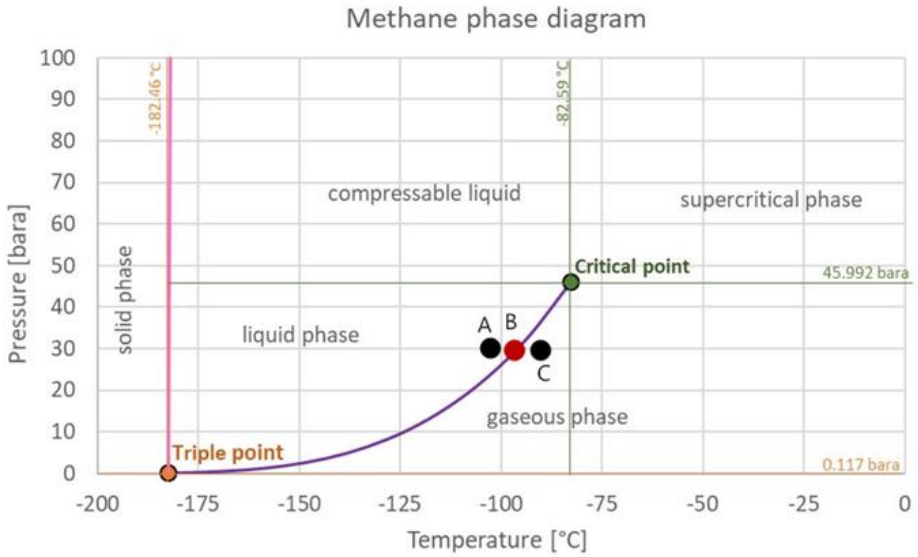

Figure 58: Critical liquid condition at point A; critical gas condition at point C; two-phase state at point B [Source: Modified from The Engineering ToolBox, 2008].

Let me use the example in **Figure 58** to show the procedures of this new method. In this pure-C1 system, the purpose is to find the number of liquid-C1 molecules and gas-C1 molecules at point B under 30 bar (two-phase state). At first, the point C was defined as critical point/critical condition for its pure gas-state; point A was defined as critical point/critical condition for its pure liquid-state. At second, the max/min critical distance of each phase-state can be determined based on point A and point C. After the critical distance determined, the region A and the max-gas number/min-liquid number can be determined through steps introduced before. Finally, for example, it is determined that the min-liquid number is 5 neighbors and max-gas number is 3 neighbors under 30 bar. If the critical number of a molecule in the two-phase state is 2 neighbors, then it is defined as a gas molecule; if the critical number of a molecule in the two-phase state is 7 neighbors, then it is defined as a liquid molecule. That's it!

4.3.5 A Case Study to Test the Third Method

A case study was used to test the new method. In **Figure 59**, under 30 bar, there are 7 different-temperature cases of pure methane system; three of them are in pure liquid-state and the other four are in pure gas-state.

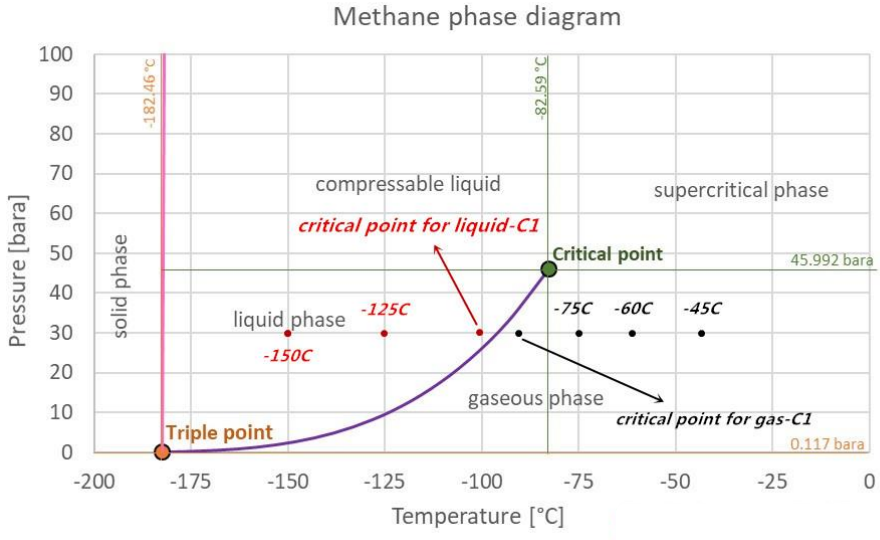

Figure 59: 7 cases were simulated under 30 bar. Left 3 cases: pure liquid-C1 system; Right 4 cases: pure gas-C1 system [Source: Modified from The Engineering ToolBox, 2008].

The min/max critical number (min-liquid number/max-gas number) can be used as a reference value to distinguish phase-state at other points. For example, on the left-hand side (liquid-state C1), the liquid critical point at temperature T = -100 °C is the reference point that can be used to distinguish phase-state of molecule at T = -125 °C or T = -150 °C, and the reason is that the critical number of every C1 molecule at T = -125 °C or T = -150 °C should be larger than min-liquid number because the temperature at the liquid critical point is higher than these two points. The same theory for gas-state on the right-hand side, the gas critical point at T = - 90 °C can be the reference point to distinguish phase-state of molecule at T = -75 °C, -60 °C and -45 °C, because the critical number of every C1 molecule at these three points should be smaller than max-gas

number.

The MD tool was still used to simulate these 7 cases. All the cases were simulated under the NPT ensemble (constant temperature, constant pressure, and a fixed number of molecules) and P-P-P boundary condition. With the given pressure and temperature, the number of molecules in a specified simulation-box was calculated through PR-EoS. Furthermore, because the size of this simulation is not big, the total simulation time was set to 20 ns which is enough for each case to get into its equilibrium-state finally. The MD details of each case are listed in **Table 10**.

Pure C1 system	Liquid-State C1			Gas-State C1			
Pressure(bar)	30			30			
Cases #	Case 1	Case 2	Case 3	Case 4	Case 5	Case 6	Case 7
Temperature(°C)	-150	-125	-100	-90	-75	-60	-45
Box size(nm^3)	4×4×4	4×4×4	5×5×5	5×5×5	8×8×8	8×8×8	8×8×8
The Number of C1 molecules	1098	964	1740	210	740	648	586
MD ensemble	NPT			NPT			

Table 10: The details of MD simulation for those 7 cases.

The RDF of each case was calculated after the simulation in equilibrium-state and is plotted below:

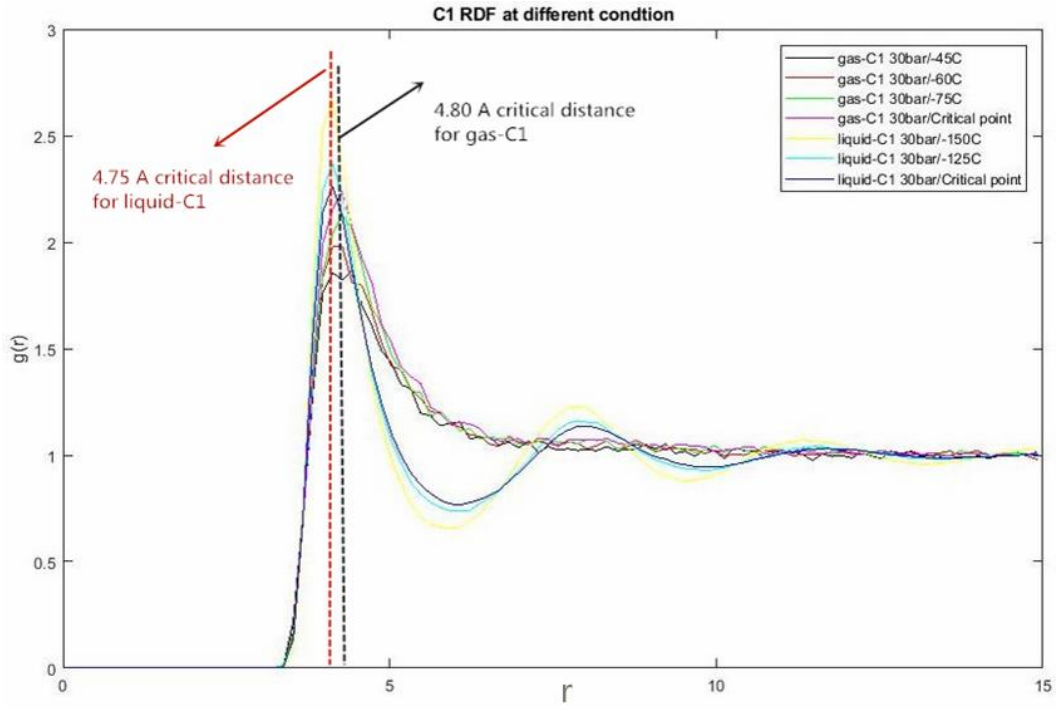

Figure 60: RDF of 7 C1-cases.

From the RDF results above, the critical distance of all liquid-C1 cases is about 4.75 angstrom and the critical distance of all gas-C1 cases is about 4.80 angstrom. The critical condition of the gas phase is case 3 and the critical condition of the liquid phase is case 4.

In MD simulation of case 3 (P = 30 bar, T = -100 °C), the number of neighbors around every liquid-C1 molecule within 4.75A can be calculated by using its coordinate file and the average value of all neighbor numbers is the min-liquid number. **Table 11** below shows a general outline about how to find min-liquid number directly.

The critical condition for liquid-state C1 system (T=-100°C, P=30 bar; case 3)	
Molecule ID	Number of neighbors within 4.75 A
1	5.2435
2	5.3131
3	5.2907
4	5.3221
⋮	⋮
1740	5.3064
Min-liquid number (average value of all 1740 molecules)	5.344

Table 11: Outline of calculating the min-liquid number of case 3.

One thing needs to be mentioned here is that the number of neighbors around each molecule is not an integer because this number is an average value of all timesteps. All of the procedures discussed before are just for one single timestep (every timestep has its own coordinate file of the system), so the final number of neighbors around each molecule should be an average value of all timesteps from the period of equilibrium-state.

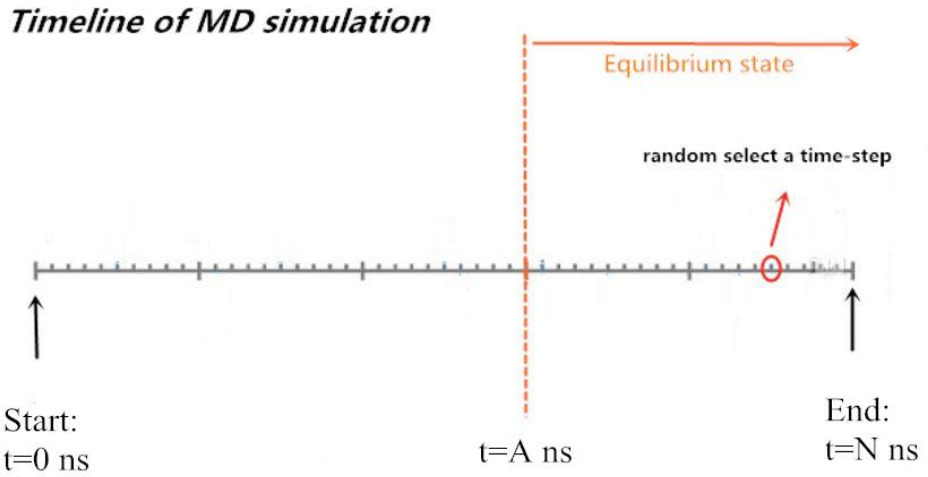

Figure 61: Timeline of Equilibrium MD simulation. The period of the equilibrium state is from A ns to N ns.

For example, in **Figure 61**, there are a lot of timesteps in the period of the equilibrium state, and the final answer should be an average value of all timesteps from A ns to N ns. The same method was used to find the max-gas number of case 4. The values of max/min-

critical number of gas/liquid-C1 molecules under 30 bar are shown in **Table 12**. After two critical numbers were known, the next step was to test the new method.

Min-liquid number of pure C1 system at P=30 bar	Max-gas number of pure C1 system at P=30 bar
5.344	0.7342

Table 12: results of max/min-critical number of pure C1 system under 30 bar.

Using the case 1 as an example, because molecules will approach each other with temperature decrease (more molecules go into region A as temperature decrease), therefore the critical number of every molecule in case 1 (P = 30 bar, T = -150°C) should be larger than the min-liquid number 5.344 and the final result should be 100% liquid molecules. For those cases in gas-state, the theory is the same as case 1. Every molecule in case 5, 6, 7 should have a critical number smaller than 0.7342 because higher temperature makes fewer molecules go into region A.

For the validation of these 7 cases, four of them should be 100% gas molecules (case 4-case7) and three of them should be 100% liquid molecules (case1-case3). The results of the test were listed in **Table 13** and **Table 14**. **Table 13** summarizes the results of liquid-state cases (case 1, case 2, case3) and **Table 14** summarizes the results of gas-state cases (case 4-case 7).

Validation of the 3rd method for the liquid-state C1 system				Percent of molecules calculated in liquid-state	Right percent of molecules in liquid-state
Pressure(bar)	Temperature(°C)	Critical distance (A)	Min-critical number		
30	-100 (Critical point)	4.75	5.344	60.13%	100%
30	-125	4.75		62.35%	100%
30	-150	4.75		88.97%	100%

Table 13: Test results of all liquid-state cases.

Validation of the 3rd method for the gas-state C1 system				Percent of molecules calculated in gas-state	Right percent of molecules in gas-state
Pressure(bar)	Temperature(°C)	Critical distance (A)	Max-critical number		
30	-90 (Critical point)	4.8	0.734	45.73%	100%
30	-75	4.8		49.01%	100%
30	-60	4.8		55.61%	100%
30	-45	4.8		62.94%	100%

Table 14: Test results of all gas-state cases.

For all liquid-state cases, the accuracy of result increases as temperature decreases. For all gas-state cases, the accuracy of result increases as temperature increase. The lower temperature makes molecules getting closer to each other which makes more molecules behave like a liquid molecule, and vice versa. For example, because of the lowest temperature, case 1 (T=-150°C) has the largest accuracy that is 88.97% of molecules can be distinguished as a liquid molecule. The case 7 has the largest accuracy in gas-state cases because its higher temperature makes more molecules behave like a gas molecule.

For both liquid-state cases and gas-state cases, there are quite difference between

results from the new method and theoretical results (none of these cases could have 100% accuracy), which means the only criteria about the number of neighbors is not enough to distinguish all the molecules in its right phase-state, so additional criteria need to be found. For example, we can either define an acceptable tolerance or an extra parameter to increase its accuracy. The additional tolerance or parameter hasn't been found in this thesis, but it can be the future work in this subject.

In chapter 4, three methods with MD simulation have been tried to study phase-state of single-component system. All the methods and ideas proposed in this chapter can't achieve the final goal, but they can be suggestion and experience for future work in this subject.

Chapter 5: Study of Supercritical CO_2 Fluid in Enhanced Oil Recovery

5.1 Background

In a conventional oil reservoir, about 5% ~ 20% of original oil in place (OOIP) can be produced by its primary recovery mechanism which is its natural reservoir energy (Stalkup et al. 1984). Because a large amount of oil still leaves in the reservoir after primary recovery, normally the secondary and tertiary recovery methods are applied to enhance oil recovery. Waterflooding is the most common secondary-recovery method. According to research studies, the combination of primary recovery and second recovery can produce 20% ~ 45% of OOIP (Stalkup et al. 1984; Tzimas et al. 2005), so it is no doubt that there is still a large amount of residual oil in place. Therefore, the tertiary recovery methods are designed to deplete the reservoir again. For tertiary-recovery methods, there are 3 basic categories:

1. Thermal flooding: steam flood, in-situ combustion
2. Chemical flooding: polymer flooding
3. Immiscible flooding: CO_2 injection method (CO_2 flooding).

CO_2 flooding has been proved that it can be used to enhance oil recovery successfully. The carbon dioxide (CO_2) is highly soluble in oil, therefore it can reduce oil viscosity,

cause oil swelling and decrease the surface tension of residual oil. But the disadvantages of tradition CO_2 flooding are obvious and inevitable (Verma 2015; Wang et al. 2017), for example:

1. The critical requirement of a CO_2 source location (it should be close to oil reservoir)
2. Transport cost of CO_2
3. Corrosion of transport-pipeline
4. Capital cost investment
5. Gas channeling problem

In order to avoid the limitations listed above of traditional CO_2 flooding, a new method called In-situ CO_2 generation is designed for tertiary oil recovery. The work in chapter 5 is mainly about studying in-situ CO_2 generation method via molecular dynamics simulation, especially for studying the behavior of CO_2 molecule in this flooding process.

5.2 Methodology of In-situ CO_2 Generation

The main theory of this new method is concluded below (Wang et al. 2017; Shiau et al. 2010):

1. The CO_2 is adsorbed in a chemical solvent to form carbamates or bicarbonates solution on the surface. This process can be expressed through the reversible chemical reaction:

   Carbamate solution:

$$2R_1R_2NH + CO_2 \leftrightarrow R_1R_2NH_2^+ + R_1R_2NCOO^- \quad (5.2.1)$$

Bicarbonate solution:

$$R_1R_2NH + H_2O + CO_2 \leftrightarrow R_1R_2NH_2^+ + HCO_3^- \quad (5.2.2)$$

2. The formed solution is injected into the reservoir. Because of the high reservoir temperature, the CO_2 will desorb from the solution. For example, Wang et al. (2017) used ammonium carbamate as the injected solution and its chemical reaction process in reservoir condition (Temperature above 95°C) is:

$$NH_2CO_2NH_4 \rightarrow 2NH_3 + CO_2 \quad (5.2.3)$$

From the chemical reaction shown in Equation 5.2.1 and 5.2.2, at high reservoir temperature, the carbamate solution will desorb CO_2 only, and Bicarbonate solution will generate CO_2 and water at the same time. Therefore, the behavior of CO_2 fluid in in-situ CO_2 generation process can be represented by a mixture system of water/oil/CO_2 from the molecular level.

The behavior of CO_2 is directly related to recovery efficiency. In detail, the self-diffusion of CO_2 and partition coefficient of CO_2 are two important elements that can significantly affect the recovery efficiency. The high-diffusivity of CO_2 means the high velocity of CO_2 which makes CO_2 penetrate the residual-oil zone very fast – in other words, high-diffusivity of CO_2 means that CO_2 fluid will be in breakthrough early, which

will decrease the recovery efficiency. In addition, the partition coefficient of CO_2 in oil and aqueous solution (water) can reveal the solubility of CO_2 in the oil phase and water phase. The larger solubility of CO_2 in oil phase makes higher recovery efficiency (Wang et al. 2017) because the viscosity of residual oil will decrease as more CO_2 dissolves in it. In the following chapter, the MD simulation was used to investigate the self-diffusion and partition coefficient of CO_2 in a water/oil/CO_2 system.

5.3 MD Simulation of Water/Oil/CO_2 Mixture

Part 1: Structure of the model

The simulation model is a mixture of water/oil/CO_2. The oil was simply represented by Octane molecule and the TraPPE-UA forced field was applied on octane molecules. The water was represented by H_2O molecule and the TIP3P force field was applied on H_2O molecules (TIP3P is a common force field designed for the water-related system). Lastly, the carbon dioxide was represented by the CO_2 molecule and classical EPM2 force field was applied on CO_2 molecules. Furthermore, the octane molecule was set as United-atom style (UA style); both H_2O and CO_2 molecule were set as All-atom style (AA style). The models of 3 components in MD simulation are shown in **Figure 62**, and the model of the whole system is shown in **Figure 63**.

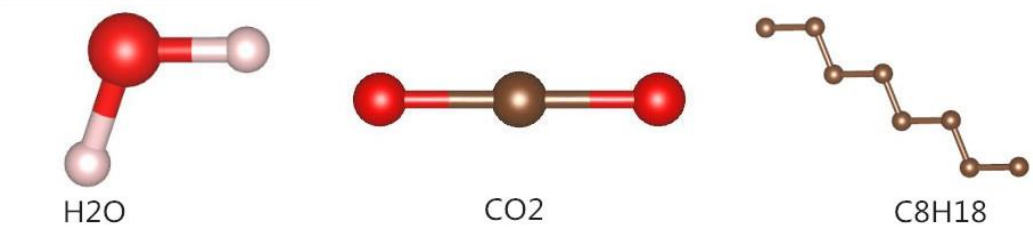

Figure 62: MD model of each component: H_2O (AA style), CO_2 (AA style), C8H18 (UA style).

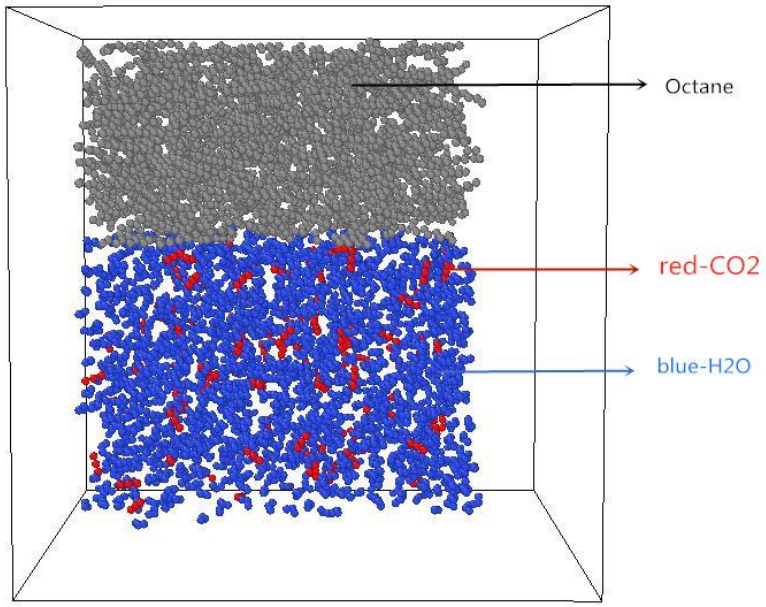

Figure 63: MD model of the water/oil/CO_2 system: 100 CO_2 molecules, 700 C8 molecules, and 1400 H_2O molecules.

The parameters of the EPM2 force field for CO_2 and TIP3P force field for H_2O are shown in **Tables** below:

EPM2 Force Field for CO_2: Bonded part		
	$\frac{k_b}{kcal}(mol^{-1}A^{-2})$	r_0/A
Bond-stretch Parameters	1283.4	1.149
	$\frac{k_b}{kcal}(mol^{-1}rad^{-2})$	θ_0/deg
Angle-bend Parameters	147.71	180

Table 15: EPM2 Force Field parameters of CO_2, Part I.

EPM2 Force Field for CO_2: Non-bonded part			
atom	q/e	σ/A	$\frac{\varepsilon}{kcal}mol^{-1}$
-C-	0.6512	2.757	0.056
O-	-0.3256	3.033	0.159

Table 16: EPM2 Force Field parameters of CO_2, Part II.

TIP3P Force Field for H_2O: Bonded part		
	$\frac{k_b}{kcal}(mol^{-1}A^{-2})$	r_0/A
Bond-stretch Parameters	450	1.993
	$\frac{k_b}{kcal}(mol^{-1}rad^{-2})$	θ_0/deg
Angle-bend Parameters	55	104.52

Table 17: TIP3P Force Field parameters of H_2O, Part I.

TIP3P Force Field for H_2O: Non-bonded part			
atom	q/e	σ/A	$\frac{\varepsilon}{kcal} mol^{-1}$
-O-	-0.834	3.53	0.1521
H-	0.417	0.45	0.046

Table 18: TIP3P Force Field parameters of H_2O, Part II.

Part 2: simulation details

The periodical boundary condition was applied in all 3 directions of the mixture system (P-P-P). The CO_2 fluid behaves like supercritical fluid under reservoir condition (Nakagawa et al. 2013; Shi et al. 2011; Zekri et al. 2006). Therefore, in order to keep CO_2 molecules as supercritical fluid in simulation, the NPT ensemble was selected.

For those factors that affect diffusivity and partition coefficient of CO_2, the pressure and temperature are two of them that have been investigated in this chapter. To study the effect of pressure, 5 cases with different pressure (1200 psi, 1450 psi, 2900 psi, 4400 psi, and 5800 psi) were simulated under the same temperature 200 °F. To study the effect of temperature, 5 cases with different temperature (212 °F, 302 °F, 392 °F, 482 °F, and 572 °F) were simulated under the same pressure 2900 psi. In addition, the CO_2 molecules were kept as supercritical fluid in all 10 cases. There is a total of 100 CO_2 molecules, 700 octanes (C8H18), and 1400 H_2O molecules in MD simulation for every case. Because the system of each case was required to achieve its equilibrium state, the total simulation time was set as 100 ns for all cases, which is enough for the system to get in its

equilibrium state.

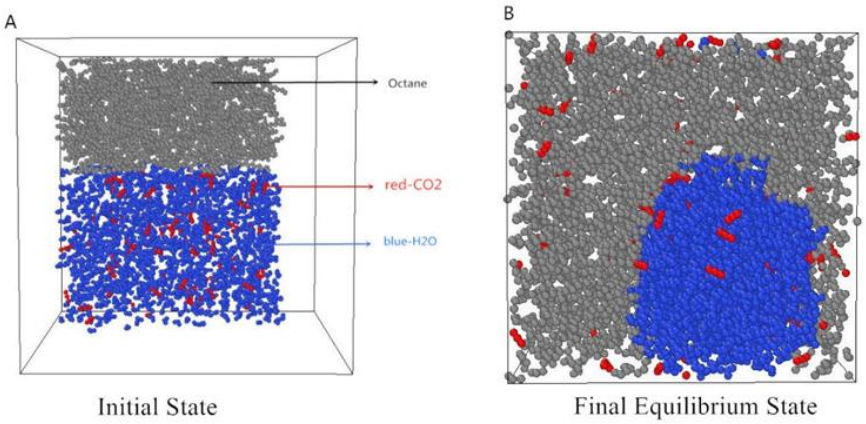

Figure 64: States of MD simulation for water/oil/CO_2 system at 200 °F and 2900 psi; 77A: t = 0 ns, 77B: t = 89 ns.

The initial set of simulation is shown in **Figure 64A**, and **Figure 64B** shows the equilibrium-state of the system at 89 ns (under 200 °F and 2900 psi). From the result of its final equilibrium-state, the construction of water/oil/CO_2 model was considered to be reasonable, because: (1). The water and oil phases should separate into two parts since they are immiscible to each other (like **Figure 64B** shown). (2). The CO_2 molecules should dissolve in both water and oil phase (like **Figure 64B** shown) because it is a truth that CO_2 is soluble in both oil and water.

5.4 Self-diffusion of CO_2 Molecule

The self-diffusion of CO_2 can reveal how fast the CO_2 will be breakthrough in the flooding process and it is directly related to the recovery efficiency. In this chapter, the effects of pressure and temperature on the self-diffusion of CO_2 were investigated.

Normally, the coefficient of diffusion (symbol *D*) represents the physical quantity of diffusion. In MD simulation, the LAMMPS tool provides us a common method to calculate the self-diffusion coefficient, which is called the Mean Square Displacement (MSD) method.

For 1D system, the average MSD value of all molecules in a group at time t can be expressed as:

$$\mathrm{MSD} = < |\mathrm{x(t)} - \mathrm{x(0)}|^2 > \tag{5.4.1}$$

x(t) means the location of any molecule at time t and < > means the average calculation of all molecules in a group. Through the combination of MSD concept and Einstein Equation, the self-diffusion coefficient of a 3D system can be derived as:

$$D_{self} = \lim_{t\to\infty} \frac{1}{6t} [\frac{1}{N} \sum_{N}^{i=1} |\mathrm{X(t)} - \mathrm{X(0)}|_i^{\ 2} + |\mathrm{Y(t)} - \mathrm{Y(0)}|_i^{\ 2} + |\mathrm{Z(t)} - \mathrm{Z(0)}|_i^{\ 2}] \tag{5.4.2}$$

With a combination of Equation (5.4.1) and (5.4.2), the self-diffusion coefficient can also be expressed as:

$$D_{self} = \lim_{t\to\infty} \frac{1}{6t} < MSD >_t \tag{5.4.3}$$

Finally, the equation above can be directly expressed as:

$$< MSD >_t = 6 \times \mathrm{t} \times D_{self} \tag{5.4.4}$$

From its final Equation (5.4.4), it is clear to see that there is a linear-function relationship between MSD and time t, and D_{self} is $\frac{1}{6} \times$ (gradient of this linear function), like **Figure 65** shown below.

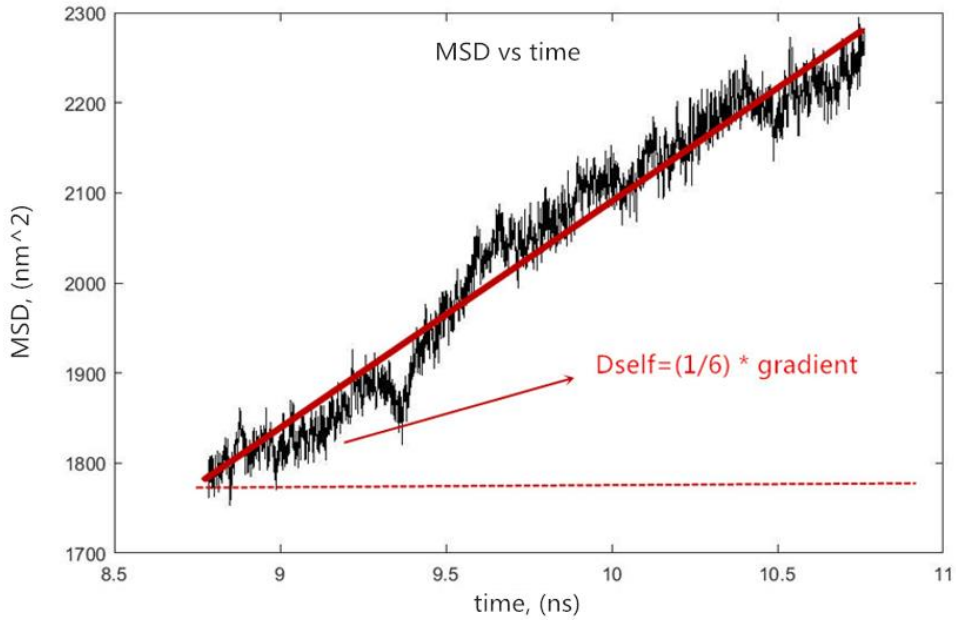

Figure 65: MSD concept.

Because the relationship between MSD and time t can be given from LAMMPS tool, it is not hard for us to calculate the self-diffusion coefficient of CO_2.

5.4.1 Results and Discussion

Figure 66 shows the Pressure vs CO_2 Dself and **Figure 67**shows the Temperature vs CO_2 Dself.

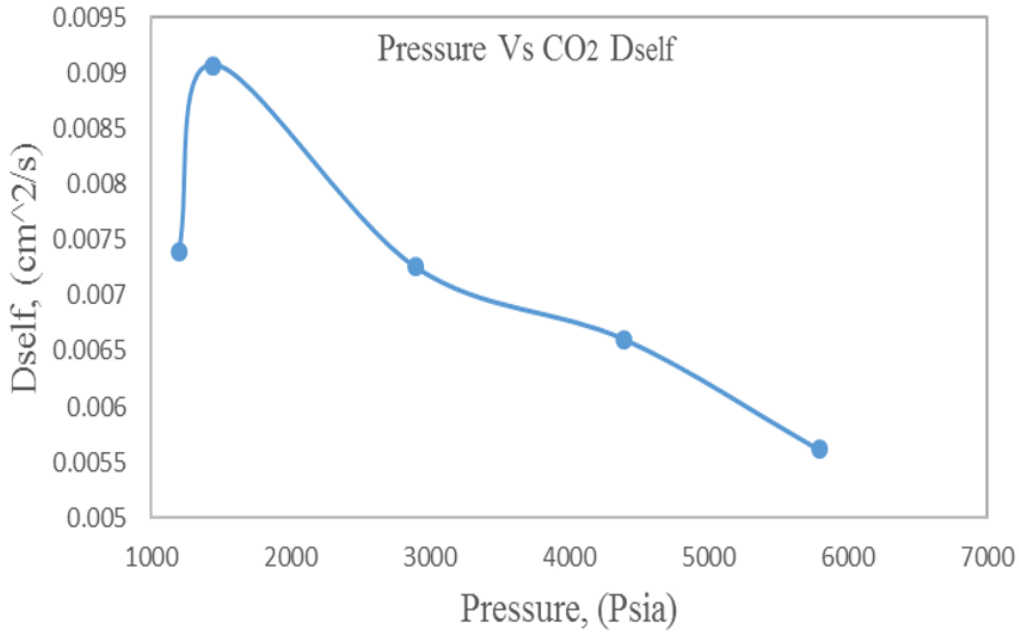

Figure 66: Different pressure Vs CO_2 Dself.

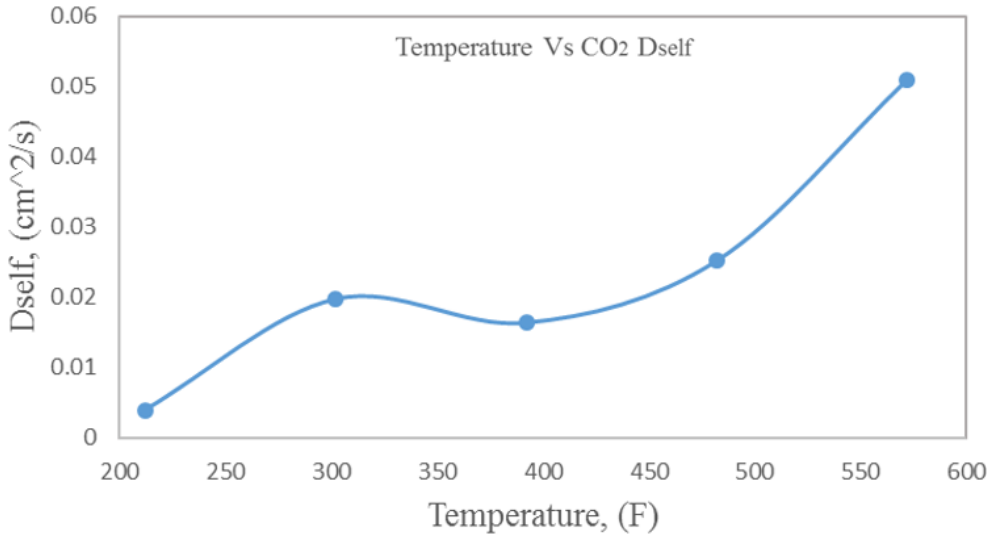

Figure 67: Different temperature Vs CO_2 Dself.

In general, as the pressure increases, the self-diffusion coefficient of CO_2 decreases; on the opposite, as the temperature increase, its self-diffusion coefficient increases. Normally, in the process of CO_2-related flooding, the engineers do not prefer a high self-diffusion of CO_2. Therefore, the CO_2-related flooding methods such as immiscible CO_2

flooding, in-situ CO_2 generation method, are best applied in the high-pressure reservoir or low-temperature reservoir.

5.5 Partition Coefficient of CO_2 Molecule

5.5.1 Concept of Partition Coefficient

The partition coefficient of CO_2 in water and oil is an important factor to study water/oil/CO_2 system because it tells us which liquid phase the CO_2 prefer to stay in (oil or water). The partition coefficient of CO_2 in water and oil is defined as:

$$K_{CO_2} = \frac{concentration\ of\ CO_2\ in\ oil}{concentration\ of\ CO_2\ in\ water} \tag{5.5.1}$$

Additionally, one thing that I want to emphasize here is that the partition coefficient K should be calculated under equilibrium-state of the target system. From the definition of K in Equation (5.5.1), it can also tell us the comparison of CO_2 solubility in oil and water. For example, if K_{CO_2} is larger than 1, it means the solubility of CO_2 in oil is larger than the solubility of CO_2 in water, and vice versa. The higher solubility of CO_2 in oil enhances the recovery efficiency of flooding since dissolved CO_2 can cause oil-swelling and reduction of oil viscosity (Wang et al. 2017). Until now, the research studies about determining the partition coefficient of CO_2 in water and oil under reservoir condition are very inadequate, especially by using Molecular dynamics simulation.

5.5.2 A Constructive Idea for Determining K_{CO_2}

As the chapter-title saying, only a constructive idea was proposed to determine the partition coefficient of CO_2 because it is not a 100% correct and well-done method. This idea is mainly based on using coordinate/trajectory file of the system.

LAMMPS tool provides the x-y-z file (coordinate file) of all molecules in the system, so the location of every molecule in the system is known. At any time, it is possible to find the number of CO_2 molecules in the water zone and oil zone according to its coordinate file, like **Figure 68** and **Figure 69** shown below.

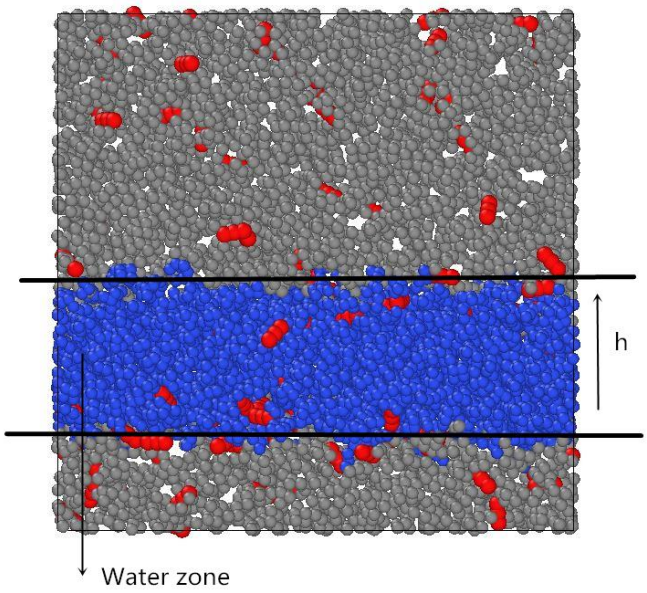

Figure 68: CO_2 molecules dissolved in the water phase and oil phase under 200 F and 4400 psi at 90 ns, in 2D.

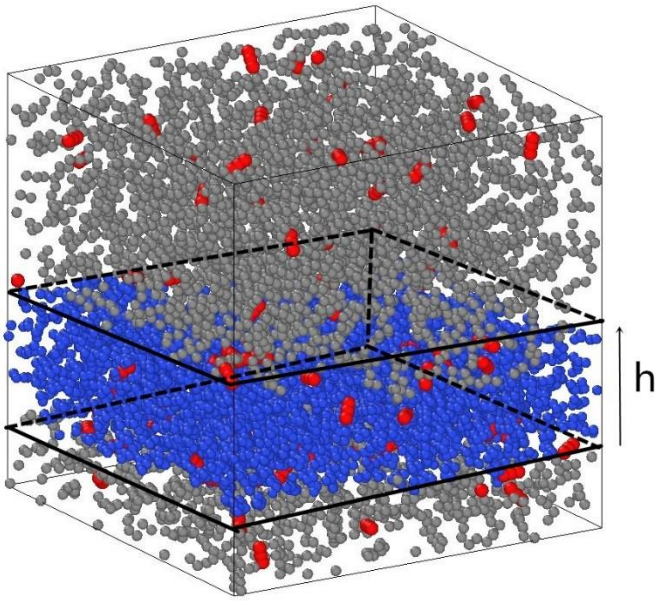

Figure 69: CO_2 molecules dissolved in the water phase and oil phase under 200 F and 4400 psi at 90 ns, in 3D.

Figure 68 and **Figure 69** display the equilibrium-state of the system at 90 ns under 200 F and 4400 psi. At this time, the number of CO_2 molecules in each zone was found below:

1. CO_2 in the water zone: 19
2. CO_2 in the oil zone: 81

Then the concentration of CO_2 in the water zone and oil zone:

3. The concentration of CO_2 in water: 0.0332 g/cm^3
4. The concentration of CO_2 in oil: 0.0446 g/cm^3

Finally, the partition coefficient of CO_2 at time = 90 ns is:

5. K_{CO_2} = 1.34

The K value calculated above just represents the partition coefficient of CO_2 at time = 90 ns but it can't represent the true partition coefficient of CO_2 in this system.

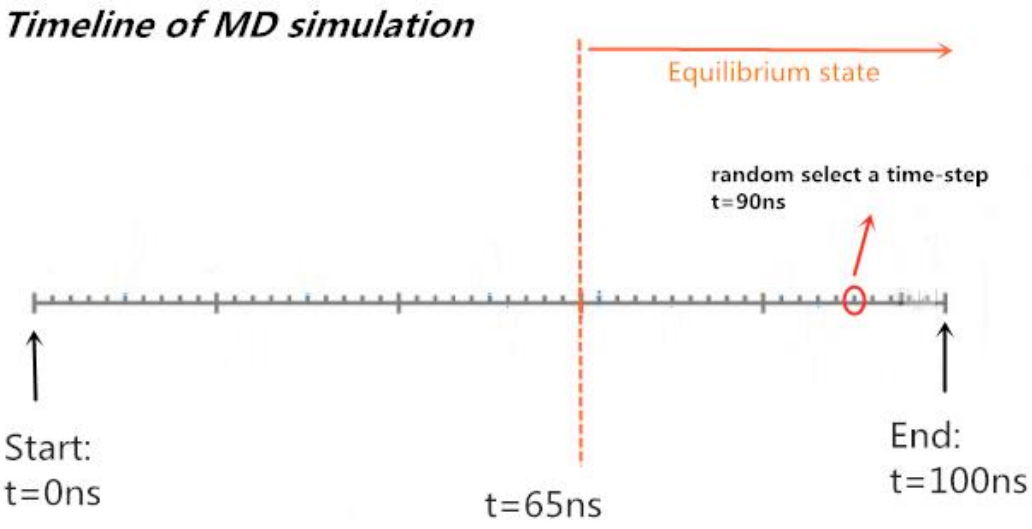

Figure 70: Simulation timeline of the case (4400 psi and 200 F); Equilibrium-state period is from 65 ns to 100 ns.

In detail, **Figure 70** shows the simulation timeline of the case under 4400 psi and 200 F and the equilibrium-state of the system is from 65 ns to 100 ns. The true partition coefficient of CO_2 should be an average value of all partition coefficient that calculated from 65 ns to 100 ns and it is not just one value calculated at a random timestep. (like the example K_{CO_2}= 1.34 which is calculated based on coordinate file at time = 90 ns).

There are two challenges in this idea. The first challenge is that there are a lot of timesteps in the period of equilibrium-state, so it is very time-consuming to find the K value of all timesteps one by one. The second challenge is the coordinate file of some timesteps can't give us a perfect geometric relationship like **Figure 68** and **Figure 69** shown. For example, as **Figure 71** shown:

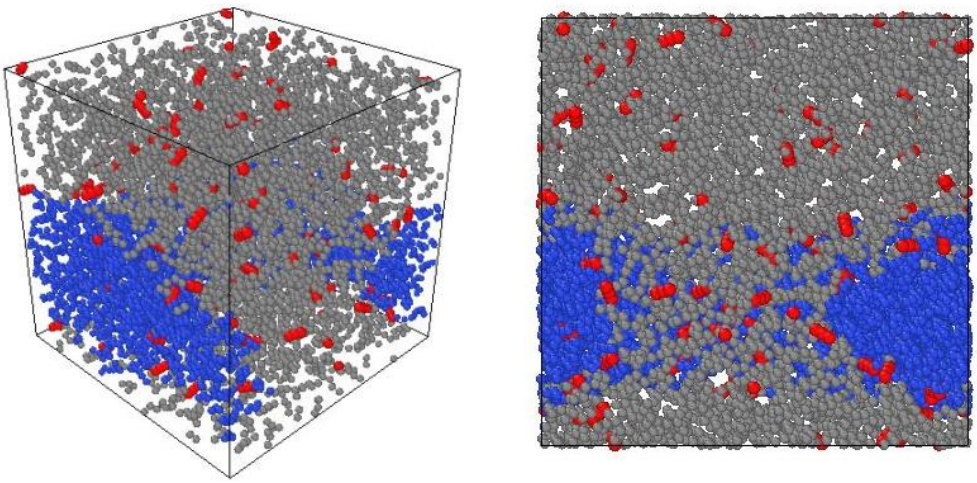

Figure 71: CO_2 molecules dissolved in the water phase and oil phase under 200 F and 2900 psi, at time = 78 ns (Equilibrium state).

At time = 78 ns, the water zone and oil zone formed such an irregular-shape structure which largely increased the difficulty on determining CO_2 number in each zone. I didn't find the solution for these two challenges in my thesis and this is why the method can only be a constructive idea or a suggestion.

Chapter 6: Conclusions and Recommendations

6.1 Conclusions

1. The new cylindrical SLD-PR model developed by Tolbert and Wu is successfully validated by molecular dynamics simulation. In this part, we first constructed a carbon nanotube with 10nm diameter to represent organic-nanopore in MD simulation. The behavior of pure-C1 fluid and C1/C4-mixture fluid in a 10nm diameter pore were studied through MD simulation and cylindrical SLD model. For all of the different-pressure cases, the results from cylindrical SLD model have a good match with MD simulation, which means the cylindrical SLD model is reliable and can be applied to other studies (for instance, OGIP estimation).
2. The adsorption behavior of the single-component system and multi-component system were studied via a combination of MD simulation and cylindrical SLD model. Under a specified condition (such as P/T, composition, pore width known), the adsorbed gas and free gas can be defined through their local density distribution profile. Furthermore, as pressure increase, the density of both adsorbed gas and free gas will increase, especially for adsorbed gas, which means more and more gas will be in the adsorption phase as pressure increase.
3. From MD simulation results, it is clear to see that the second adsorption layer present as pressure increase, and this is because molecular interaction will be stronger as pressure increase. From this point, it can be concluded that the

multiple adsorption layers exist in nanopores under high pressure, which is also another explanation for that the density of adsorbed gas will increase largely as pressure increase.

4. The behavior of competition-adsorption in the multi-component system was studied via MD simulation and cylindrical SLD model. The Composition-distribution graph from SLD model and Number-distribution graph from MD simulation show the same result which is the pore-wall has a stronger effect on heavier and more complex component because of its larger molecular polarizability.
5. After the cylindrical SLD model was validated by MD simulation, a new framework to estimate OGIP is developed through the combination of pore size distribution and verified SLD model, and a case study to test the new framework was successfully achieved.
6. The effect of pore size distribution on OGIP is consequential. The larger volume of adsorbed gas is stored in smaller nanopore because of stronger molecular interaction. Therefore, more and more relatively small nanopores in a shale gas formation can vastly increase its OGIP.
7. For a pure C1/C4 system, the location of the first peak (critical distance) in its radial distribution function (RDF) can't be a sufficient criterion to distinguish its phase state because the critical distance of its gas-state and liquid-state are almost same.

8. The critical distance of methane (or N-butane) is a natural property of itself and it is not affected by external factors such as temperature, pressure and so on.
9. In the water/oil/CO_2 system, as pressure increases, the self-diffusion coefficient of CO_2 decreases; on the opposite, the self-diffusion coefficient of CO_2 increases as temperature increases. Therefore, those tertiary recovery methods based on CO_2 substance (such as immiscible CO_2 flooding, in-situ CO_2 generation) are best applied in a high-pressure reservoir or low-temperature reservoir.

6.2 Future Recommendations

1. In chapter 3, an ideal and perfect cylindrical nanotube was constructed for studying the adsorption behavior of hydrocarbon fluid. In the future, the factors such as the roughness of pore surface, the wavelength of pore structure can be considered to make CNT more realistic.
2. On the basis of methods discussed in chapter 4, an acceptable tolerance or additional parameter is required for determining the phase-state of hydrocarbon fluid successfully by using MD simulation.
3. In the water/oil/CO_2 system, how to find an applicable and time-saving method for calculating true partition coefficient can be the future work. In addition, the MD simulation can also be tried to study the subjects such as reduction of oil viscosity, oil swelling through CO_2-related flooding process.

References

1. Aljamaan, Hamza. "Multi-Component Physical Sorption Investigation of Gas Shales at the Core Level." In *SPE Annual Technical Conference and Exhibition*, 24. Houston, Texas, USA: Society of Petroleum Engineers, 2015.

2. Aljamaan, Hamza. "Petrophysical Investigation on Gas Transport Properties of the Barnett." In *SPE Annual Technical Conference and Exhibition*, 15. New Orleans, Louisiana, USA: Society of Petroleum Engineers, 2013.

3. Ambrose, Raymond Joseph, Robert Chad Hartman, Mery Diaz Campos, I. Yucel Akkutlu, and Carl Sondergeld. "New Pore-Scale Considerations for Shale Gas in Place Calculations." In *SPE Unconventional Gas Conference*, 17. Pittsburgh, Pennsylvania, USA: Society of Petroleum Engineers, 2010.

4. B. Curtis, John. *Fractured Shale-Gas Systems*. Vol. 86,2002. doi:10.1306/61EEDDBE-173E-11D7-8645000102C1865D.

5. Basan, Paul B., Ben D. Lowden, Peter R. Whattler, and John J. Attard. "Pore-Size Data in Petrophysics: A Perspective on the Measurement of Pore Geometry." *Geological Society, London, Special Publications* 122, no. 1 (1997): 47.

6. Brunauer, Stephen, P. H. Emmett, and Edward Teller. "Adsorption of Gases in Multimolecular Layers." *Journal of the American Chemical Society* 60, no. 2 (1938/02/01 1938): 309-19.

7. Bullin, K. A., and Peter E. Krouskop. *Compositional Variety Complicates Processing Plans for Us Shale Gas*. Vol. 107,2009.

8. Chalmers, Gareth, R. Marc Bustin, and Ian Power. *Characterization of Gas Shale Pore Systems by Porosimetry, Pycnometry, Surface Area, and Field Emission Scanning Electron Microscopy/Transmission Electron Microscopy Image Analyses: Examples from the Barnett, Woodford, Haynesville, Marcellus, and Doig Units*. Vol. 96,2012. doi:10.1306/10171111052.

9. Charoensuppanimit, Pongtorn, Sayeed A. Mohammad, and Khaled A. M. Gasem. "Measurements and Modeling of Gas Adsorption on Shales." *Energy & Fuels* 30, no. 3 (2016/03/17 2016): 2309-19.

10. Clarkson, C. R., N. Solano, R. M. Bustin, A. M. M. Bustin, G. R. L. Chalmers, L. He, Y. B. Melnichenko, A. P. Radliński, and T. P. Blach. "Pore Structure Characterization of North American Shale Gas Reservoirs Using Usans/Sans, Gas Adsorption, and Mercury Intrusion." *Fuel* 103 (2013/01/01/ 2013): 606-16.

11. Collell, Julien, Guillaume Galliero, Romain Vermorel, Philippe Ungerer, Marianna Yiannourakou, François Montel, and Magali Pujol. "Transport of Multicomponent Hydrocarbon Mixtures in Shale Organic Matter by Molecular Simulations." *The Journal of Physical Chemistry C* 119, no. 39 (2015/10/01 2015): 22587-95.

12. Curtis, Mark Erman, Raymond Joseph Ambrose, and Carl H. Sondergeld. "Structural Characterization of Gas Shales on the Micro- and Nano-Scales." In *Canadian Unconventional Resources and International Petroleum Conference*, 15. Calgary, Alberta, Canada: Society of Petroleum Engineers, 2010.

13. Dhanapal, Kaverinathan, Deepak Devegowda, Yijia Zhang, Adriana C. Contreras-Nino, Faruk Civan, and Richard Sigal. "Phase Behavior and Storage in Organic Shale Nanopores: Modeling of Multicomponent Hydrocarbons in Connected Pore Systems and Implications for Fluids-in-Place Estimates in Shale Oil and Gas Reservoirs." In *SPE Unconventional Resources Conference*, 17. The Woodlands, Texas, USA: Society of Petroleum Engineers, 2014.

14. Frantz, Joseph H., Walter K. Sawyer, Ronald James MacDonald, Jeron Ray Williamson, David Johnston, and George Waters. "Evaluating Barnett Shale Production Performance-Using an Integrated Approach." In *SPE Annual Technical Conference and Exhibition*, 18. Dallas, Texas: Society of Petroleum Engineers, 2005.

15. Freeman, Craig, George J. Moridis, Gerard Eric Michael, and Thomas Alwin Blasingame. "Measurement, Modeling, and Diagnostics of Flowing Gas Composition Changes in Shale Gas Wells." In *SPE Latin America and Caribbean Petroleum Engineering Conference*, 25. Mexico City, Mexico: Society of Petroleum Engineers, 2012.

16. Ghanbarian, Behzad. "Estimating Gas Relative Permeability of Shales from Pore Size Distribution." In *SPE Annual Technical Conference and Exhibition*, 13. Dallas, Texas, USA: Society of Petroleum Engineers, 2018.

17. Hinai, Adnan Al, Reza Rezaee, Lionel Esteban, and Mehdi Labani. "Comparisons of Pore Size Distribution: A Case from the Western Australian

Gas Shale Formations." *Journal of Unconventional Oil and Gas Resources* 8 (2014/12/01/ 2014): 1-13.

18. Jenkins, Creties D., and Charles M. Boyer, II. "Coalbed- and Shale-Gas Reservoirs." *Journal of Petroleum Technology* 60, no. 02 (2008/2/1/ 2008): 92-99.

19. Jin, Bikai, and Hadi Nasrabadi. "Phase Behavior in Shale Organic/Inorganic Nanopores from Molecular Simulation." *SPE Reservoir Evaluation & Engineering* 21, no. 03 (2018/8/1/ 2018): 626-37.

20. Jin, Zhehui, and Abbas Firoozabadi. "Phase Behavior and Flow in Shale Nanopores from Molecular Simulations." In *SPE Annual Technical Conference and Exhibition*, 35. Houston, Texas, USA: Society of Petroleum Engineers, 2015.

21. Joshi, Ameet V. "Statistical Analysis of in-Line Inspection Performance with Gamma Distribution." In *CORROSION 2011*, 10. Houston, Texas: NACE International, 2011.

22. Kale, Sagar Vivek, Chandra Shekhar Rai, and Carl H. Sondergeld. "Petrophysical Characterization of Barnett Shale." In *SPE Unconventional Gas Conference*, 17. Pittsburgh, Pennsylvania, USA: Society of Petroleum Engineers, 2010.

23. Ko, Lucy T., Robert G. Loucks, Stephen C. Ruppel, Tongwei Zhang, and Sheng Peng. "Origin and Characterization of Eagle Ford Pore Networks in the South Texas Upper Cretaceous Shelf." *AAPG Bulletin* 101, no. 3 (2017): 387-418.

24. Labani, Mohammad Mahdi, Reza Rezaee, Ali Saeedi, and Adnan Al Hinai. "Evaluation of Pore Size Spectrum of Gas Shale Reservoirs Using Low Pressure Nitrogen Adsorption, Gas Expansion and Mercury Porosimetry: A Case Study from the Perth and Canning Basins, Western Australia." *Journal of Petroleum Science and Engineering* 112 (2013/12/01/ 2013): 7-16.

25. Langmuir, Irving. "The Adsorption of Gases on Plane Surfaces of Glass, Mica and Platinum." *Journal of the American Chemical Society* 40, no. 9 (1918/09/01 1918): 1361-403.

26. Li, Wenjie, Changcheng Wang, Zejin Shi, Yi Wei, Huailai Zhou, and Kun Deng. "The Description of Shale Reservoir Pore Structure Based on Method of Moments Estimation." *PLOS ONE* 11, no. 3 (2016): e0151631.

27. Li, Zhidong, Zhehui Jin, and Abbas Firoozabadi. "Phase Behavior and Adsorption of Pure Substances and Mixtures and Characterization in Nanopore Structures by Density Functional Theory." *SPE Journal* 19, no. 06 (2014/12/1/ 2014): 1096-109.

28. Liu, Yu, Yanming Zhu, Wu Li, Jianhua Xiang, Yang Wang, Jiahong Li, and Fangui Zeng. "Molecular Simulation of Methane Adsorption in Shale Based on Grand Canonical Monte Carlo Method and Pore Size Distribution." *Journal of Natural Gas Science and Engineering* 30 (2016/03/01/ 2016): 119-26.

29. Ma, Yixin, and Ahmad Jamili. "Using Simplified Local Density/ Peng-Robinson Equation of State to Study the Effects of Confinement in Shale Formations on Phase Behavior." In *SPE Unconventional Resources Conference*, 14. The Woodlands, Texas, USA: Society of Petroleum Engineers, 2014.

30. Ma, Yixin, Baoyan Li, Alberto Mezzatesta, and Ahmad Jamili. "Simplified Local Density Theory for Modeling Adsorbed Gas and Estimation of Gas-in-Place of Unconventional Gas Condensate Reservoirs." In *International Petroleum Technology Conference*, 23. Bangkok, Thailand: International Petroleum Technology Conference, 2016.

31. Martin, Marcus G., and J. Ilja Siepmann. "Novel Configurational-Bias Monte Carlo Method for Branched Molecules. Transferable Potentials for Phase Equilibria. 2. United-Atom Description of Branched Alkanes." *The Journal of Physical Chemistry B* 103, no. 21 (1999/05/01 1999): 4508-17.

32. Martin, Marcus, and Ilja J Siepmann. *Transferable Potentials for Phase Equilibria. 1. United-Atom Description of N-Alkanes*. Vol. 102,1998. doi:10.1021/jp972543+.

33. Mavor, Matt. "Barnett Shale Gas-in-Place Volume Including Sorbed and Free Gas Volume." (2003).

34. Nakagawa, Seiji, Timothy J. Kneafsey, Thomas M. Daley, Barry M. Freifeld, and Emily V. Rees. "Laboratory Seismic Monitoring of Supercritical Co2 Flooding in Sandstone Cores Using the Split Hopkinson Resonant Bar Technique with Concurrent X-Ray Computed Tomography Imaging." *Geophysical Prospecting* 61, no. 2 (2013/03/01 2013): 254-69.

35. Nelson, Philip H. "Pore-Throat Sizes in Sandstones, Tight Sandstones, and Shales." *American Association of Petroleum Geologists Bulletin* 93, no. 3 (2009): 329-40.

36. Oobatake, Motohisa, Soichi Hayashi, and Katsunosuke Machida. "Molecular Dynamics Simulation of Structure of Liquid Methane." (1990).

37. Pang, Yu, M. Y. Soliman, and Jie Sheng. "Investigation of Adsorption Effects on Nanopores in Shale Gas Reservoir by Simplified Local-Density Model." In *SPE/AAPG/SEG Unconventional Resources Technology Conference*, 20. San Antonio, Texas, USA: Unconventional Resources Technology Conference, 2016.

38. Pitakbunkate, Termpan, Perla B. Balbuena, George J. Moridis, and Thomas A. Blasingame. "Effect of Confinement on Pressure/Volume/Temperature Properties of Hydrocarbons in Shale Reservoirs." *SPE Journal* 21, no. 02 (2016/4/1/ 2016): 621-34.

39. Prammer, M. G. "Nmr Pore Size Distributions and Permeability at the Well Site." In *SPE Annual Technical Conference and Exhibition*, 10. New Orleans, Louisiana: Society of Petroleum Engineers, 1994.

40. Rangarajan, Bharath, Carl T. Lira, and Ramkumar Subramanian. "Simplified Local Density Model for Adsorption over Large Pressure Ranges." *AIChE Journal* 41, no. 4 (1995/04/01 1995): 838-45.

41. Ross, Daniel J. K., and R. Marc Bustin. "Shale Gas Potential of the Lower Jurassic Gordondale Member, Northeastern British Columbia, Canada." *Bulletin of Canadian Petroleum Geology* 55, no. 1 (2007): 51-75.

42. Sage, Bruce H., William N. Lacey, and Institute American Petroleum. *Thermodynamic Properties of the Lighter Paraffin Hydrocarbons and Nitrogen; Monograph on Api Research Project 37* [in English]. New York: Americna Petroleum Institute, 1950.

43. Saito, A., and H. C. Foley. "Curvature and Parametric Sensitivity in Models for Adsorption in Micropores." *AIChE Journal* 37, no. 3 (1991/03/01 1991): 429-36.

44. Schettler, P. D., Jr., and C. R. Parmely. "Gas Composition Shifts in Devonian Shales." *SPE Reservoir Engineering* 4, no. 03 (1989/8/1/ 1989): 283-87.

45. Shi, Ji-Quan, Ziqiu Xue, and Sevket Durucan. "Supercritical Co2 Core Flooding and Imbibition in Tako Sandstone—Influence of Sub-Core Scale Heterogeneity." *International Journal of Greenhouse Gas Control* 5, no. 1 (2011/01/01/ 2011): 75-87.

46. Shiau, Bo Jier Ben, Tzu-Ping Hsu, Bruce Lynn Roberts, and Jeffrey H. Harwell. "Improved Chemical Flood Efficiency by in Situ Co2 Generation." In *SPE Improved Oil Recovery Symposium*, 10. Tulsa, Oklahoma, USA: Society of Petroleum Engineers, 2010.

47. Sigal, Richard Frederick. "Pore-Size Distributions for Organic-Shale-Reservoir Rocks from Nuclear-Magnetic-Resonance Spectra Combined with Adsorption Measurements." *SPE Journal* 20, no. 04 (2015/8/1/ 2015): 824-30.

48. Sing, Kenneth SW. "Reporting Physisorption Data for Gas/Solid Systems with Special Reference to the Determination of Surface Area and Porosity (Recommendations 1984)." *Pure and applied chemistry* 57, no. 4 (1985): 603-19.

49. Stalkup, Fred I., L. Doherty Memorial Fund of Aime Henry, Aime, and Engineers Society of Petroleum. *Miscible Displacement* [in English]. New York: AIME, 1984.

50. Tolbert, Brandon T., and Xingru Wu. "Quantifying Pore Size Distribution Effect on Gas in Place and Recovery Using Sld-Pr Eos for Multiple-Components Shale Gas Reservoir." In *SPE Asia Pacific Unconventional Resources Conference and Exhibition*, 27. Brisbane, Australia: Society of Petroleum Engineers, 2015.

51. Tzimas, E, A Georgakaki, C Garcia Cortes, and SD Peteves. "Enhanced Oil Recovery Using Carbon Dioxide in the European Energy System." (2005).

52. Umeda, Kazuki, Rongjuan Li, Yunosuke Sawa, Hirotatsu Yamabe, Yunfeng Liang, Hiromi Honda, Sumihiko Murata, *et al.* "Multiscale Simulations of Fluid Flow in Nanopores for Shale Gas." In *International Petroleum Technology Conference*, 19. Kuala Lumpur, Malaysia: International Petroleum Technology Conference, 2014.

53. Verma, Mahendra K. "Fundamentals of Carbon Dioxide-Enhanced Oil Recovery (Co2-Eor): A Supporting Document of the Assessment Methodology for Hydrocarbon Recovery Using Co2-Eor Associated with Carbon Sequestration." In *Open-File Report*, 24. Reston, VA, 2015.

54. Wang, Shuoshi, Mohannad J. Kadhum, Changlong Chen, Benjamin Shiau, and Jeffrey H. Harwell. "Development of in Situ Co2 Generation Formulations for Enhanced Oil Recovery." *Energy & Fuels* 31, no. 12 (2017/12/21 2017): 13475-86.

55. Wang, Xiaoqi, Zengqiang Zhai, Xu Jin, Songtao Wu, Jianming Li, Liang Sun, and Xiaodan Liu. "Molecular Simulation of Co2/Ch4 Competitive Adsorption in Organic Matter Pores in Shale under Certain Geological Conditions." *Petroleum Exploration and Development* 43, no. 5 (2016/10/01/ 2016): 841-48.

56. Whitson, Curtis H, and Michael R Brulé. *Phase Behavior*. Henry L. Doherty Memorial Fund of AIME, Society of Petroleum Engineers …, 2000.

57. Wu, Tianhao, and Abbas Firoozabadi. "Methane Flow in Shale Nanopores with Kerogen Microstructure by Molecular Simulations." In *SPE Annual Technical Conference and Exhibition*, 13. Dallas, Texas, USA: Society of Petroleum Engineers, 2018.

58. Yang, Feng, Zhengfu Ning, Q. Wang, D. T. Kong, K. Peng, and L. F. Xiao. *Fractal Characteristics of Nanopore in Shales*. Vol. 25,2014. doi:10.11764/j.issn.1672-1926.2014.04.0618.

59. Yu, Wei, Kamy Sepehrnoori, and Tadeusz Wiktor Patzek. "Evaluation of Gas Adsorption in Marcellus Shale." In *SPE Annual Technical Conference and Exhibition*, 16. Amsterdam, The Netherlands: Society of Petroleum Engineers, 2014.

60. Zekri, Abdulrazag Yusef, Reyadh A. Almehaideb, and Shedid A. Shedid. "Displacement Efficiency of Supercritical Co2 Flooding in Tight Carbonate Rocks under Immiscible Conditions." In *SPE Europec/EAGE Annual Conference and Exhibition*, 13. Vienna, Austria: Society of Petroleum Engineers, 2006.

61. Zhang, Haibo, and Dapeng Cao. "Molecular Simulation of Displacement of Shale Gas by Carbon Dioxide at Different Geological Depths." *Chemical Engineering Science* 156 (2016/12/15/ 2016): 121-27.

62. Zhang, Tingshan, Yingjie He, Yang Yang, and Kunyu Wu. "Molecular Simulation of Shale Gas Adsorption in Organic-Matter Nanopore." *Journal of Natural Gas Geoscience* 2, no. 5 (2017/12/01/ 2017): 323-32.

63. Zhang, Yu, Deyong Shao, Jianping Yan, Xiangjuan Jia, Yanfang Li, Ping Yu, and Tongwei Zhang. "The Pore Size Distribution and Its Relationship with Shale Gas Capacity in Organic-Rich Mudstone of Wufeng-Longmaxi Formations, Sichuan Basin, China." *Journal of Natural Gas Geoscience* 1, no. 3 (2016/06/01/ 2016): 213-20.

64. Zhao, Tianyi, Xiangfang Li, Huawei Zhao, and Xiangji Dou. "Micro-Storage State and Adsorption Behavior of Shale Gas." In *SPE Nigeria Annual International Conference and Exhibition*, 9. Lagos, Nigeria: Society of Petroleum Engineers, 2015.

65. Zhou, Jian. *Gibbs Ensemble Monte Carlo Simulation of Adsorption Equilibrium of Methane*. Vol. 17,2001.

66. Zolfaghari, Ashkan, and Hassan Dehghanpour. "Pore Size Distribution from Water Adsorption Isotherm." In *SPE Annual Technical Conference and Exhibition*, 15. Houston, Texas, USA: Society of Petroleum Engineers, 2015.

Appendix A

Main methodology for cylindrical PR-SLD model from Tolbert and Wu

$$\mu(r) = \mu_{bulk} = \mu_{ff}(ri) + \mu_{fs}(ri)$$

$$\mu_{bulk} = \mu_0(T) + RTln(\frac{f_{bulk}}{f_0})$$

$$\mu_{ff}(r) = \mu_0(T) + RTln(\frac{f_{ff}(r)}{f_0})$$

$$\mu_{fs} = N_A\varphi(r,R)$$

$$\varphi(r,R) = \pi^2\rho_{atoms}\varepsilon_{fs}\sigma_{fs}^2[\frac{63}{62}\left[\frac{r}{\sigma_{fs}}\left(2-\frac{r}{R}\right)\right]^{-10} \times F\left(-\frac{9}{2},\frac{9}{2};1;\left(1-\frac{r}{R}\right)^2\right)$$

$$-3\left[\frac{r}{\sigma_{fs}}\left(2-\frac{r}{R}\right)\right]^{-4} \times F\left(-\frac{3}{2},\frac{3}{2};1;\left(1-\frac{r}{R}\right)^2\right)]$$

$$\sigma_{fs} = \frac{\sigma_{ff}+\sigma_{ss}}{2}$$

$$f_{ff}(r) = f_{bulk}\exp[-\frac{\varphi_{fs}(r)}{RT}]$$

PR-EoS applied in model:

$$\frac{P}{\rho RT} = \frac{1}{1-\rho b} - \frac{\alpha_T\rho}{RT\left[1+\left(1-\sqrt{2}\right)\rho b\right][1+\left(1+\sqrt{2}\right)\rho b]}$$

$$\mathrm{b} = \sum y_i b_i$$

$$a_T = \sum\sum y_i y_j (a_{Ti}a_{Tj})\text{^}0.5(1-\delta_{ij})$$

$$b_i = 0.07780\frac{RT_c}{P_c}$$

$$a_{Ti} = 0.45724a_j(\frac{R^2{T_c}^2}{P_c})$$

$${B_j}' = \frac{b_j}{b}$$

$${A_j}' = \frac{1}{a_T}[2{a_{Tj}}^{0.5}\sum_i y_i\,{a_{Tj}}^{0.5}(1-\delta_{ij})]$$

$$Z^3 - (1-B)Z^2 + (A - 2B - 3B^2)Z - (AB - B^2 - B^3) = 0$$

$$\mathrm{A} = \frac{a_T P}{R^2 T^2}$$

$$\mathrm{B} = \frac{bP}{RT}$$

$$\rho_{bulk} = \frac{P}{TRZ}$$

For single component system:

$$\ln\left(\frac{f_i^{Bulk}}{P}\right) = -\ln(Z-B) + (Z-1)B_j{}' - \frac{A}{2^{1.5}B}\left(A_j{}' - B_j{}'\right)\ln\left(\frac{Z + (2^{0.5}+1)B}{Z + (2^{0.5}-1)B}\right)$$

For multi-components system:

$\sum y_i$=1

$$\ln\left(\frac{f_i{}^{ff}}{y_i P}\right) = \frac{b_i}{b}\left(\frac{P}{RT\rho(r_i)} - 1\right) - \ln\left[\frac{P}{RT\rho(f_i)} - \frac{Pb}{RT}\right] + \frac{a_{ff}(z)}{2\sqrt{2}bRT}\left(\frac{b_i}{b}\right.$$

$$\left. - \frac{2\sum_j y_j a_{ij}{}^{ff}(z)}{a_{ff}(z)}\right)\ln\left(\frac{1 + \left(1+\sqrt{2}\right)\rho(r_i)b}{1 + \left(1-\sqrt{2}\right)\rho(r_i)b}\right)$$

Table: Physical Properties of Methane and Butane Molecule					
Component	Critical Pressure (Psia)	Critical Temperature (R)	Accentric Factor	Molecular Diameter (nm)	Energy coefficient ε/K_B
C1	669	343	0.011	0.376	149
C4	552	765	0.200	0.469	531

Appendix B

VLE-17:

$$K_i = \frac{P_{ci}}{p}\exp\{5.37(1+w_i)\left[1-\frac{T_{ci}}{T}\right]\}$$

VLE-9:

$$\sum_{i=1}^{n}(y_i - x_i) = \sum_{i=1}^{n}\frac{z_i(k_i-1)}{(k_i-1)\frac{V}{F}+1} = f\left(\frac{V}{F}\right) = 0$$

VLE-6:

$$x_i = \frac{z_i}{1+\frac{V}{F}(k_i-1)}$$

VLE-7:

$$y_i = x_i k_i = \frac{z_i k_i}{1+\frac{V}{F}(k_i-1)}$$

C-38:

$$A_L = C_a\frac{P}{T\text{^}2}[\sum_{i=1}^{n} x_i T_{ci}(\frac{a_i}{p_{ci}})^{0.5}]\text{^}2$$

C-39:

$$A_V = C_a\frac{P}{T\text{^}2}[\sum_{i=1}^{n} y_i T_{ci}(\frac{a_i}{p_{ci}})^{0.5}]\text{^}2$$

C-40:

$$B_L = C_b\frac{p}{T}\sum_{i=1}^{n} x_i T_{ci}/P_{ci}$$

C-41:

$$B_V = C_b \frac{p}{T} \sum_{i=1}^{n} y_i T_{ci}/P_{ci}$$

C-5:

$$Z_L^3 - Z_L^2 + Z_L(A_L - B_L - B_L^2) - A_L B_L = 0$$

C-6:

$$Z_V^3 - Z_V^2 + Z_V(A_V - B_V - B_V^2) - A_V B_V = 0$$

C-7:

$$\ln \varphi_i^L = \left(\frac{b_i}{b}\right)_L (Z_L - 1) - \ln(Z_L - B_L) - \frac{A_L}{B_L}\left[2\left(\frac{a_i}{a}\right)_L^{0.5} - \left(\frac{b_i}{b}\right)_L\right] \ln\left(1 + \frac{B_L}{Z_L}\right)$$

C-8:

$$\ln \varphi_i^V = \left(\frac{b_i}{b}\right)_V (Z_V - 1) - \ln(Z_V - B_V) - \frac{A_V}{B_V}\left[2\left(\frac{a_i}{a}\right)_V^{0.5} - \left(\frac{b_i}{b}\right)_V\right] \ln\left(1 + \frac{B_V}{Z_V}\right)$$

C-2:

$$K_i = \frac{y_i}{x_i} = \frac{\varphi_i^L}{\varphi_i^V}$$